Mechanical Properties of Superelastic and Shape-Memory NiTi and NiTi-TiC Composites Investigated by Neutron Diffraction

by

Rajan Vaidyanathan

B.S., Chemical Engineering
Lafayette College, May 1994

M.S., Materials Science and Engineering
Stanford University, June 1995

Submitted to the Department of Materials Science and Engineering in partial fulfillment of the requirements for the degree of

Doctor of Philosophy in Materials Engineering

at the
Massachusetts Institute of Technology
February 1999

Author.....
Department of Materials Science and Engineering
January 8, 1999

Certified by.....
David C. Dunand
AMAX Associate Professor of Materials Engineering
Thesis Supervisor

Certified by.....
Linn W. Hobbs
John F. Elliot Professor of Materials
Chairman, Departmental Committee on Graduate Students

Mechanical Properties of Superelastic and Shape-Memory NiTi and NiTi-TiC Composites Investigated by Neutron Diffraction

by

Rajan Vaidyanathan

Submitted to the Department of Materials Science and Engineering on January 8, 1999 in partial fulfillment of the requirements for the degree of Doctor of Philosophy in Materials Engineering

Abstract

The objective of this work was to study materials subjected to external loading where alternative deformation mechanisms are available to generate strains. In the case of shape-memory and superelastic NiTi, these mechanisms are twinning and stress-induced phase transformation, respectively. Superelastic NiTi (51.0 at.% Ni) reinforced with 0, 10 and 20 vol.% TiC particles was fabricated by Hot Isostatic Pressing (HIP), heat-treated and deformed under uniaxial compression while neutron diffraction spectra were collected. The experiments yielded in-situ measurements of the reversible austenite to martensite stress-induced transformation in NiTi. A methodology is established to ascertain the evolving discrete phase strains, austenite/martensite volume fractions and texture during stress-induced transformations using Rietveld refinement. Phase fractions and strains are discussed using Eshelby's theory in terms of load transfer in composites where the matrix undergoes a stress-induced phase transformation. Evolution of texture distributions in austenite and martensite are examined as a function of stress and strain by Rietveld refinements using a spherical harmonic texture formulation.

The following phenomenological changes are noted from in situ neutron diffraction measurements on superelastic NiTi subjected to stress-cycling : (i) the volume fraction of martensite formed remains almost unchanged (ii) the average phase strain in austenite remains mostly unchanged at intermediate loads but changes for unloaded austenite (iii) the texture in martensite and austenite under load changes significantly resulting in changes in macroscopic stress-strain behavior (iv) the isotropic and anisotropic components of the strain in austenite redistribute themselves. While the mechanical characteristics of stress-cycling have been previously studied, the relevance of this work stems from the fact that such fundamentally significant phenomenological changes are reported for the first time.

Mention is made of the work initiated to study the fatigue behavior of shape-memory NiTi and NiTi-TiC composites. The materials were fabricated using HIP and subsequently characterized. Fatigue crack growth experiments were carried out at room temperature and the results reported. A pre-cracked, compact test, shape-memory NiTi specimen was subjected to neutron diffraction measurements under various loaded and unloaded conditions. Suggestions for related future projects are made.

Thesis Supervisor: Prof. David C. Dunand
Title: AMAX Associate Professor of Materials Engineering

TABLE OF CONTENTS

LIST OF FIGURES

LIST OF TABLES

ACKNOWLEDGEMENTS

Ein einziger dankbarer Gedanke gen Himmel ist das vollkommenste Gebet
"One single grateful thought raised to heaven is the most perfect prayer"
Minna von Barnhelm

I would like to express my sincere gratitude to:
Prof. David C. Dunand: I shall remain indebted to David for being my thesis advisor, having confidence in me and giving me an opportunity to study at MIT. I was very fortunate to work on this interesting project. His untiring enthusiasm and dedication has been a constant source of motivation.

Prof. Subra Suresh: for serving on my thesis committee and advising on the fatigue portion of this work. His friendly advice, kindness, wisdom and interest in my welfare will always be remembered. During the last six months, allowing me to be a part of the Laboratory for Experimental and Computational Micromechanics (LEXCOM) was a particularly enriching experience and is very much appreciated.

Prof. August Witt: for serving on my thesis committee and making useful suggestions to this thesis.

Dr. Mark Bourke, Dr. Mark Daymond, Dr. K. Bennett and Dr. B.Von Dreele at Los Alamos National Laboratory: for helping with the neutron diffraction measurements and analysis.

Dr. H. Voggenreiter, Dr. K. Johansen and Dipl-Ing J. Vlcek at Daimler Benz, AG Germany: for all their help and hospitality during my stay at Daimler-Benz.

Daimler-Benz AG, Germany: for funding this research project and my stay in Germany.

Dr. Sigrid Berka and the MIT-Germany program: for making it possible for me to spend six-months in Germany and coordinating my efforts to obtain funding.

My wonderful office-mates Hermann Holzer, Ann Jansen, Kai Johansen, Angeliki Lakkis, Jean-Marc Lefeuvre, Jacques Teisen, T.A. Venkatesh, Christian Verdon, Mike Whitney and Peter Zwigl: for their camaraderie and friendship. My stay at MIT has indeed been memorable thanks largely to them. I am sure that the friendships that started off in 8-328 will continue for a lifetime. More recently, my stay in the LEXCOM group has also been a lot of fun.

Gloria Landahl and Jamie Sieger: for always helping me find my way through the paperwork at MIT

and finally on the path to this PhD,

I find myself having been most influenced by my teachers.... more significantly by my late grandfather C.C. Hall, Prof. J.R. Martin, Prof. J.P. Schaffer , Mr. D. Chatterjee , Prof. W.D. Nix and Prof. A.D. Novaco ; and

the three people who undoubtedly are most responsible for it all, to whom I humbly dedicate this work, my parents: *Amma* for her boundless love, care and dedication to the family, *Appa* for always teaching me what hard-work and duty was all about and to "my guide, philosopher and friend"[1] Prof. James P. Schaffer for introducing me to research and giving me an opportunity.

"Beggar that I am, I am poor even in thanks"
William Shakespeare, Hamlet

---

[1] Alexander Pope, An Essay on Man

Chapter 1

Introduction

1.1 Motivation

This work was initiated with the primary purpose of studying materials subjected to external loading where alternative deformation mechanisms are available to generate strains. In the case of shape-memory and superelastic NiTi, these mechanisms are twinning and stress-induced phase transformation, respectively. Composites with matrices that deform plastically on loading (e.g., Al-SiC) have been extensively studied. The aim here was to fabricate and study composites with matrices that deform by undergoing stress-induced transformations in the presence of stiff elastic reinforcements. TiC particles were chosen as the reinforcement for reasons of non-reactivity with the matrix during processing, high modulus and low cost. The addition of TiC particles to superelastic NiTi could provide an effective means of changing its macroscopic stress-strain response.

Neutron diffraction is advantageous as it can be used to obtain individual phase information that is representative of bulk specimens during deformation. This is possible if neutron diffraction spectra can be obtained during applied external loading. However in order to obtain such phase specific information, a refinement methodology needed to be developed to analyze neutron spectra on account of the changing texture, volume fraction and low symmetry of the transforming monoclinic martensite phase during stress-induced phase transformations.

Having developed the means to obtain and analyze neutron spectra during reversible stress-induced austenite to martensite transformations two additional sets of experiments, keeping in mind the broad objective of this work, were performed. The first was to use neutron diffraction to study changes in reversible stress-induced austenite to martensite transformations arising from repeated stress-cycling. As described in Chapter 6, macroscopic observations have been made during such cycling experiments. However, the idea was to better understand the mechanisms that account for these observed changes. Such stress-cycling experiments may help modify the current industry practice of training (cycling to stabilize) superelastic materials. The second was to perform spatially resolved neutron diffraction measurements on a pre-cracked Compact Test

(CT) specimen in the loaded and unloaded state. The motivation was to observe and report a twinned zone ahead of a loaded crack in addition to plastic deformation ahead of the crack-tip.

As described in Chapter 4, previous work has characterized the uniaxial response of composites where the matrix deforms by twinning. This work has carefully characterized the uniaxial compressive response of composites where the matrix deforms by stress-induced transformation. The fatigue-fracture behavior of either of these composites systems has not been studied. This work initiates such an investigation by obtaining crack-growth data in shape-memory NiTi and NiTi composites.

Since the goals outlined in this work have not been undertaken before, for convenient reasons associated with the stress-rig in the neutron beam at Los Alamos National Laboratory compression samples were use. A more general understanding and discussion of phenomenological behavior was the objective. As will be discussed in detail in Chapter 5, differences in tension and compression can be expected. This difference is limited to magnitudes of the observed behavior (e.g., maximum recoverable strain) rather than significant differences in mechanisms. With the preceding motivation, the following objectives were established:

(1) Fabrication of NiTi composites: To fabricate and characterize NiTi (both austenitic and martensitic at room temperature) and such NiTi reinforced with TiC particles

(2) Uniaxial compression with simultaneous neutron spectra acquisition: To use neutron diffraction for monitoring the evolving discrete phase strains, texture and phase fractions while NiTi and NiTi reinforced with TiC (austenitic NiTi capable of reversibly forming martensite under stress) are uniaxially compressed

(3) Stress-cycling with simultaneous neutron spectra acquisition: To investigate the effect of stress-cycling on superelastic NiTi and to use neutron diffraction to monitor the phases as the transformation stabilizes

(4) Fatigue and fracture studies: To investigate the fatigue crack-growth behavior of martensitic NiTi with and without TiC reinforcements

(5) Loading of compact test specimen with simultaneous neutron spectra acquisition: To investigate deformation mechanisms ahead of the crack tip in martensitic NiTi

(6) Modeling: To establish a methodology to analyze neutron diffraction spectra obtained in the above cases and to apply Eshelby's theory to investigate load transfer and load partitioning

1.2 Organization

The following chapters are structured as expanded, stand-alone refereed journal articles or refereed conference proceedings (in various stages at the time of writing this thesis). The table below summarizes the content and outcome of each of the following chapters.

The first seven chapters of this thesis outline the work that was carried out at the Massachusetts Institute of Technology, Cambridge, MA and Los Alamos National Laboratory, Los Alamos, NM from July 1995 to August 1998. Prof. David C. Dunand, AMAX Associate Professor of Materials Engineering and thesis advisor, Prof. Subra Suresh, Richard P. Simmons Professor of Materials Science and Engineering and Professor of Mechanical Engineering and Prof. August F. Witt, Ford Professor of Engineering and Margaret MacVicar Faculty Fellow (all at MIT) constituted the author's thesis committee. Chapter 8 is an outcome of the author's experience from August 1997 to February 1998 in the research group of Dr. H. Voggenreiter in Daimler-Benz AG, Germany as part of the MIT-Germany program. It also included extensive interaction with personnel from Ruhr Universität Bochum and Technische Universität München in Germany in the area of shape-memory and superelastic alloys. The final public defense of the thesis was held on September 15, 1998.

Chapter	Subject	Publication
2	Introduction to neutron diffraction in superelastic NiTi	[1, 2]
3	Method of analysis of neutron diffraction spectra in stress-induced transformations in NiTi	[3]
4	Study of superelastic NiTi-0TiC and NiTi-10TiC, NiTi-20TiC composites	[4, 5]
5	Crystallographic features of stress-induced martensitic transformations	[6, 7]
6	Stress-cycling in superelastic NiTi investigated using neutron diffraction	[7]
7	Fatigue behavior of shape-memory NiTi-0TiC and NiTi-10TiC	[8]
8	Use of shape-memory and superelastic alloys	

Chapter 2

Observations of Stress-Induced Transformations in Superelastic NiTi by Neutron Diffraction

The formation of stress-induced martensite in superelastic NiTi was studied by neutron diffraction during uniaxial compressive loading and unloading. The respective phase fractions were determined as a function of the applied stresses using a Rietveld refinement with a March-Dollase texture formulation. Before loading, the specimen was fully austenitic. At the highest applied compressive stress of 625 MPa, about 90% of the austenitic phase had transformed to martensite, with a concomitant macroscopic strain of -2.9%. Upon unloading, all of the stress-induced martensite reverted to austenite and the totality of the macroscopic strain was recovered. The propensity for the various austenitic crystallographic orientations to transform at different stresses was determined and qualitative observation of this incipient texture in the austenite and of the inherent texture in the nascent martensite are reported.

2.1 Introduction

Depending on stoichiometry, applied stress and temperature, the intermetallic NiTi can exist as a cubic (B2) austenitic phase or as a monoclinic (B19') martensitic phase. The austenitic phase is usually associated with high-temperatures and the martensitic phase with low-temperatures. The transformation between these two phases is first-order, displacive, athermal and thermoelastic and can be induced by temperature and/or stress. At room temperature, the stress-induced transformation of nickel-rich NiTi from austenite to martensite can result in tensile strains as high as 8%. On unloading, the martensite becomes unstable and transforms back to austenite, leading to a concomitant macroscopic strain recovery. This so-called superelastic or pseudoelastic effect is related to the shape-memory effect where transformation is thermally induced in a twinned martensitic structure [9-11]. The transformation has a large shear component but only a small negative dilatant component (-0.54%) associated with it [12]. A typical idealized stress-strain curve for an austenitic material that displays such superelastic behavior by stress-induced transformation is shown in Fig. 2.1.

Electrical resistance measurements and Differential Scanning Calorimetry (DSC) have been widely used to track the transformation. In addition, changes in magnetic properties [13-15], electromotive force [16, 17], internal friction [18], damping [19], thermal conductivity [20,

21], Hall Coefficient [13, 15, 22, 23], hardness [24] and thermoelectric power [13] [14] are some of the properties that have been used to study the transformation [10]. None of these techniques or measurements can easily monitor martensite and austenite phases individually for texture, phase strain and phase volume fraction information during the transformation, especially when it is to be induced under an applied external stress.

A simple method to study such stress-induced transformations in superelastic NiTi single crystals is with optical surface observations which can track the formation of stress-induced martensite during loading and its back transformation to austenite during unloading [25-27]. However, this technique is not applicable in most polycrystalline specimens because of the small size scale of the transformed martensite features and diffraction techniques are therefore the preferred approach for polycrystals. X-ray diffraction on polycrystalline NiTi wires has identified stress-induced changes in crystal structure [28]. Whereas both x-ray and neutron diffraction can monitor such phase transformations, a major difference between the two techniques is the sampled volume of material[2]. The 50% transmission thickness for Cu K_α x-rays in NiTi is approximately 9 μm, compared to about 3 cm for thermal neutrons [29]. Hence, in a diffraction experiment, conventionally-produced x-rays only sample a shallow depth which is not necessarily representative of the bulk because of the proximity to the free surface (the same problem arises in electron microscopy). By contrast, neutron diffraction is ideally suited for the study of stress-induced transformations, because the average behavior of bulk polycrystals can be measured with sampling volumes of up to 1 cm^3. Although the irradiated volume is large compared to a typical polycrystalline microstructure, each diffraction peak is an average over many grains which have an orientation defined by scattering geometry. Thus while the transformation of an individual grain cannot be measured, the average behavior of many grains can be. At a pulsed neutron source operated in time of flight mode, collection of an entire diffraction pattern occurs for each measurement, and, for a given detector, the scattering vectors of all reflections lie in the same direction. Thus, in a single measurement, the behavior of all crystallographic planes can be explored by aligning the load axis relative to the scattering vector.

---

[2] X-rays from third-generation synchrotrons may be able to provide comparable penetration (Science, Vol. 277, pp. 1214, 29 August 1997). However, currently no setup exists to obtain *in situ* measurements under stress.

While neutron diffraction studies of twinning have been reported for martensitic shape-memory NiTi [30-32], to the best of our knowledge there has been only one other investigation of superelasticity [33]. In that case the structure of a Cu-Al-Ni single crystal was determined as a function of stress. However, results from single crystals are difficult to extend to polycrystals because of the differences in constraints and self-accommodation.

This chapter introduces neutron diffraction results on polycrystalline superelastic NiTi subjected to a series of stress levels. Quantitative measurements of the phase fractions and qualitative discussions of the texture are reported and discussed.

2.2 Experimental Procedures

In order to obtain austenitic nickel rich NiTi from available prealloyed, martensitic titanium-rich NiTi powders, two different nominal compositions (51.0 at.% Ni-NiTi and 50.6 at.% Ni-NiTi) were fabricated using Hot Isostatic Pressing (HIP) (1065 °C, 100 MPa, 3 h). The goal was to select a composition that demonstrated favorable (i.e. large recoverable strains) superelastic behavior. Samples with both these compositions were solutionized at 1000 °C for one hour and oil quenched to room temperature, both under titanium gettered flowing argon and subsequently annealed at 400 °C for 1 h in air and ice-water quenched. Samples were then subjected to Differential Scanning Calorimetry (DSC) and preliminary compressive uniaxial testing. The results identified NiTi with 51.0 at.% Ni as showing favorable superelastic behavior. Details of the DSC measurements are discussed in Chapter 4.

Identification of the optimum composition was followed by additional fabrication. Prealloyed NiTi powders (99.9 % pure, 49.4 at.% Ni, size between 44 μm and 177 μm, from Specialty Metals Corp., NY) were blended with Ni powders (99.9 % pure, size between 44 μm and 177 μm, from Specialty Metals Corp., NY) and TiC powders (99.9 % pure, 44 μm average size, from Atlantic Equipment Engineers, NJ) so that the overall nominal nickel composition was 51.0 at.%. The powder, packed in a low carbon steel container (0.318 cm thick, 1.9 cm in diameter and 12.7 cm in height and lined with a boron nitride coated nickel foil to prevent carbon contamination) was subjected to HIP at 1065 °C and 100 MPa for 3 h. One cylindrical compression specimen (10 mm in diameter and 24 mm in length) was fabricated by electrode-discharge machining and heat-treated as described above. Prior to the diffraction analysis the specimen, outfitted with an extensometer (gauge length 12.5 mm), was subjected to two training

(loading-unloading) cycles with peak compressive stresses of 563 MPa and 550 MPa at 3 mm/min ramp speed (unless otherwise stated all stresses and strains are compressive and only their magnitude is reported in this document). A non-recoverable compressive plastic strain of 0.1 % was recorded after the first training mechanical cycle but none was noted during the second or during the diffraction mechanical cycle, despite an increase in the maximum stress to 625 MPa. The training cycles served to stabilize and homogenize the transformation. The effect of stress-cycling on the transformation is addressed in detail in Chapter 6.

Diffraction measurements were performed using the Neutron Powder Diffractometer at the Los Alamos Neutron Science Center (LANSCE) at Los Alamos National Laboratory (LANL). In a polycrystalline material, individual reflections result from grains whose (hkl) orientation, specified in the crystallographic coordinate system, is parallel to the diffraction vector specified in the measurement coordinate system. The load axis was placed in a horizontal plane at 45° to the incident neutron beam, and two detectors recorded diffraction patterns with scattering vectors parallel and perpendicular to the load axis [31, 34-36]. This is schematically shown in Fig. 2.2. Thus diffraction information can be separately obtained from lattice planes perpendicular and parallel to the loading axis. The modified stress rig is shown in Fig. 2.3. The load was ramped in stroke control and kept constant during hold periods where diffraction spectra were collected. The ramp and hold periods were respectively, about 1 min and 2-4 h, depending on beam intensity. Diffraction spectra were recorded at 14 compressive stress levels, as depicted in Fig. 2.4.

2.3 Results and Discussion

Fig. 2.4 shows the stress-strain curve for all three cycles. The stresses at which the diffraction measurements were made are apparent from the steps in Fig. 2.4, associated with small time-dependent strains. These steps probably resulted from the sample temperature (increased or decreased by the transformation enthalpy according to loading or unloading) returning to ambient temperature during the hold period. This effect is discussed in more detail in Chapter 3.

The austenite is first elastically loaded, followed by strains associated with a transformation to stressed martensite. On unloading, the martensite transforms back to austenite followed by elastic unloading of the austenite. The difference in structure between the

unstressed and stressed states is shown in Fig. 2.5 in which the broad martensitic peaks are clearly discernible from the sharp austenitic peaks. The broad martensitic peaks arise due to the low symmetry of its monoclinic structure. The progression and reversibility of the stress-induced transformation are illustrated in Fig. 2.6 which shows a short section of the spectra for each stress level. Upon loading, the shift to shorter lattice spacings result from increasing elastic compressive strains, while the decrease in intensity of the austenite peak and concomitant increase in the martensitic peak are due to transformation. As illustrated in Fig. 2.7, where the intensity of the austenitic (100) and (111) peaks are plotted as a function of stress through the loading cycle, not all the austenitic reflections diminish at the same rate. At the maximum stress, the (100) intensity is close to zero whereas the (111) intensity is approximately half of the unloaded value. The propensity for transformation is thus related to the crystallographic orientation of the austenite. One unusual observation was that the integrated intensity of the austenitic reflections in the unstressed state showed a small increase after the loading cycle. This may be attributed to the evolving texture and is discussed in more detail in Chapter 6.

The incipient texture in the austenite described above, resulting from the transformation of austenite grains in preferred orientations with respect to the applied stress prior to those in less favorable orientations, is matched by the strong orientation in the nascent stress-induced martensite. For instance, the martensitic (010) peak was absent in spectra for which the scattering vector was parallel to the load, whereas the martensitic (100) peak was absent in spectra for which the scattering vector was perpendicular to the load. Rietveld refinements of the spectra (scattering vector parallel to load) were performed with a March-Dollase description of the texture [37, 38] using the Los Alamos Generalized Structure Analysis System GSAS program [39]. This method of analysis is described in the next chapter. The stress-dependence of the phase volume fractions determined by these refinements are shown in Fig. 2.8. An interesting result is that about 90% of the austenite is transformed to martensite at a compressive macroscopic strain of only 2.9%. Since the maximum recoverable strain in tension is 8% [40-42], this observation raises the question of whether, at strains above 2.9%, further recoverable strain can be produced by twinning of the stress-induced martensite. An alternate explanation is that in polycrystalline superelastic NiTi the strain is lower in compression than in tension. This issue is further addressed in detail in Chapter 5 of this thesis.

2.4 Conclusions

The significance of this work lies in the potential to quantify in polycrystals the proclivity for transformation of specific grain orientations at different stresses and at different angles to the loading direction. The results offer the potential to validate polycrystalline models and a mechanism to examine whether and how elastic anisotropy biases the transformation. In the following chapters these issues are addressed in more detail and further light is shed on the reversible stress-induced austenite to martensite transformation in both bulk NiTi and particulate-reinforced NiTi.

2.5 Figures

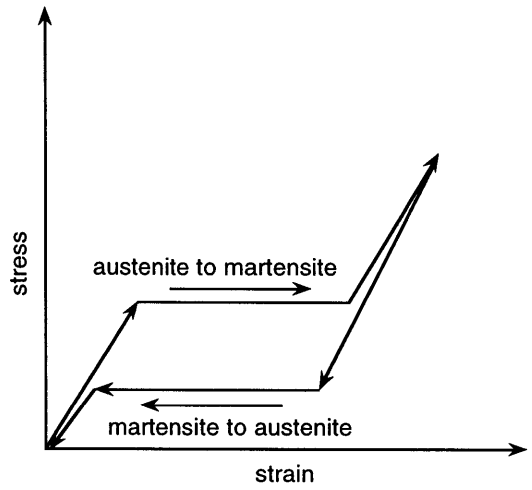

Fig. 2.1 Schematic stress-strain curve of an austenitic superelastic material undergoing a reversible stress-induced phase transformation.

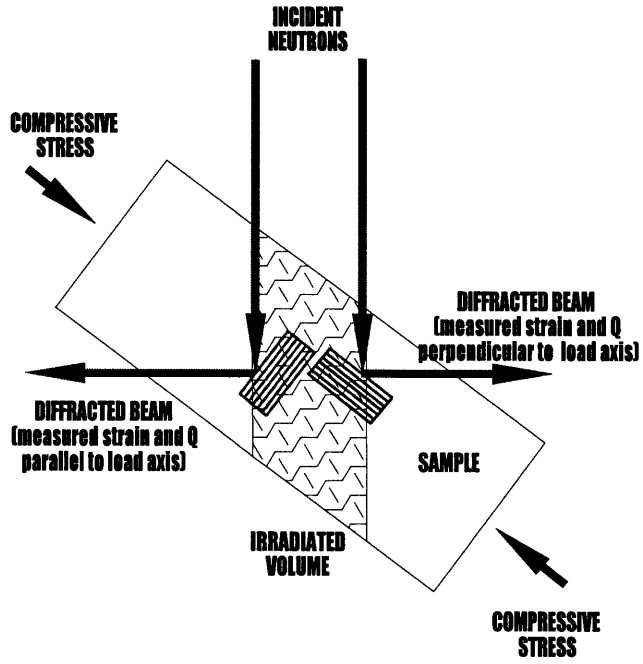

Fig. 2.2 Schematic of experimental setup at Los Alamos National Laboratory. The irradiated volume is about 1 cm^3 and the cylindrical sample is 10 mm in diameter and 24 mm in height. Q is the scattering vector.

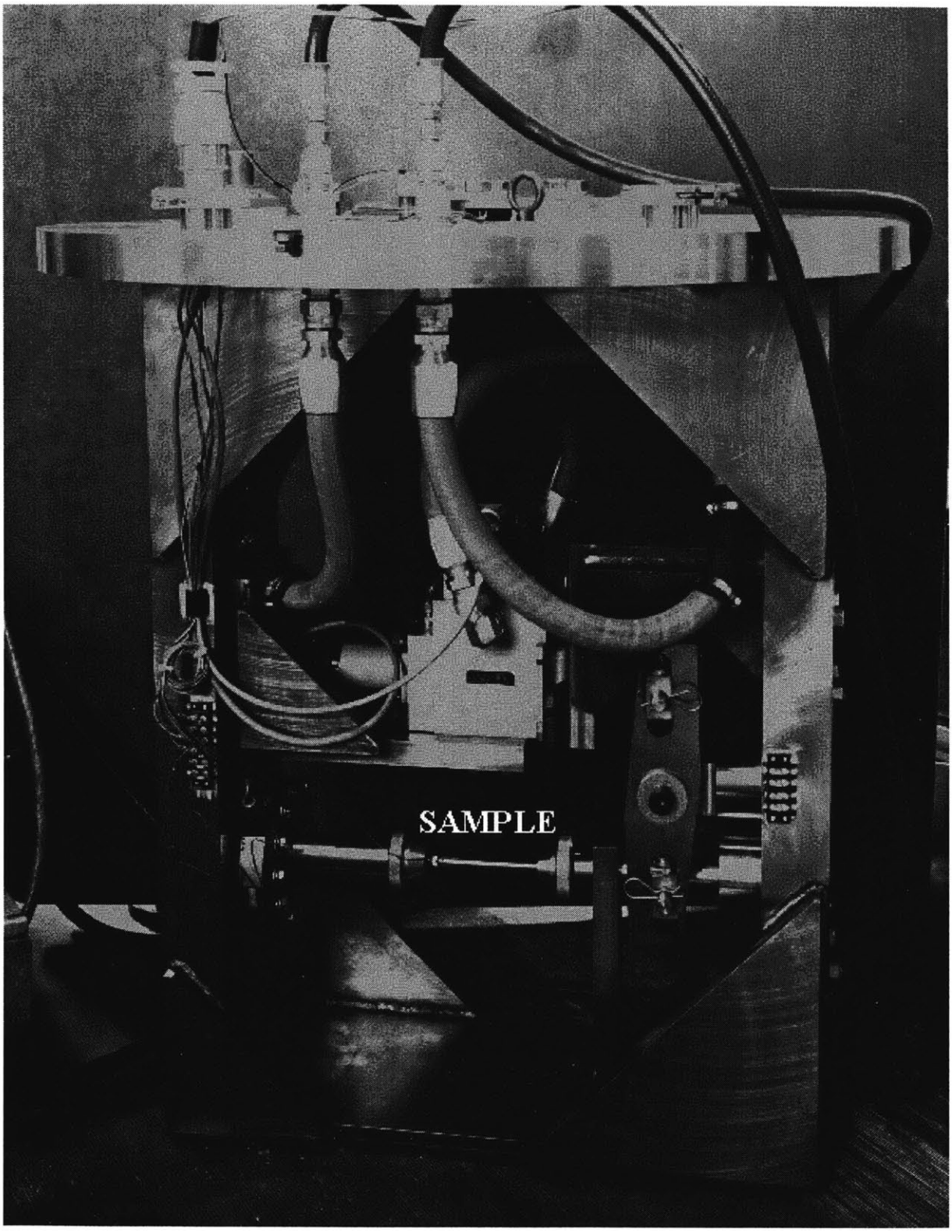

Fig. 2.3 Modified stress rig to apply stress as neutron diffraction spectra are obtained. The rig is precisely aligned and lowered into the path of the incident neutrons.

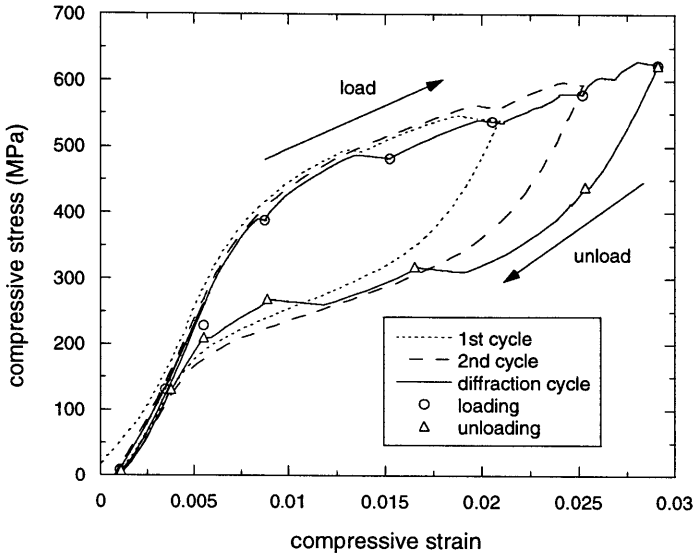

Fig. 2.4 Macroscopic compressive stress-strain curve of superelastic NiTi for the first (training), second (training) and third (diffraction) mechanical cycles. Stress levels at which diffraction spectra were recorded are marked with symbols.

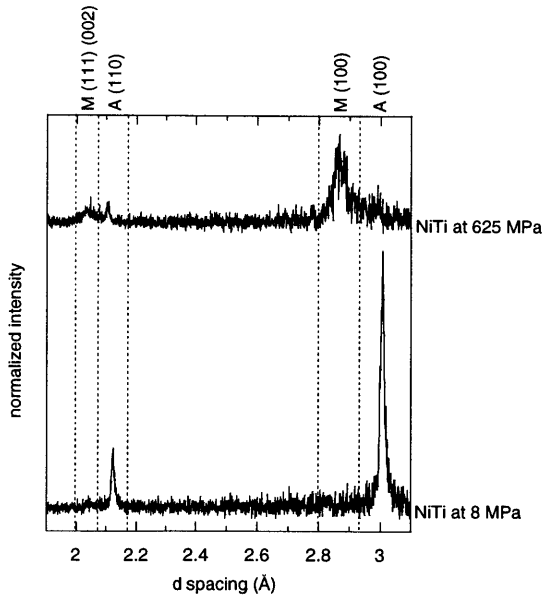

Fig. 2.5 Diffraction spectra for 100% austenitic and 90% martensitic compositions (8 MPa and 625 MPa, respectively) with main peaks labeled. The scattering vector is parallel to the loading direction. A small stress of 8 MPa was used to hold the NiTi specimen horizontally in the rig during "no load" measurements.

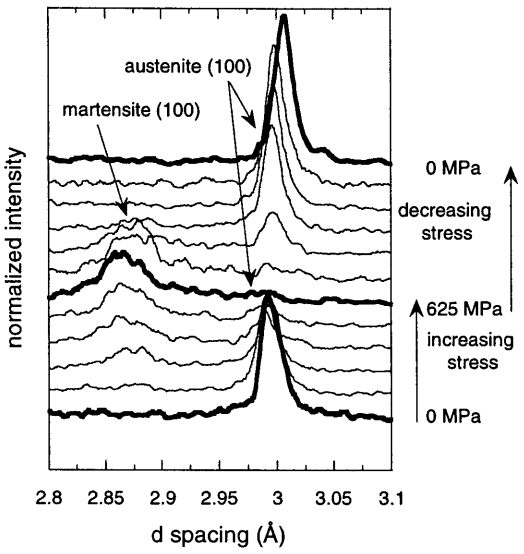

Fig. 2.6 Section of diffraction spectra for all applied stresses. The spectra are smoothed, normalized, and displaced along the Y axis for clarity. The scattering vector is parallel to the loading direction.

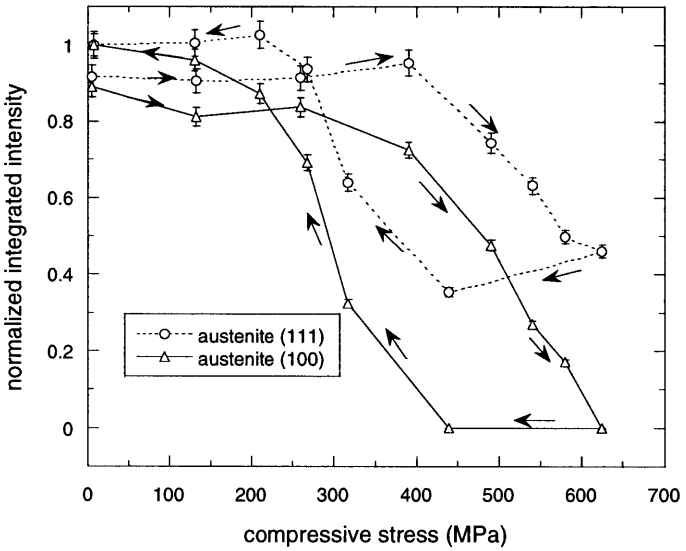

Fig. 2.7 Stress dependence of the intensity of (100) and (111) austenitic peaks normalized to their value after unloading. The scattering vector is parallel to the loading direction.

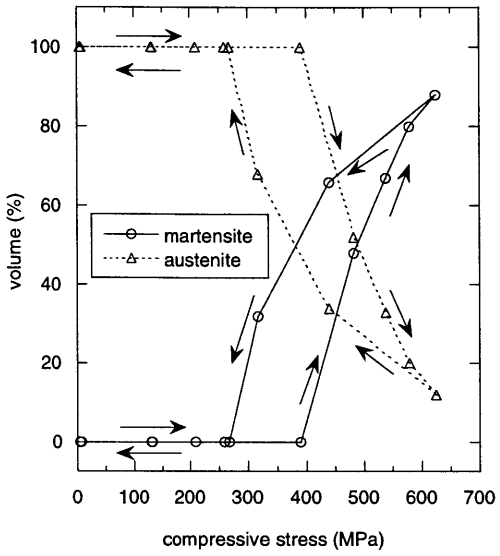

Fig. 2.8 Stress dependence of the volume (%) of martensite and austenite phases through the load cycle.

Chapter 3

Analysis of Neutron Diffraction Spectra from Stress-Induced Transformations in NiTi

In the previous chapter, the use of neutron diffraction to observe a stress-induced transformation in NiTi was described. Here a detailed analysis is made of neutron diffraction spectra obtained during such transformations. The analysis is carried out using individual lattice reflections as well as a Rietveld refinement that simultaneously uses lattice reflections in the entire spectra. The strain is described in terms of an isotropic component and an anisotropic component, which may be associated with anisotropy introduced by the transformation. To accurately quantify the evolving phase fractions, two approaches are used to formulate the evolving texture i.e. due to March-Dollase and a generalized spherical harmonics approach. Comparisons between a Rietveld refinement and single-peak analysis and the two texture formulations are made. A methodology is established to ascertain the discrete phase strains, phase volume fractions and texture during stress-induced transformations, to be used in the following chapters that investigate load transfer and stress cycling in superelastic NiTi and NiTi-TiC composites.

3.1 Introduction

For diffraction spectra obtained from specimens under mechanical load, shifts in positions of individual lattice plane reflections can be used to obtain elastic strains [43]. Anisotropy arising from crystal geometry (i.e., elastic) or strain redistribution among individual grains (i.e., plastic or transformation) may lead to significantly different responses between lattice planes, limiting the inferences that can be drawn from the analysis of individual peaks. One solution to this problem is to use a Rietveld refinement [44] which simultaneously considers reflections from many lattice planes and can describe the average polycrystalline deformation. By using the Rietveld technique, input from many lattice reflections that contribute to the overall deformation can be incorporated. Furthermore, the Rietveld refinement can also account for changes in intensity due to changes in phase volume fractions in multiphase materials and to preferred orientation or texture. Two such formulations of the texture are presented here, namely a model due to March and Dollase [37, 38] and a generalized spherical-harmonics texture formulation [45].

In the earlier chapter the utility of neutron diffraction measurements to observe stress-induced transformations in superelastic NiTi was demonstrated. The present chapter builds on this study while seeking to:

(a) describe texture evolution in stress-induced transformations from austenite to martensite in NiTi;

(b) highlight the differences between a March-Dollase texture formulation and a generalized spherical-harmonics texture formulation of both austenite and martensite phases;

(b) compare the strain responses of individual lattice planes in the austenite, especially as it transforms to martensite;

(c) use an anisotropy factor within the Rietveld discrete phase strain description of the austenite which tracks changes in the anisotropic component of the strain;

(d) compare measured strains and inferred phase fractions from individual lattice reflections and Rietveld refinements of neutron data from austenitic NiTi to aid practitioners at a steady state source where it may not be convenient to acquire data over a wide range of angles;

(e) establish a methodology to ascertain the discrete phase strains, phase volume fractions and texture during stress-induced transformations to be used in the following chapters that investigate load transfer and stress-cycling in superelastic NiTi and NiTi-TiC composites.

3.2 Experimental Procedures

3.2.1 Sample fabrication

The sample that was tested in Chapter 2 (designated hereafter as Sample 1) was further reduced by electrode-discharge machining to yield a cylindrical sample 8 mm in diameter and 20 mm in length (designated hereafter as Sample 2). Sample 2 was subjected to the same heat-treatment as outlined in §2.2 and then tested as described below. Both Samples 1 and 2 had an average grain size of 20 μm (polishing details are described in §7.2.2) and displayed a homogeneous composition from microprobe analysis.

3.2.2 Neutron diffraction and mechanical testing

The experimental setup is also described in §2.2. A third detector, in back-scattering geometry provided a measurement at an angle of 32° with the incident beam. An extensometer attached to the samples recorded macroscopic strain during the experiments. Sample 1 was tested

to a maximum stress of 625 MPa under uniaxial compression (stroke control at 3 mm/min) while Sample 2, because of its reduced cross-section, could be tested up to 975 MPa (stroke control at 0.1 mm/min). Diffraction data for Sample 1 were the same as that obtained in the previous chapter.

Fig. 3.2 shows the stress and strain levels at which neutron spectra were obtained with both samples in the neutron beam. These cycles were obtained after training the sample twice with a load-unload cycle up to 625 MPa at a stroke speed of 3 mm/min. The differences in the shape of the curves of the two samples are discussed in more detail in a later section. Due to limitations in data acquisition time (approx. 6 to 8 hours per stress level), the stress levels for Sample 2 were chosen to supplement data already obtained from Sample 1.

3.2.3 Transformation temperatures

Differential scanning calorimetry using a Perkin Elmer DSC-7 Calorimeter at a rate of 1 $K \cdot min^{-1}$ under nitrogen cover gas was used in an attempt to determine the martensite start (M_s) and martensite finish (M_f) temperatures for both samples. Temperatures as low as -140°C were approached with no observable transformation. In addition, Sample 1 was cooled while neutron diffraction spectra were simultaneously obtained. A spectrum obtained at -253°C by cooling with liquid helium confirmed that the B2 high-temperature austenitic structure was stable at that temperature. The stable nature of the austenitic phase is discussed in detail in the next chapter.

3.3 Single Peak Fitting

By fitting individual lattice peaks, strains with respect to the unloaded state can be determined for specific grain orientations along the corresponding lattice directions. The algorithm TOFMANY [46] was used to fit the individual lattice reflections, which takes into account the inherently asymmetric peak shapes present in the LANSCE pulsed source. Strain for a plane (hkl) at a given stress is reported as:

$$\varepsilon_{hkl} = \frac{d_{hkl} - d_0}{d_0} \qquad \text{..... 3.1}$$

where d_{hkl} is the spacing of the plane (hkl) at a given stress and d_0 is its spacing in the unloaded condition. In practice, a small nominal stress of up to 8 MPa was used as the "zero stress" condition to hold the specimen horizontally in the rig. Since the strains are calculated relative to the initial state of the specimen, the presence of initial residual intergranular stresses are ignored.

Strains from individual lattice reflections are reported only for the austenite phase. Martensitic peaks could not be used to characterize strains because a d_0 value for the nascent martensite cannot be easily determined. In addition, there are a large number of peaks associated with the low-symmetry martensite, many of which overlap.

The simplest approach to determining the volume fraction of martensite (V_{mar}) is from the integrated intensity of the austenitic peaks I:

$$V_{mar} = 1 - V_{aus} = 1 - \left(\frac{I_{hkl}}{I^0_{hkl}} \right) \qquad .....3.2$$

where the volume fraction of austenite (V_{aus}) is determined from I_{hkl} and I^0_{hkl}, the integrated normalized (hkl) intensities at the applied stress and at zero stress after training. The normalization is carried out so that the number of total counts in the spectra are the same. In the case where there is no change in texture in the austenite, the various peak reflections should ideally give the same volume fraction of martensite. If all the austenite grains were oriented identical to their orientation at the no load condition, then as the austenite transformed to martensite the peak intensities would simultaneously decrease at the same rate giving V_{mar} values independent of (hkl) from Eq. 3.2. However, if the texture changes then the corresponding changes in the peak intensities would result in different V_{mar} values from the different (hkl) intensities.

3.4 Rietveld refinement

Instead of limiting analysis to single peaks, the Rietveld refinement method provides a mathematical model describing the intensity, Y_c, at every point in the spectrum:

$$Y_c = Y_b + \sum_h SKF_h^2 P(\Delta T_h) \qquad ..... 3.3$$

where the first term Y_b is the background intensity and the second term is the Bragg scattering containing a structure factor F_h, a scale factor S, a correction factor K, and a profile function $P(\Delta T_h)$, determined by the displacement ΔT_h of the profile point from the reflection position. The correction factor K contains a term describing the changes in the predicted powder intensity due to texture. The refinement procedure optimizes various parameters related to phase volume fractions, atom positions and texture until the calculated spectrum exhibits an optimum least

squares fit with the measured spectrum. Errors where significant are reported and arise from the statistics associated with such a least squares fit.

3.4.1 Strain description

Within the Rietveld refinement, isotropic and anisotropic components of the strains are accounted for by using a strain description that incorporates three parameters, α, β and γ:

$$\varepsilon_{hkl} = \frac{\alpha}{C} - \frac{\beta Cos\phi}{C} - \frac{\gamma A_{hkl}}{C} \qquad .....3.4$$

where C is the diffraction constant for the instrument (since the peak position change is in units of time for time-of-flight data, dividing by C gives d spacing). The first fitting parameter α is varied so that $\Delta a/a = \Delta b/b = \Delta c/c$ (where a, b and c are the lattice constants) and hence is the strain along <100> i.e.,

$$\frac{\alpha}{C} = \varepsilon_{h00} \qquad .....3.5$$

Thus α may at least be considered an empirical isotropic strain when used by itself (i.e., when β and γ are zero in the fit). The second fitting parameter β accounts for the anisotropy in a given direction where ϕ is the angle between [hkl] and a fixed axis. For the martensite the fixed axis was [100]. Following Daymond et al. [47], a cubic anisotropy factor γ was also used to shift the position of each peak from a perfect cubic structure by a quantity proportional to γA_{hkl}, where A_{hkl} is given by:

$$A_{hkl} = \frac{h^2k^2 + h^2l^2 + k^2l^2}{(h^2 + k^2 + l^2)^2} \qquad .....3.6$$

For a cubic single crystal, the single crystal plane specific modulus, E_{hkl}, can be expressed as [48]

$$\frac{1}{E_{hkl}} = S_{11} - 2(S_{11} - S_{12} - \frac{S_{44}}{2})A_{hkl} \qquad ..... 3.7$$

where S_{ij} is the single crystal compliance tensor in collapsed matrix notation.

Only the parameters α and γ were used to fit the cubic austenitic phase. In the case of the monoclinic martensite, all three parameters were used: the parameter γ, which does not capture

any physics of the deformation for the non-cubic case, was used so that an additional degree of freedom would facilitate convergence in the least squares fit in the Rietveld refinements.

The above description applied to a refinement where spectra from all three scattering geometries were used. Another series of refinements was performed using only the spectrum perpendicular to the loading axis (possible since the incident beam is polychromatic) that included reflections from all lattice planes with a d spacing between 0.6Å to 4.0Å. Then, only α was used to describe the strain evolution in the austenite and the martensite, and the parameters β and γ were always set to zero.

3.4.2 Texture formulations

Within the correction factor K in Eq. 3.3 is a term which describes the change in Bragg intensity for a reflection due to texture. Two differing approaches were used. In the first, following the formulation of March and Dollase [37, 38], a cylindrical symmetrical version of an ellipsoidal model was used to describe the texture. Data from a single detector was analyzed with the General Structure Analysis System (GSAS) [39] using the March-Dollase formulation. The detector chosen included reflections from lattice planes perpendicular to the loading axis. The profile which fitted best the data is a combination of two functions: the first is the result of convoluting two back-to-back exponentials with a Gaussian and the second is a linear combination of a Lorentzian and a Gaussian (pseudo-Voigt). Fig. 3.1 shows a typical output for such a refinement for Sample 2 at 625 MPa during loading.

Recently, a generalized spherical-harmonics description of the orientation distribution function (which maps the probability of each of the possible grain orientations with respect to the external sample dimensions) has been incorporated into GSAS. Using two sets of neutron time-of-flight data from a standard calcite sample previously used for a round-robin study, von Dreele [49] showed that the new technique gives texture results identical with those obtained from individual reflection pole figures. Using NiTi data from all three detectors, a refinement was performed using an 8^{th} order spherical-harmonics description with a profile function identical to that described above for the March-Dollase formulation.

3.5 Results

Fig. 3.2 shows the macroscopic stress-strain responses of superelastic NiTi Samples 1 and 2 tested in the neutron beam. Accordingly with increasing stress, the austenite is first elastically deformed before transforming to martensite. For Sample 2, the transformation is complete and results in further elastic deformation of the transformed martensite. On unloading, the stress-induced martensite becomes unstable and transforms back to austenite (with concurrent elastic and superelastic recovery), so that all the strain is recovered.

As shown by the strain plateaus of Sample 1 at the stresses where the testing machine was stopped, the sample accumulated strain before reaching within a few minutes the stable strain levels marked with black dots. This effect can be attributed to the relatively high loading rate which did not allow sufficient time for dissipation of the transformation enthalpy [50-52]. Since the transformation is thermoelastic, strain is produced upon equilibrating to the ambient temperature. This phenomenon occurred in the first few minutes after the load had been stabilized and thus had no significant effect on the neutron measurements which lasted about 6 h.

Comparison of Sample 1 and 2 in Fig. 3.2 shows that the stress at which martensite forms and reverts back is lower in the case of the former sample. As described previously, these samples are physically identical (Sample 2 was obtained by machining Sample 1) and were subjected to the same thermomechanical treatments. However, the mechanical response of NiTi is very sensitive to temperature changes (an increase of 1 K may require an additional 4-20 MPa to initiate the transformation [10]). Thus the above difference can be attributed to a slight difference in testing temperature, e.g., a slightly different level of air cooling of the hydraulic equipment in the enclosed testing volume. This may have increased the ambient temperature by a few degrees for Sample 2, but the temperature during the entire cycle was uniform as evidenced from the lack of plateaus in the stress-strain response for that sample. Recognizing this impact of testing temperature on stress, data from Samples 1 and 2 have only been combined when the superelastic strain is reported since, unlike stress, it is a fundamental global quantity characterizing the phase strains, phase fractions and texture evolution in the transformation independently of temperature. Fig. 3.3 shows selected normalized spectra corresponding to stresses in the stress-strain curve in inset. The evolution of the various peaks corresponding to the austenite and martensite phases reflect the general trends in the phase evolution as a function of the applied stress. Fig. 3.4 seeks to investigate the austenite as it transforms to martensite and

shows portions of the spectra corresponding to the (110) and (100) peaks of the austenite at various load levels. For clarity the martensite reflections (where present) are subtracted from the spectra. Spectra are from the detector where the scattering vector is parallel to the loading axis (i.e., reflections from lattice planes perpendicular to the loading axis are shown). The spectra are normalized so that the (110) peak at all stress levels have the same area. Thus any change in the (100) peak intensity after normalization implies a change in texture in the austenite.

Fig. 3.5 shows the volume fraction of martensite (as determined from the intensities of individual lattice reflections using Eq. 3.2) as a function of the superelastic strain during loading for Sample 1. Superelastic strain refers to the total macroscopic strain measured by extensometry, from which the elastic contribution was subtracted. This contribution is calculated using an elastic modulus of 51 GPa, determined from a fit to the linear elastic region in the macroscopic stress-strain data for Samples 1 and 2 from Fig. 3.2. Since the macroscopic strain is much larger than the elastic strain, this elastic correction is small. The general shape of these curves is not affected even for an upper bound modulus of 125 GPa, corresponding to perfectly textured martensite [31]. Fig. 3.5 also shows the volume fractions of martensite as determined from Rietveld refinements using the March-Dollase and spherical-harmonics texture formulations.

Fig. 3.6 shows the lattice parameter of austenite and computed strains in the austenite (referenced to the lattice parameter in the no load condition) as a function of the external applied stress, as determined from both March-Dollase and spherical-harmonics texture descriptions during loading and unloading for Sample 1.

Fig. 3.7 shows the volume fraction of martensite formed as a function of the superelastic strain as determined from both March-Dollase and spherical-harmonics texture formulations. Data is included here from both Samples 1 and 2 and the load and unload parts of the cycle. Significant qualitative and quantitative differences are noted. As justified in the next section, the spherical-harmonics texture formulation is used in all further refinements in this work. Fig. 3.8a and Fig. 3.8b show strains for individual peaks (from Eq. 3.1) in the austenite as a function of the external applied stress during loading and unloading for lattice planes perpendicular to the loading direction, i.e., for strains in the direction of the applied load. Also shown is the strain obtained from a Rietveld refinement where only α is varied (β=0 and γ=0 and hence $\varepsilon_{hkl}=\varepsilon_{h00}$ from Eq. 3.4) for Sample 1. Varying only ε_{h00} for the austenite in the Rietveld refinement gives

an average representation of the individual lattice planes in the austenite. The individual lattice plane strains are referenced to the d spacing after training under no stress, neglecting any intergranular stresses.

As mentioned earlier, two sets of refinements were performed for each stress level using the spherical-harmonics texture formulation. In the first case only α was varied for both austenite and martensite, while in the other case α and γ were varied for the austenite, and α, β and γ for martensite. Fig. 3.9a and Fig. 3.9b show values of ε_{h00} (in the set of refinements where only α was varied) against γ/C (in the set of refinements where α and γ were varied) for the austenite during the load and unload part of the cycle for Sample 1. A distinct change in slope in these graphs is observed corresponding to changes in the anisotropic component of the strain in the austenite. Fig. 3.10 and Fig. 3.10b show ε_{h00} with γ=0 and γ fitted during loading and unloading for Sample 1. Fig. 3.11a and Fig. 3.11b are the corresponding figures for Sample 2 during unloading. Fig. 3.12a and Fig. 3.12b compare the individual lattice plane strains obtained from the Rietveld refinement (Eq. 3.4) with those obtained by profiling single peaks for the austenite during loading in Sample 1. Fig. 3.13a and Fig. 3.13b are the corresponding curves during unloading in Sample 1. Again, the above figures are shown for the lattice planes perpendicular to the loading direction, i.e., for strains in the direction of the applied load.

3.6 Discussion

The stress-induced transformation from austenite to martensite and its back transformation are observed macroscopically as plateaus in Fig. 3.2. A qualitative examination of the peaks corresponding to the austenite and martensite phases in Fig. 3.3, confirms that these transformations occur within the bulk, and can be observed from diffraction spectra owing to their different crystallographic structures. Measurements on Sample 1 in Chapter 2 did not observe a complete transformation to martensite as observed from the spectrum obtained at 975 MPa in this figure for Sample 2.

Fig. 3.4 shows for the austenite the normalized (100) peaks disappearing as the load increases and the austenite transforms to martensite, and reappearing upon unloading and back-transformation. From the scattering geometry, this evolution corresponds to transformation occurring preferentially in austenite grains with their (100) planes aligned perpendicular to the

loading axis, as compared to grains with their (110) planes aligned perpendicular to the load. If transformation occurred istropically (i.e., there was no preferential disappearance but rather a random transformation to martensite), the normalized (100) spectra would show a constant intensity. This preferential disappearance of favorably-oriented grains also explains why using different peak intensities in Eq. 3.2 yields different volume fraction of martensite in Fig. 3.5. For example, if the phase fractions are inferred from single-peak reflections alone, the (111) austenite reflection suggests that 50 vol.% martensite is present at maximum strain while the complete disappearance of the (100) austenitic peaks suggests the presence of 100% martensite. Due to the nature of the transformation, the martensite that is formed can be expected to exhibit a strong texture. The texture may further be enhanced by deformation twinning in the martensite. Thus, it is important to examine and model the evolving texture during the stress-induced formation of austenite to obtain accurate phase fractions of the martensite and austenite during the transformation.

A striking difference between the March-Dollase and the generalized spherical-harmonics formulations used to quantify this texture evolution is seen in Fig. 3.5. The volume fraction predicted by the March-Dollase formulation in the Rietveld refinement is much higher that the volume fraction predicted by using a spherical-harmonics formulation as seen in Fig. 3.5. In Fig. 3.5, the March-Dollase results overlaps with the most intense peaks (100) and (210) while the spherical-harmonics approach tracks a more average behavior of the peaks. The average strain in the austenite phase (calculated with the lattice parameter at zero stress after training as reference) is shown in Fig. 3.6 and the differences are larger at higher stresses where more martensite exists. In Fig. 3.7, the non-linear slope of the March-Dollase texture curve suggests that the martensite forming at high stress contributes more macroscopic uniaxial average strain than the martensite forming at low stress. This is physically unlikely since it has been observed that the texture is lower for martensite formed at higher stresses than at low stresses. The texture index (Eq. 4.4) of the martensite during loading as defined by Bunge [45] is 5.0 at 490 MPa as compared to 2.6 at 975 MPa (see Chapter 5 for more details). This leads to certain peaks in the martensite (e.g. the (100) plane) having very high relative intensities. The difference between the March-Dollase and the spherical-harmonics texture formulation can also be explained on the basis of these high relative intensities. Given the number of variables in the Rietveld refinement and the amount of neutron data used, the simple elliptical March-Dollase

model overestimates the volume of martensite formed since these high intensity reflections are over-weighted. This overestimation of the volume of martensite is also confirmed by a qualitative check of the unprocessed diffraction spectra. In the light of the preceding discussion, the generalized spherical-harmonics description of the texture is used in further analysis of the data.

At low stress levels, the stress-strain behavior observed in the different lattice planes is quite linear and similar in Fig. 3.8a and Fig. 3.8b. This suggests that the austenite phase is fairly isotropic, in agreement with ultrasonic measurements by Brill et al. [53], who report a value of 1.94 for the anisotropy factor $(2C_{44}/(C_{11}-C_{12})$, where C_{ij} is the stiffness tensor. The anisotropy factor has a value of unity for perfect isotropy. We note again that all the lattice planes have been assumed to be stress free at the no load state in Fig. 3.8a and Fig. 3.8b. This may not be true due to intergranular strains as observed from the d_0 spacing of the austenite planes at zero stress. Using a d_0 value to compute a lattice parameter from $d_0/(h^2+k^2+l^2)^{0.5}$ results in an average lattice parameter of 3.0043 Å. On the basis of this simple calculation, the effect of intergranular strains seems to be largest in (100) and (110). The strain is tensile $(9\cdot10^{-4} \pm 3\cdot10^{-4})$ in the case of (100) and compressive $(6\cdot10^{-4} \pm 3\cdot10^{-4})$ in the case of (110), when compared to the average lattice parameter. However, these possible differences in the residual intergranular strains are negligible compared to the elastic strain developing upon mechanical deformation.

As noted before, certain preferred orientations of austenite grains transform to martensite first. This leads to strain redistribution between the grains and the elastic response of the austenite lattice reflections are no longer linear and similar. To satisfy compatibility between the textured martensite and the austenite phases, load transfer due to mismatch results in additional strain anisotropy in the austenite phase. For example the (100), (210), (320) and (311) reflections deviate significantly in Fig. 3.8a and Fig. 3.8b. Thus the stress-induced austenite to martensite transformation behavior of NiTi is analogous to slip in metals in terms of the individual lattice plane responses, even though in the present case all the strain is reversible on unloading [47, 54]. As expected, the Rietveld strain ε_{h00} (with only α as a variable) gives an average isotropic response as seen by the bold line in Fig. 3.8a and Fig. 3.8b.

The anisotropy in the lattice plane responses in the austenite phase is described in the Rietveld refinements by using the γ parameter in Eq. 3.4. The γ parameter can be considered to have contributions from elasticity, plasticity associated with slip and the phase transformation:

$$\gamma = \gamma_{el} + \gamma_{sp} + \gamma_{tran} \quad \text{..... 3.8}$$

The slip contribution, γ_{sp}, is set to zero because no slip is associated with the macroscopic stress-strain curve, as shown by the full strain recovery on unloading (Fig. 3.2). In Fig. 3.9a and Fig. 3.9b, the y-axis is a measure of the average isotropic strain in the austenite (ε_{h00} while only α was refined and γ=0) while the x-axis is a measure of the anisotropy. The absolute value of γ is not important as redefining the stress-free state (i.e., the stress-free lattice constant) of the austenite can redefine the x-axis. In Fig. 3.9a, the anisotropy factor initially decreases in magnitude but begins to increase around a strain level of $3.2 \cdot 10^{-3}$ (ε_L) in the austenite. The reason for this unusual behavior of the anisotropic component of the strain in the austenite phase is not clear. The elastic component of the anisotropy is always present and introduces variations in individual lattice plane response of the austenite. It is physically difficult to explain the change in the slope of γ from the γ_{el} contribution alone, suggesting an effect due to γ_{tran}. The anisotropy factor $2C_{44}/(C_{11}-C_{12})$ for nascent, thermally-formed martensite is 0.52 as reported by Brill et al. [53], using the lattice basis of the parent austenite. The anisotropy factor in terms of the compliance elements is $2(S_{11}-S_{12})/S_{44}$ i.e., $2C_{44}/(C_{11}-C_{12}) = 2(S_{11}-S_{12})/S_{44}$. Thus a change in the value of $2C_{44}/(C_{11}-C_{12})$ from 1.94 to 0.52, corresponding to the change of a single crystal of austenite to martensite, will take $S_{11}-S_{12}-S_{44}/2$ through a sign reversal. In Eq. 3.7, A_{hkl} is related to the anisotropic contribution to the modulus by $S_{11}-S_{12}-S_{44}/2$. This anisotropic contribution to the modulus is analogous to the anisotropic contribution to the strain in Eq. 3.4 with γ being equivalent to $S_{11}-S_{12}-S_{44}/2$. This change may be responsible for the unusual anisotropic behavior observed in the austenite phase. The unique lattice correspondence between the austenite and martensite phase along with the stress and strain compatibility of austenite and martensite as they co-exist during the transformation results in the austenite reflecting the anisotropy of the martensite. The strain level, ε_L, also seems to correspond to the onset of deviation from linearity in the stress-strain response of (100) (Fig. 3.8a). The strain level, ε_L, represents a strain in the austenite phase and cannot be directly compared with the strain from an extensometer in NiTi (i.e., both austenite and martensite phases) because of the mechanics of load partitioning. From Fig. 3.8a, an external applied stress level of 212 MPa corresponds to the ε_L strain level in the austenite. This stress level is represented by the dotted line at 212 MPa in the inset in Fig. 3.2. The onset of the stress-induced transformation (as defined by the first deviation from linearity in

the macroscopic stress-strain response in Fig. 3.2) occurs near this stress level. The difference, if real, can be attributed to some initial γ_{tran} contribution to γ, canceling the γ_{el} contribution since they appear to act in opposite directions.

Fig. 3.10 shows the strains in the austenite phase from the two sets of refinements i.e. with γ=0 and with γ fitted. The general trends observed seem to again verify the above proposed anisotropic contribution from the transformation. It is tempting to conclude that Fig. 3.9a and Fig. 3.10a (and consequently also Fig. 3.9b and Fig. 3.10b) do not contain independent information. However, they validate each other since no constraint was put on γ and α when they were used simultaneously in the refinement i.e. they were allowed to be refined independently. It is to be noted that when γ is fitted, the x-axis has no absolute value and hence the need to limit the discussion to trends. Fig. 3.11 shows the corresponding curves for Sample 2. Here no stress levels are reported due to lack of statistically robust data. Sample 2 was used mostly to reach a complete transformation to martensite (Fig. 3.2) rather than to study intermediate stress levels.

The same trend is repeated during the unload part of the cycle for Sample 1 in Fig. 3.8b. The hysteresis between the load and the unload part of the cycle is captured very well. The stress level corresponding to $\varepsilon_L=3.2\cdot10^{-3}$ during loading is 212 MPa while the stress level corresponding to $\varepsilon_{UL}=2.3\cdot10^{-3}$ during unloading is 144 MPa i.e., there is a difference of 68 MPa. The stress at which the anisotropy changes in the unload part of the cycle corresponds to (a) the finish of the martensite to austenite back transformation as shown by the dotted line at 144 MPa in the inset in Fig. 3.2 and (b) the finish in the deviation from linearity in the stress-strain response of (100) (Fig. 3.8b). Again, the relatively small difference can be attributed to some initial γ_{tran} contribution to γ canceling the γ_{el} contribution. Fig. 3.12a and Fig. 3.12b compare the individual lattice plane strains obtained from the Rietveld refinement (Eq. 3.4) with those obtained by fitting single peaks for the austenite during loading in Sample 1. At the lower stress levels both techniques compare very well. However there are some deviations at higher stress levels especially in Fig. 3.12b. The simple hkl dependence of γ through A_{hkl} (which is restricted to values between 0 and 1/3) was originally formulated to capture the elastic anisotropy. We have extended the same formulation to try to describe the anisotropy due to the transformation. A more rigorous relationship may further improve the fits. Fig. 3.13a and Fig. 3.13b show the same trend during the unload part of the cycle.

While the current strain description incorporating an anisotropy factor works very well with the cubic austenite, it remains to be seen if the fitting parameter β (Eq. 3.4) can be used to generate some information on the monoclinic martensite. This was impossible in the present work since more emphasis was placed on correctly modeling the texture and volume fraction of the martensite. This was done so that convergence could be obtained in the least squares fit with the Rietveld refinement. Thus β and γ served merely as fitting parameters for the monoclinic phase without any associated physical significance. However, it is suggested that working with very large volume fractions of martensite (>90%) or and not using γ might provide some information on the use of β in this work.

3.7 Conclusions

Neutron diffraction measurements have been used to investigate stress-induced austenite to martensite transformations in superelastic NiTi. The evolving texture is found to play a significant role in the transformation and needs to be correctly accounted for to accurately quantify volume fractions of martensite and austenite during the transformation. The texture was formulated using two different approaches i.e., the March-Dollase formulation and a generalized spherical-harmonics approach. The strain description used in the Rietveld refinement gives an average response to the various (hkl) planes in good agreement with data from single peaks. An anisotropy factor is used that helps to predict individual lattice plane responses. The anisotropic component of the discrete phase strain description of the austenite exhibits unusual behavior i.e., undergoes a reversal in direction. This seems to correspond to the onset of the austenite to martensitic transformation and the conclusion of the back transformation and may be due to the additional anisotropy introduced by the transformation.

In addition the evolving texture in the martensite is of interest and is discussed in the context of crystallography and transformation strains in detail in Chapter 6. This work has established a methodology to ascertain the discrete phase strains, phase volume fractions and texture during stress-induced transformations to be used in future investigations of the mechanics of load transfer and stress cycling in superelastic NiTi and superelastic NiTi-TiC composites in later chapters.

3.8 Figures

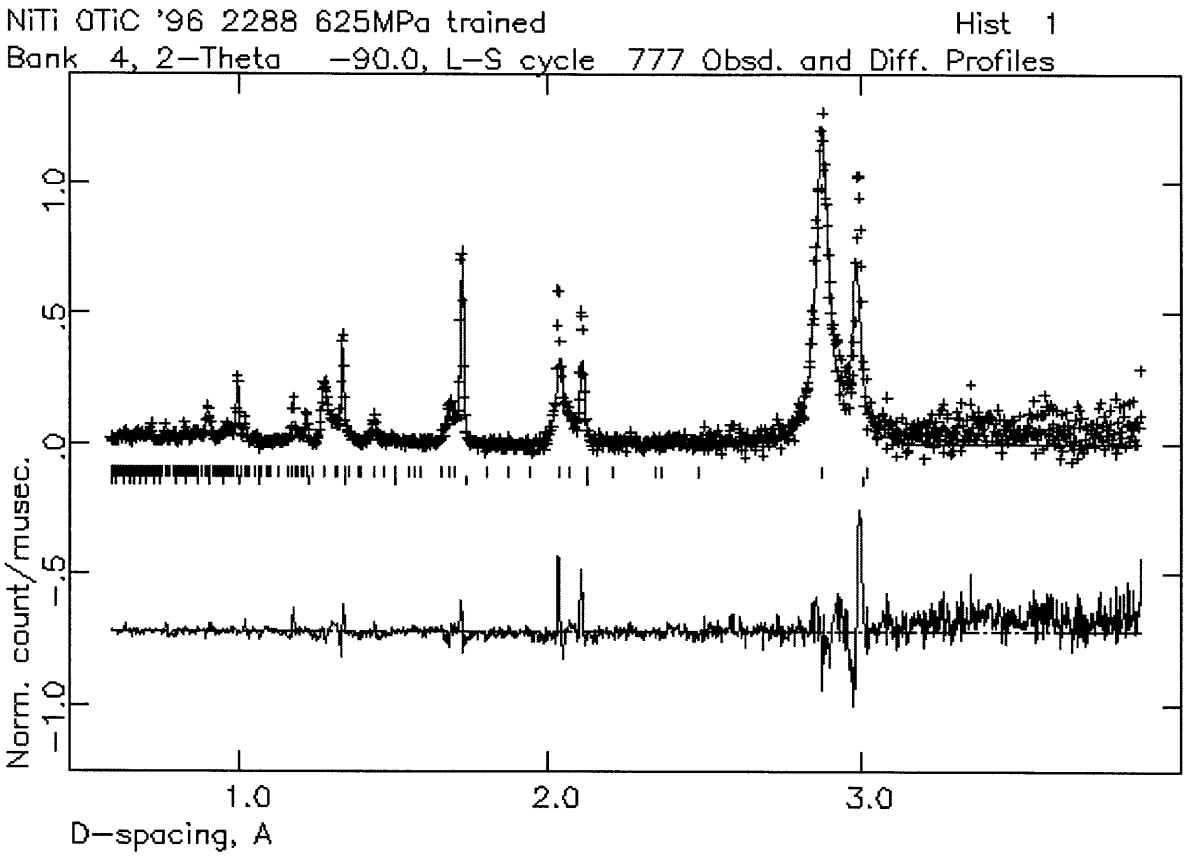

Fig. 3.1 A typical GSAS Rietveld refinement output (shown here for Sample 2 at 625 MPa) for diffracting lattice planes perpendicular to the load. The crosses are the measured spectra; the line through them is the Rietveld least squares fit, using a spherical harmonics texture formulation for the texture. The tick marks indicate reflections from the martensite and austenite phase. The difference curve between measurement and refinement is also shown.

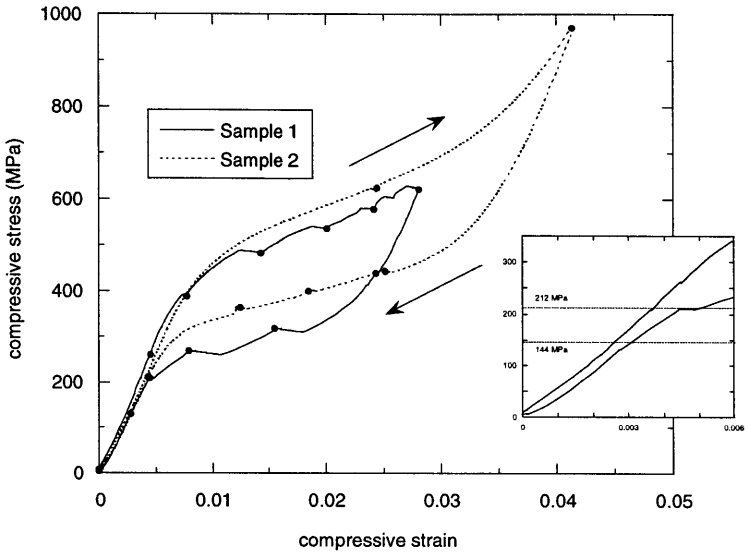

Fig. 3.2 Macroscopic stress-strain response of superelastic NiTi Samples 1 and 2 which were tested in the neutron beam. The points indicate the stress levels at which the mechanical cycles were stopped and neutron diffraction spectra obtained. The inset shows the starting and ending regions of the transformation for Sample 1.

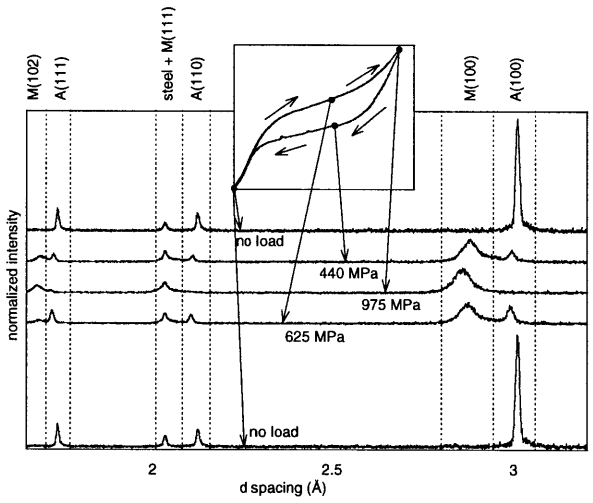

Fig. 3.3 Section of normalized neutron spectra from Sample 2 at various stress levels (see inset) to show martensite and/or austenite phases with the austenite (A) and martensite (M) peaks identified. Diffraction from steel in the extensometer knife edges contaminates the M(111) reflection. This was determined to have no effect on the refinement.

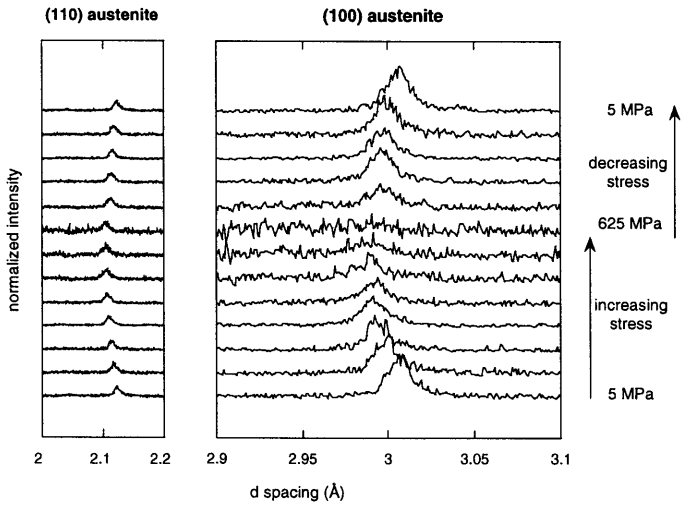

Fig. 3.4 The (110) and (100) peaks in austenite after the martensite peaks (where present) have been subtracted out for clarity from Sample 1; the spectra are normalized so that the (110) peaks at all stress levels have the same area.

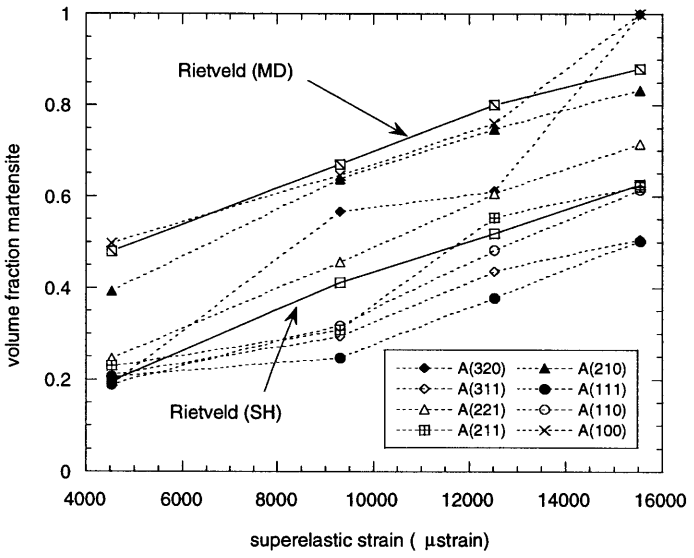

Fig. 3.5 Volume fraction of martensite as a function of the superelastic strain for Sample 1 during loading. The volume fraction is determined from the intensities of individual lattice reflections (Eq. 3.2) and by performing refinements on the spectra using both March-Dollase (MD) and spherical harmonics (SH) texture formulations.

(a)

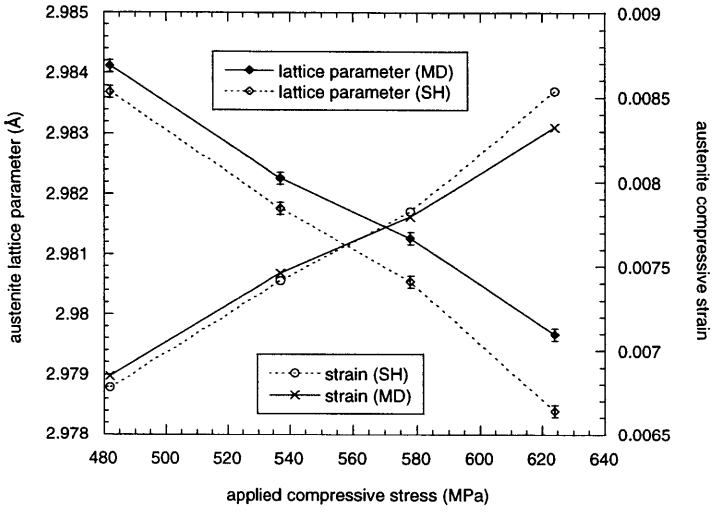

(b)

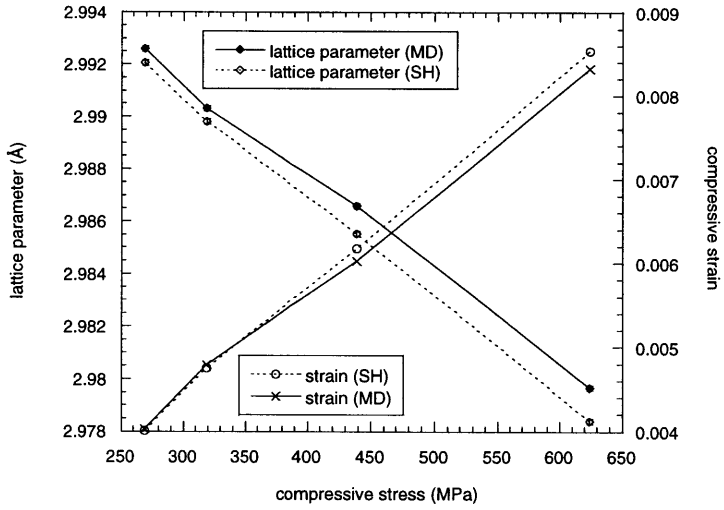

Fig. 3.6 Lattice parameter and computed strain in austenite as a function of the applied external stress as determined from both March-Dollase (MD) and spherical harmonics (SH) texture descriptions during (a) loading and (b) unloading for Sample 1.

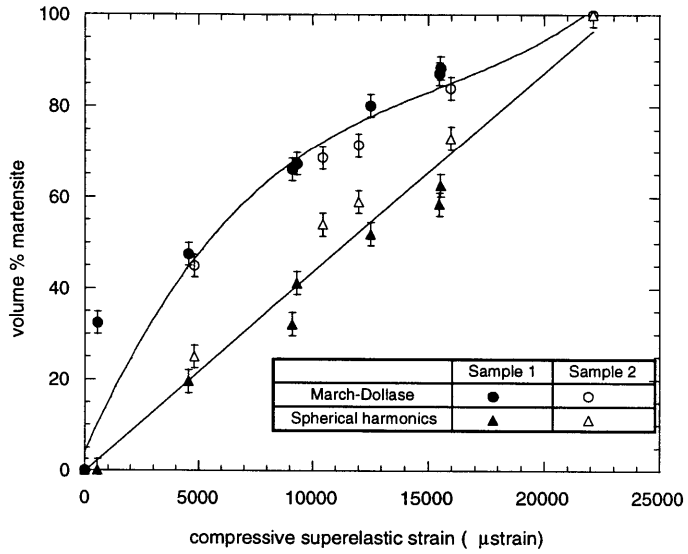

Fig. 3.7 Relationship between the volume (%) of martensite formed and the superelastic strain (total strain minus the elastic contribution) from both March-Dollase and spherical harmonics texture formulations. Data from both the load and unload portion of the mechanical cycle are included for Samples 1 and 2.

(a)

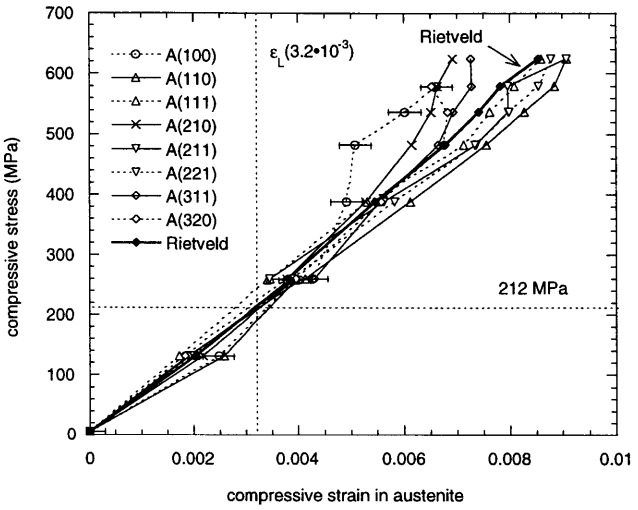

(b)

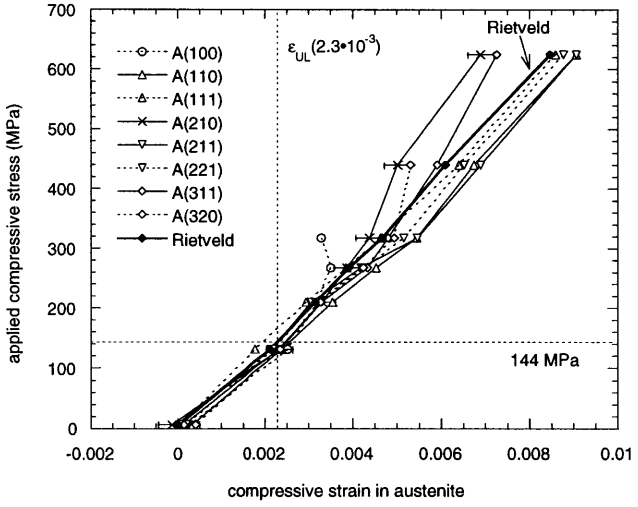

Fig. 3.8 The stress-strain response of individual lattice reflections in austenite during (a) loading and (b) unloading for Sample 1. ε_{h00} (with γ=0) from the Rietveld refinement gives a very good average representation. ε_L and ε_{UL} are strain levels at which the anisotropy due to the transformation dominates in (a) and diminishes in (b) as determined by the γ parameter. For clarity, typical error bars for peak profiling are shown only on (100) in (a) and (210) in (b) and are similar in magnitude for other peaks.

(a)

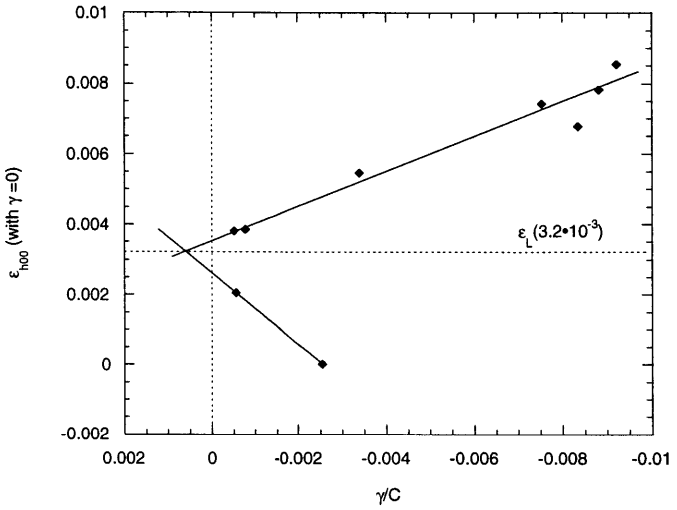

(b)

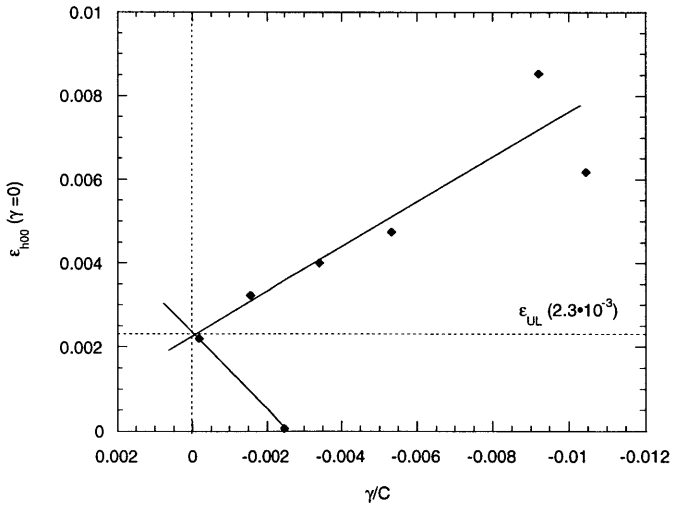

Fig. 3.9 ε_{h00} (with γ=0) as a function of γ/C for austenite during (a) loading and (b) unloading for Sample 1. ε_L and ε_{UL} are the strain levels ($3.2 \cdot 10^{-3}$ in (a) and $2.3 \cdot 10^{-3}$ in (b)) where changes in slope are observed. The diffractometer constant C is used to change γ time-of-flight values into strain.

(a)

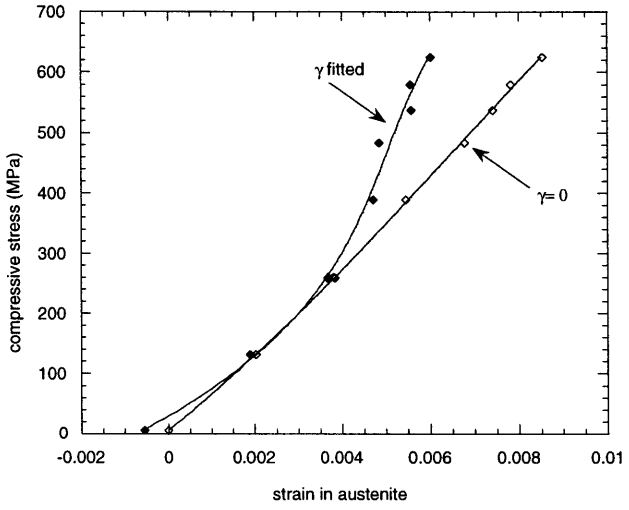

(b)

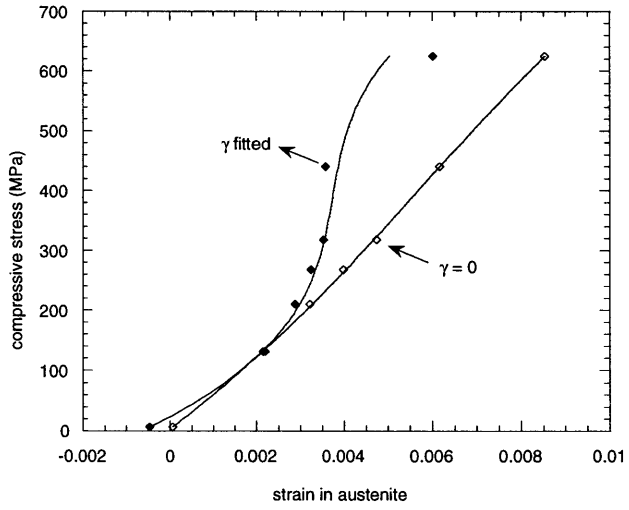

Fig. 3.10 ε_{h00} with $\gamma=0$ and $\gamma\neq0$ in austenite as a function of the applied external stress during (a) loading and (b) unloading for Sample 1 . Lines are meant to merely guide the eye.

(a)

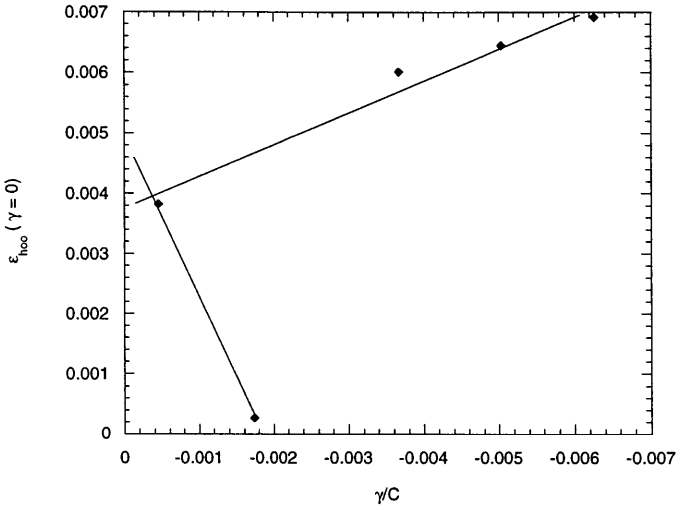

(b)

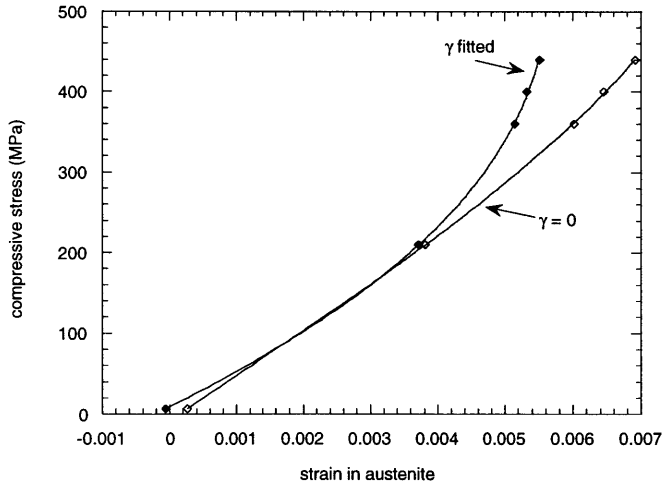

Fig. 3.11 (a) ε_{h00} (with γ=0) as a function of γ/C for austenite during unloading for Sample 2. The same trends as in Fig. 3.9 and Fig. 3.10 are seen. The diffractometer constant C is used to change γ time-of-flight values into strain. (b) ε_{h00} with γ=0 and $\gamma \neq 0$ in austenite as a function of the applied external stress during unloading for Sample 2 . Lines are meant to merely guide the eye.

(a)

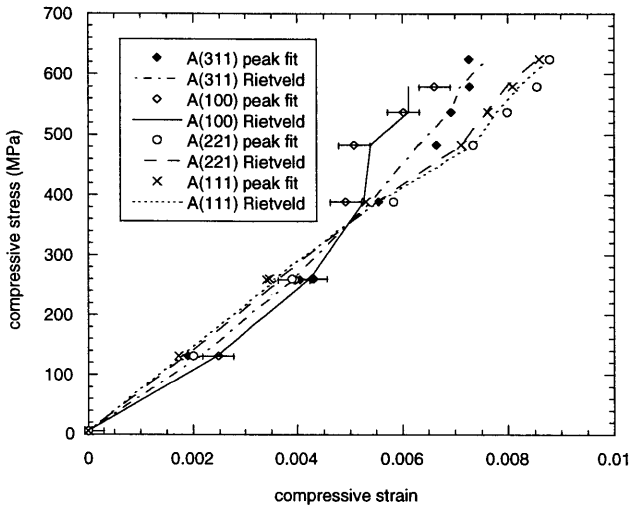

(b)

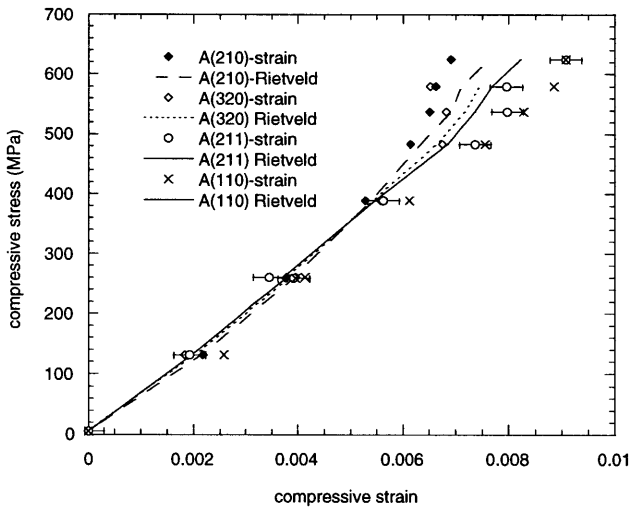

Fig. 3.12 Strains for individual austenite lattice reflections as determined by peak profiling and a Rietveld refinement (Eq. 3.4) as a function of the external applied stress during loading for Sample 1. For clarity typical error bars for the peak profiling are shown only on (100) in (a) and (211) in (b) and are similar in magnitude for other peaks.

(a)

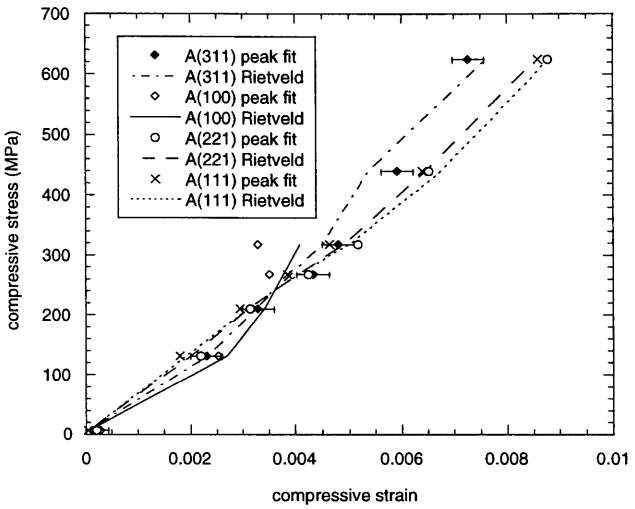

(b)

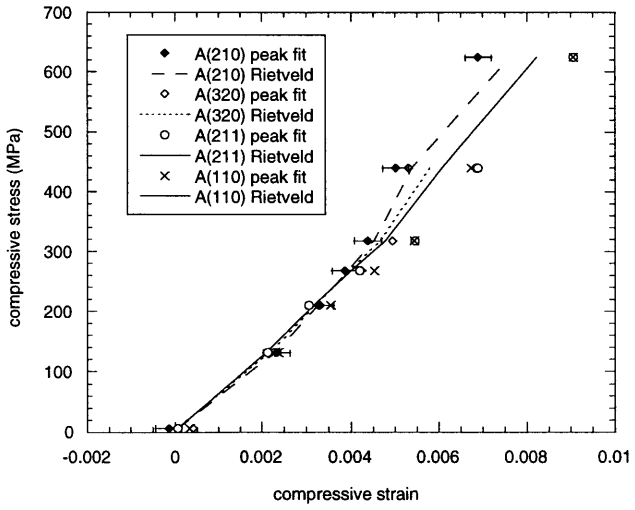

Fig. 3.13 Strains for individual austenite lattice reflections as determined by peak profiling and a Rietveld refinement (Eq. 3.4) as a function of the external applied stress during unloading for Sample 1. For clarity typical error bars for the peak profiling are shown only on (311) in (a) and (210) in (b) and are similar in magnitude for other peaks.

Chapter 4

Study of Superelastic NiTi and NiTi-TiC Composites

Superelastic NiTi (51.0 at.% Ni) reinforced with 0, 10 and 20 vol.% TiC particles were deformed under uniaxial compression while neutron diffraction spectra were collected. The experiments yielded in-situ measurements of the thermoelastic stress-induced transformation in the presence of TiC particles. The evolution of austenite/martensite phase fractions, texture and of elastic strains (both isotropic and anisotropic components) in the reinforcing TiC particles and the austenite matrix were obtained by Rietveld refinement during the loading cycle as the austenite transforms to martensite (and its subsequent back transformation on unloading). Phase fractions and strains are discussed in terms of load transfer in composites where the matrix undergoes a stress-induced phase transformation. Eshelby's elastic theory is used to predict the discrete phase strains and good agreement is observed between theory and measurements suggesting that the self-accommodation of the stress-induced martensite almost minimizes the transformation mismatch with the TiC particles.

4.1 Introduction

Since the NiTi phase transformation is thermoelastic, internal or external stresses can significantly affect the behavior of these alloys. The internal stresses in NiTi can be due to mismatch between grains, dislocations, precipitates or second phases. Extensive studies have been performed for metal matrix composite systems with stiff ceramic reinforcing phases where the matrix primarily deforms by slip at high stresses. However, for the case of composites comprising of matrices involving alternative deformation mechanisms, e.g., twinning or stress-induced transformations, relatively little knowledge is available in the scientific literature. The thermoelastic phase transformation and/or twinning deformation in NiTi can be expected to be affected by stiff ceramic particles that produce internal stresses or partition externally applied stresses. Consequently, the mechanical deformation behavior of such composites are worthy of investigation.

Dunand and co-workers have carried out a series of investigations to systematically characterize such NiTi based shape-memory composites (martensitic NiTi matrix reinforced with TiC). The thermal transformation behavior [55, 56], the bulk mechanical properties in compression [57], the subsequent shape-memory recovery [58] and the study by neutron diffraction of twinning deformation and shape-memory recovery [30, 31] have been investigated.

The key results from these investigations have been summarized in [59]. To the best of our knowledge there has been no analysis providing information on the mechanical behavior of an austenitic NiTi matrix with a reinforcing ceramic phase where the matrix is capable of reversibly forming stress-induced martensite from austenite.

Chapter 2 demonstrated the ability to observe stress-induced transformations in NiTi by obtaining neutron diffraction data while NiTi is subjected to loading. Here an attempt is made to further investigate the evolving phase fractions, texture and discrete phase strains in austenitic NiTi and NiTi reinforced with TiC by carrying out neutron diffraction measurements during compression loading.

4.2 Experimental procedures

4.2.1 Sample fabrication

NiTi Prealloyed NiTi powders (99.9% pure, 49.4 at.% Ni, size between 44μm an 177μm, from Specialty Metals Corp., NY) were blended with Ni powders (99.9% pure, size between 44μm and 177μm, from Specialty Metals Corp., NY) and equiaxed TiC powders (99.9% pure, 44μm average size, from Atlantic Equipment Engineers NJ). The powder, packed in a low carbon cylindrical steel container (thickness 0.318 cm, internal diameter 2.5 cm, length 12 cm and lined with a boron nitride coated nickel foil to prevent carbon contamination) was subjected to Hot Isostatic Pressing (HIP) at 1065°C and 100 MPa for 3 h. The final cylindrical samples had the following nominal compositions:

(a) 10 volume % TiC in an austenitic NiTi (51.0 at.% Ni) matrix

(b) 20 volume % TiC in an austenitic NiTi (51.0 at.% Ni) matrix

These compositions will hereafter be referred to as NiTi-10TiC and NiTi-20TiC. The samples were further electrode-discharge-machined into cylindrical specimens 10 mm in diameter and 24 mm in length. These composite samples (NiTi-10TiC (S1) and NiTi-20TiC (S1)) were heat treated as outlined in §2.2 and tested as described in the following section.

Sample NiTi-10TiC (S1) was further reduced in dimension by electrode-discharge-machining to cylindrical samples 8 mm in diameter and 20 mm in length. The heat treatment described previously was again followed. The resulting sample (designated NiTi-10TiC (S2)) was again tested as described below while neutron diffraction spectra were obtained.

4.2.2 Neutron diffraction and mechanical testing

The same setup described in Chapter 2 and 3 was used. Data described previously in Chapter 3 from Sample 1 and Sample 2 (redesignated NiTi-0TiC (S1) and NiTi-0TiC (S2) to be consistent with the composite designations) are used for comparative descriptions. Thus, results from five tests at room temperature corresponding to NiTi-0TiC, NiTi-10TiC and NiTi-20TiC are presented here. The larger samples (S1) were tested up to 625 MPa under uniaxial compression (stroke control at 3 mm/min) while neutron diffraction data were simultaneously obtained. These cycles were obtained after training the sample twice to 625 MPa at a stroke speed of 3 mm/min. The purpose of these training cycles were to stabilize and homogenize the transformation. A systematic evaluation of the effect of such stress-cycling is described in Chapter 6. The smaller samples (S2) were tested up to 975 MPa under uniaxial compression (stroke control at 0.1 mm/min) with simultaneous neutron diffraction. These cycles were also obtained after training the sample twice to 625 MPa at a stroke speed of 3 mm/min. Fig. 4.1 shows the stress levels at which neutron spectra was obtained. Due to limitations in data acquisition time (approx. 6 to 8 hours per stress level), the stress levels were judiciously chosen.

4.2.3 Sample characterization

Optical microscopy (Fig. 4.2) shows that the samples are pore-free and the interface in the composites is unreacted. A uniform distribution of TiC particles are observed in NiTi-10TiC and NiTi-20TiC. The average grain-size was determined to be 20 μm with no statistically significant differences in grain size between the three samples. Density measurements by water-displacement show that NiTi, NiTi-10TiC and NiTi-20TiC are 99.8%, 99.7% and 99.4%, respectively, of their theoretical density as reported in [57].

Differential scanning calorimetry using a Perkin Elmer DSC-7 Calorimeter at a rate of 1 $K \cdot min^{-1}$ under nitrogen cover gas was used in an attempt to determine the martensite start (M_s) and martensite finish (M_f) temperatures for the three samples. Temperatures as low as -140°C were approached with no observable transformation.

4.3 Neutron diffraction data analysis

In the case of a reversible austenite-martensite transformation, grains of austenite do not transform randomly. Grains favorably oriented with respect to the external stress and able to

accommodate the transformation strain transform first and consequently the austenite develops texture. Correspondingly, certain peaks in the spectra disappear first making single peak reflections not representative of the overall transformation. In addition single-peak reflections include anisotropic contributions from crystal geometry and strain redistribution especially arising from the transformation. In the previous chapters these issues have been discussed in detail and a methodology established to analyze diffraction spectra in the case of stress-induced transformations. Here the outcome of that work is summarized with emphasis on determining phase fractions, texture and strain evolution.

A generalized spherical harmonic description is used to account for the evolving texture in the austenite and the martensite phases [45, 49]. The Rietveld refinement [44] procedure using GSAS [39] lets vary various parameters related to phase volume fractions, atom positions and texture until the calculated spectrum matches the measured spectrum in a least squares fit. The profile function which fitted best the data is a combination of two functions - one function is the result of convoluting two back-to-back exponentials with a Gaussian and the other is a linear combination of a Lorentzian and a Gaussian (pseudo-Voigt).

Since loading was uniaxial, the "macroscopic" strain differs parallel and perpendicular to the load direction. An average isotropic strain is used in the austenite phase to capture these effects empirically, shifting the individual (hkl) lattice reflections in the refinement according to changes in the lattice parameter. Thus a strain in the austenite or TiC is reported as

$$\varepsilon_{aus} = \frac{a_s^{aus} - a_0^{aus}}{a_0^{aus}}$$
$$\varepsilon_{TiC} = \frac{a_s^{TiC} - a_0^{TiC}}{a_0^{TiC}} \qquad \text{..... 4.1}$$

where a_s is the austenite or TiC lattice parameter under an applied compressive stress, a_0 is the lattice parameter under no external load. A compressive stress of 8 MPa was used to hold the sample horizontally in the stress rig and corresponds to the "no load" condition. The refinement procedure determines a lattice parameter by fitting many individual reflections and not merely the peak corresponding to the (100) reflection. As shown in Fig. 3.8 in Chapter 3, this representation of the strain (β=0 and γ=0 in Eq. 3.4) tracks the average response of the various lattice planes.

An attempt to capture the anisotropic component of the strain in the austenite (ignored in Eq. 4.1) was also made and the strain described as

$$\varepsilon^{*}_{aus} = \varepsilon^{iso}_{aus} - A_{hkl}\varepsilon^{aniso}_{aus}$$
$$\varepsilon^{*}_{TiC} = \varepsilon^{iso}_{TiC} - A_{hkl}\varepsilon^{aniso}_{TiC} \quad \text{..... 4.2}$$

where A_{hkl} is $(h^2k^2+h^2l^2+k^2l^2)/(h^2+k^2+l^2)^2$. Here the strain is obtained as a contribution of isotropic and anisotropic components. The isotropic component is determined by shifting the individual lattice reflections equally so as to account for a change in the lattice parameter. The anisotropic component shifts the individual reflections proportional to A_{hkl}. The A_{hkl} dependence is introduced given that in a cubic single crystal the single crystal plane specific modulus, E_{hkl}, can be expressed as

$$\frac{1}{E_{hkl}} = S_{11} - 2(S_{11} - S_{12} - \frac{S_{44}}{2})A_{hkl} \quad \text{.....4.3}$$

where S_{ij} is the single crystal compliance tensor in collapsed matrix notation. The A_{hkl} dependence though originally formulated to capture the elastic anisotropy, also captures the anisotropy due to the transformation.

4.4 Results

Fig. 4.1 shows the stress-strain response of the five samples. The plateaus corresponding to the measurements in NiTi-0TiC (S1) and NiTi-10TiC (S1) (more pronounced in the non-linear regions where more martensite is present in NiTi) can be attributed to the higher loading rate and the consequent temperature effects as described in detail in the previous chapter.

Table 4.1 lists the elastic moduli of NiTi-0TiC, NiTi-10TiC and NiTi-20TiC from a fit to the linear portion of the macroscopic stress strain curve. The stress levels at which there is deviation from linearity corresponds to definite formation of the stress-induced martensite during the loading cycle. The unloading cycle gives the stress level at which the reverse transformation to martensite is apparently complete. These values are also shown here. Fig. 4.4 examines the spectra corresponding to NiTi-0TiC, NiTi-10TiC and NiTi-20TiC under stress and at the no load condition. A qualitative examination shows that there is more martensite in NiTi-0TiC than in NiTi-10TiC and even less in NiTi-20TiC. By using data from all three sets of detectors with a generalized spherical harmonic texture formulation in a Rietveld refinement, the amount of martensite present is quantified at the various stress levels. This is shown in Fig. 4.5, where data

obtained in the loading part of the mechanical cycle is distinguished from that obtained during the unloading part. As described in Chapter 3, the superelastic strain is the strain arising from the transformation and does not include the elastic component. The volume fraction is corrected for the fact that only 90% of NiTi-10TiC can transform and the superelastic strain reported is corrected since only 90% of NiTi-10TiC can generate recoverable strain. For NiTi-20TiC, the volume of martensite present could not be quantified from the refinement procedure since even at maximum load less than 10 vol.% of martensite was present. A typical Refinement is shown in Fig. 4.6. The validity of the refinements are further enhanced by the fact that a volume fraction for TiC is not an input parameter but is determined independently. In all cases, the values obtained (10 ± 0.8 vol.% or 20 ± 0.8 vol.% TiC, respectively) are very close to the nominal volume fractions.

In this chapter, the severity of the texture without details of the distribution are presented. The sharpness of the texture is characterized by a single parameter, the texture index J [60]:

$$J = \oint [f(g)]^2 dg \qquad .....4.4$$

where f(g) is the orientation distribution function which maps the probability of each of the possible grain orientations g with respect to the external sample dimensions and the integration is over all orientation space. Using a series expansion and given the orthogonality of generalized spherical harmonics it can easily be shown [45] that J varies between unity and infinity (unity corresponds to random orientation and infinity to one or more ideal single crystals). Some typical values of the texture index are: 2 to 5 for moderate texture (e.g., from rolling), 10 to 15 for a very strong texture (e.g., wire drawing), 70% rolled steel has an index of 3-4, extruded Al has an index of 18. The texture index is presented here to merely indicate trends in the texture evolution. Detailed distribution and orientations are discussed in the next chapter. Fig. 4.7 shows the texture index for martensite in NiTi-0TiC and NiTi-10TiC. The texture index was determined to be inadequate to track the changes in the austenite phase. To investigate the texture evolution in the austenite phase, axial distribution functions are used in the following chapter.

Fig. 4.8 shows the strains obtained from Rietveld analysis (Eq. 4.1) in the austenite phase in NiTi-0TiC during loading and unloading. Fig. 4.9 shows strains obtained from Rietveld analysis (Eq. 4.1) in the austenite and TiC phases of NiTi-20TiC while Fig. 4.10 shows strains obtained from Rietveld analysis (Eq. 4.1) in the austenite and TiC phases of NiTi-10TiC. The above strains represent average isotropic strains. For NiTi-10TiC (S1), the average isotropic

strain in austenite (Eq. 4.1) is plotted against its anisotropic component i.e. ε^{aniso} in Eq. 4.2 during loading in Fig. 4.11a and unloading in Fig. 4.11b. The corresponding figures for NiTi-10TiC (S2) are Fig. 4.12a and Fig. 4.12b and for TiC is Fig. 4.13.

4.5 Discussion

The NiTi-TiC system is known not to have any reaction occurring over a large range of compositions [61, 62]. In addition, [55] confirms this observation with microprobe analysis in the case of martensitic NiTi reinforced with TiC. The unreacted interfaces further suggest that the TiC particles , which were almost perfectly stoichiometric with a composition of 49.8 ± 0.1 at.% C (as determined by combustion analysis with infrared detection), behave as an inert reinforcement. From [9], the temperature at which martensite should start to form (M_s) when austenitic NiTi (51.0 at.% Ni) is cooled is expected to be around -50°C. However, we report a nominal composition of 51.0 at.% and expect some oxygen (that was present in the surface of the original powder prior to hot isostatic pressing) to exist as Ti_4Ni_2O (see Fig. 4.3) and to further deplete the Ti content and consequently depress the Ms temperature. This may be a possible explanation as to why the transformation could not be thermally induced. More work needs to be carried out to confirm this hypothesis. It is important to restate that given the comparable densities (the small differences are attributed to porosity in TiC), grain sizes and the inert nature of the TiC, we believe the mechanical behavior of NiTi-0TiC, NiTi-10TiC and NiTi-20TiC are directly comparable in this work.

4.5.1 Macroscopic mechanical response of NiTi-0TiC, NiTi-10TiC and NiTi-20TiC

From Fig. 4.1 and Table 4.1 it is evident that there are significant differences in the macroscopic mechanical responses of NiTi-0TiC, NiTi-10TiC and NiTi-20TiC.

Starting from stiffness tensor values for austenitic NiTi reported by [53] and [63], the elastic behavior of a polycrystal as a single crystal average is determined using the Hashin-Shtrikman [64] upper and lower bounds for elastic moduli of cubic polycrystals. The Voigt [65] and Reuss average [66] suggested by Hill [67] is also used. The calculations involved in these averaging schemes are shown in Appendix A and the results in Table 4.2.

Using Eshelby's equivalent inclusion method outlined in [68] and [31], an average elastic modulus for the composite stiffness tensor C_C is obtained from

$$C_C = \left\langle C_M^{-1} - f\{(C_I - C_M)[S - f(S-I) + C_M\}^{-1}(C_I - C_M)C_M^{-1} \right\rangle^{-1} \quad \text{.....4.5}$$

where C_M is the stiffness tensor of the matrix, C_I is the stiffness tensor of the inclusion, f is the volume fraction of inclusions, I is the identity matrix and S is the Eshelby tensor. The equiaxed inclusions are assumed to be spherical for purposes of an initial analysis. These calculations are documented in Appendix B and the results compared to those from extensometer measurements in Table 4.3. In predicting an average modulus for the composite, coefficient of thermal expansion mismatch stresses between austenitic NiTi and TiC are neglected as justified below.

The matrix mean internal stress $<\sigma>_M$ is determined using the Eshelby method for non-dilute systems [68] as a result of thermal mismatch stresses upon cooling from the annealing temperature:

$$<\sigma>_M = -fC_M(S-I)\varepsilon_{TM}^T \quad \text{.....4.6}$$

where f is the volume fraction of inclusions, S is the Eshelby tensor, I is the identity matrix, C_M is the matrix stiffness tensor and ε_{TM}^T is the equivalent transformation strain, resulting from the thermal mismatch strain ε^* between matrix and inclusion:

$$\varepsilon_{TM}^T = -\{(C_M - C_I)[S - f(S-I)] - C_M\}^{-1} C_I \varepsilon^* \quad \text{.....4.7}$$

For austenite, an elastic modulus of 74.5 GPa, a shear modulus of 26.8 GPa and a Poisson's ration of 0.39 are used as obtained in Table 4.2. For TiC, the room-temperature elastic constants measured in [69] i.e., c_{11} = 515 GPa, c_{12} = 106 GPa and c_{44} = 179 GPa are used. The thermal mismatch strain resulting from cooling to room temperature (25°C) is

$$\varepsilon^* = (\alpha_I - \alpha_M)(T^* - T_R)[1\,1\,1\,0\,0\,0] \quad \text{.....4.8}$$

where $\alpha_M = 11 \cdot 10^{-6}$ K^{-1} is the average coefficient of thermal expansion for austenite and $\alpha_I = 7.3 \cdot 10^{-6}$ K^{-1} is the average coefficient of thermal expansion of TiC [12, 70]. The term T^* is the temperature at which the mismatch between the two phases is zero, corresponding to the annealing temperature if no relaxation takes place during cooling from the annealing temperature. It is assumed, as observed experimentally [71] [72], that diffusion and creep processes relax the thermal mismatch stresses at temperatures above 0.65 T_M where T_M is the melting point and this value is taken to be 756°C for austenitic NiTi. As shown in Appendix C the matrix tensile stress is determined me to be 24.9 MPa in NiTi-10TiC and 49.1 MPa in NiTi-20TiC from the above method.

Thus there is a significant discrepancy between the moduli obtained from extensometer measurements in Table 4.3 for austenitic NiTi-0TiC, NiTi-10TiC and NiTi-20TiC and the Eshelby predictions. The Rietveld refinements indicate no texture in austenite at these low stresses which may possibly explain the differences in moduli. The predictions account for purely elastic contributions to the modulus while the extensometer may measure non-elastic contributions such as the stress-induced transformation. Assuming that favorable orientations of austenite transform to martensite at these low stresses (e.g., producing a compressive strain of 5.2% in the <011> direction with reference to the parent phase vector basis [73]), a mere 1 vol.% of martensite is needed every 78 MPa to explain the difference in Young's moduli for NiTi-0TiC in Table 4.3. These small volume fractions are below the experimental sensitivity limit. Despite additional elastic phase mismatch in the composites, even smaller volume fractions of martensite are needed to account for the moduli differences in the composites. This suggests that the stress-induced martensite matrix accommodates very effectively these mismatch strains.

From Table 4.1 and Fig. 4.1 the following observations are made:

(a) The stress at which austenite transforms to martensite and transforms back to austenite increases with increasing TiC content.

(b) The stress-strain gradient during the transformation is steeper with increasing TiC content.

(c) The total recoverable macroscopic strain decreases with increasing TiC content.

A thermoelastic martensitic transformation is based on a balance of chemical free-energy, elastic strain energy and the interfacial energy during the course of the forward and reverse transformations. The transformational shape-change is accommodated elastically in the system and the build up of this strain-energy hinders further growth. The hysteresis observed in the idealized curve in Fig. 2.1 is due to the friction stress for interface motion as austenite transforms to martensite [74]. From [75], it is known that in the case of multiple-interface transformations as compared to single-interface transformations, the resulting constraints to the transformational shape-change cause elastic strain energy to be stored and hence the gradient of the stress-strain curve during the transformation will be steeper. Thus thermodynamically, the additional elastic strain energy introduced by the interaction of the martensite with the TiC particles results in the stress-strain gradient being steeper with increasing volume fraction of TiC. This also suggests that higher stresses will be needed to transform austenite to martensite with increasing TiC. In addition, load partitioning due to TiC can be expected to be responsible for

these changes in stress levels and stress-strain gradients. These two effects have not been decoupled in this work.

The decreasing recoverable strain with increasing TiC could arise because of lower transformation strains associated with martensite forming in the presence of TiC or due to lower volume fraction of martensite forming in the presence of TiC.

4.5.2 Phase fraction evolution

Fig. 4.5 addresses the issue of martensite phase fraction evolution in NiTi-0TiC and NiTi-10TiC. A linear relationship is observed during loading-unloading between the volume fraction of martensite formed and the superelastic strain. There is no hysteresis observed during loading and unloading suggesting that the hysteresis observed is with respect to stress and not strain [74].

The question that may be raised is whether the martensite that is formed can twin further to generate more strain. This is possible if the martensite is not in the optimal orientation and growth/coalescence of certain martensite variants (equivalent to a twinning operation) can produce more strains. To answer this question NiTi-0TiC, NiTi-10TiC and NiTi-20TiC were progressively tested to higher stresses. The martensite begins to yield due to slip and strains are no longer recoverable on unloading. There was no evidence of significant twinning. This is shown in Fig. 4.14 (see non-recoverable strains around 0 MPa), where the plastic strain from the previous cycle is subtracted out.

The strain introduced by austenite transforming to martensite can be thought of as being a product of the transformation strain and the volume fraction. Thus if more favorably oriented martensite forms (i.e. the strains associated with the transformation are larger) or simply more of it forms, the recoverable strains can be expected to be larger. Fig. 4.5 shows that a larger volume fraction of martensite is needed to generate the same superelastic strain when TiC particles are present. This seems to suggest that the transformation strains associated with the formation of martensite are smaller in the case when TiC particles are present. This is understandable given that a favorable variant may not be compatible with a non-transforming TiC particle in its proximity.

4.5.3 Texture evolution

Due to the nature of the transformation, the martensite that forms is highly textured. This is seen in the high texture indices of the martensite in Fig. 4.7. Clearly the martensite that

exists at lower strains is more textured that the martensite that exists at higher strains. Given the linear relationship in Fig. 4.5 and the decreasing texture in Fig. 4.7, it appears that there should be a non-unique association between orientation of variants and transformation strain. This means one or more orientations among the 24 variants should generate the same strain because the martensite that forms earlier generates the same strain as martensite that forms at higher stresses. From Fig. 4.7 it is not clear whether the martensite in the presence of TiC is more textured than martensite in the presence of only austenite. These issues are dealt in a more quantitative manner in the next chapter.

4.5.4 Austenite strains in NiTi-0TiC

The average modulus of austenite from neutron diffraction is determined to be 74.5 GPa in Fig. 4.8a and 66.9 GPa in Fig. 4.8b (statistics in Fig. 4.8b are poorer since fewer data points are available) . This compares well with the values obtained from the various averaging methods. However, the modulus of the austenite phase measured by this method would be expected to change at higher load levels due to (i) load transfer to the stress-induced martensite which exhibits different elastic constants, (ii) transformation mismatch stresses between the two phases, and (iii) the evolving texture in the austenite. The latter effect results from the strong texture qualitatively observed in individual spectra of the stress-induced martensite and the resulting austenite texture, given the unique lattice correspondence that exists between the austenite and the martensite phases. However, Fig. 4.8 shows that these three effects do not cause any significant non-linearity in the stress-strain response of austenite in either loading or unloading, despite the fact that more martensite exists during unloading than loading for the same stress level due to the hysteresis shown in Fig. 4.1. This suggests that the non-linear effects either cancel each other or have negligible magnitude.

.

4.5.5 Austenite and TiC strains in NiTi-10TiC and NiTi-20TiC

Eshelby's equivalent inclusion method is also used to predict the strains in austenite and TiC phases. Using the same notation and source as before, the equivalent transformation strain due to elastic mismatch is given by:

$$\varepsilon_{EM}^{T} = \left\langle -\{(C_M - C_I)[S - f(S-I)] - C_M\}^{-1} \right\rangle \left\langle (C_M - C_I)(C_M^{-1}\sigma_A) \right\rangle \qquad \text{.....4.9}$$

where σ_A is the applied external stress. The total equivalent transformation strain is a sum of the equivalent transformation strain resulting from thermal mismatch (Eq. 4.7) and elastic mismatch (Eq. 4.9) i.e.

$$\varepsilon^T_{TOT} = \varepsilon^T_{TM} + \varepsilon^T_{EM} \qquad .....4.10$$

The matrix mean internal stress is now given by

$$<\sigma>_M = -fC_M(S-I)\varepsilon^T_{TOT} \qquad .....4.11$$

and the inclusion mean internal stress by

$$<\sigma>_I = -(1-f)C_M(S-I)\varepsilon^T_{TOT} \qquad .....4.12$$

The average strains in the matrix and inclusion are

$$\bar{\varepsilon}_M = C_M^{-1}\bar{\sigma}_M$$

$$\bar{\varepsilon}_I = C_I^{-1}\bar{\sigma}_I \qquad .....4.13$$

where the average stresses are

$$\bar{\sigma}_M = \sigma_A + <\sigma>_M$$

$$\bar{\sigma}_I = \sigma_A + <\sigma>_I \qquad .....4.14$$

Fig. 4.9 shows the individual phase strains in austenite and TiC as obtained by Rietveld refinement (Eq. 4.1) and predicted from Eshelby theory using the above equations for NiTi-20TiC. Fig. 4.10a and Fig. 4.10b are the corresponding figures for NiTi-10TiC (S1) and NiTi-10TiC (S2). A sample calculation is documented in Appendix D. Values obtained from the single-crystal averaging methods for austenite were used for the matrix in the predictions, in the light of its behavior in Fig. 4.8, while elastic constants from [69] were used for TiC. The strains obtained from the diffraction data are referenced to the residual stresses in Appendix C in the no load condition. The figures show reasonable agreement between elastic theory and experimental data.

Agreement in Fig. 4.9 is expected for NiTi-20TiC because little martensite is formed, so that the composite deforms mostly elastically. On the other hand, NiTi-10TiC shows significant amounts of stress-induced martensite at high applied stresses (Fig. 4.1) which could lead to additional mismatch with the TiC particles and thus deviation from the elastic response in Fig. 4.10, as observed in plastically deforming aluminum composites [34]. The lack of such plastic

load-transfer suggests that the austenite/martensite matrix effectively accommodates the mismatch arising between the elastic TiC and the superelastic matrix deforming by stress-induced transformation, as also shown above for the case without TiC. This may be attributed to the self-accommodating nature of the transformation, wherein certain variants can preferentially form to minimize mismatch between matrix and reinforcement, as also observed in shape-memory NiTi-TiC composites deforming by martensite twinning [59].

4.5.6 Anisotropic components of strain

The above described strains indicate an average isotropic strain as described in Eq. 4.1. This strain was found to be representative of the average behavior of the various individual reflections in Chapter 3. However, the Rietveld refinement procedure was also modified to incorporate anisotropic components of the strain as described earlier. As seen earlier for austenite in NiTi-0TiC in Chapter 3, changes in the anisotropic component of the strain are also observed in the austenite phase of NiTi-10TiC in Fig. 4.11 and Fig. 4.12. This may be attributed to the additional anisotropy introduced by the transformation. The strain levels at which the changes in anisotropy occur are indicated in Fig. 4.11 (due to poor statistics Fig. 4.12 only shows trends) and a hysteresis is again noted. The corresponding stress levels are 370 MPa and 290 MPa and can be compared to experimentally observed values in Table 4.1. The differences, if real, can be attributed to some initial anisotropy contribution from the transformation canceling the elastic contribution since they appear to act in opposite directions in Chapter 3.

For TiC no significant changes are observed in Fig. 4.13 and the anisotropic component is very small given the large stiffness of TiC and consequently small elastic strains.

4.6 Conclusions

The above discussion of strains has been limited to austenite and TiC phases. The low symmetry of the martensite and consequently the large number of reflections make it very difficult for a Rietveld refinement to converge while strains are physically described in the martensite phase. As described in Chapter 3, for martensite the emphasis was on accurately modeling the volume fraction and the texture. Given the macroscopic stress-strain behavior and the discrete phase strains in austenite and TiC, no additional information is important to describe

the strain information. The issue of using strains in the martensite along with the texture information is discussed in Chapter 9.

In this chapter, Rietveld refinements of neutron diffraction spectra have been used to elucidate stress-induced transformations in superelastic NiTi containing 0, 10 and 20 vol.% TiC particles. The following conclusions are made and explained:

(1) The volume fraction of martensite formed at any given applied stress and the recoverable strain decreases with increasing TiC content.

(2) The stress at which austenite transforms to martensite and transforms back to austenite increases with increasing TiC content.

(3) Significant discrepancies are observed in the elastic moduli of NiTi-10TiC and NiTi-20TiC measured between measurements by extensometry and predictions by Eshelby's theory. The differences are attributed to small amounts of austenite transforming to martensite at low stresses which reduces the apparent modulus.

(4) The generalized spherical harmonics texture formulation provides a determination of austenite and martensite phase fractions evolving in the matrix. A linear relationship is observed between the volume of martensite formed and the strain generated by the transformation. The relationship is maintained during loading and unloading suggesting that the hysteresis is due to stress and not strain.

(5) The overall texture of the martensite as it forms decreases with increasing stress. This is due to more favorable orientations of austenite transforming first to martensite. To maintain the linearity in the volume fraction-superelastic strain curve, a non-unique relationship between the transformation strain and variant orientation is expected.

(6) The elastic moduli of austenite in NiTi-0TiC measured by neutron diffraction compared very well with moduli predicted from various polycrystalline averaging schemes (Hashin-Shtrikman bounds and Hill average) using single crystal data.

(7) Load transfer or texture in the evolving austenite does not cause any significant non-linearity in the stress-strain response of austenite in the presence of martensite, suggesting that they either cancel each other or have negligible magnitudes.

(8) Additional anisotropy introduced by the transformation is captured in changes in the anisotropic component of the strain of the austenite phase in NiTi-10TiC as seen before for austenite in NiTi-0TiC.

(9) Good agreement is observed between Eshelby's elastic theory and phase strains in the transforming matrix and the elastic TiC reinforcement, suggesting that the self-accommodation of the stress-induced martensite almost minimizes the transformation mismatch with the TiC particles.

4.7 Tables

Sample	Elastic modulus (GPa)	Stress transformation initiates (MPa)	Stress transformation finishes (MPa)
NiTi-0TiC (S1)	50 ± 2	320 ± 15	280 ± 15
NiTi-0TiC (S2)	51 ± 2	220 ± 15	180 ± 15
NiTi-10TiC (S1)	58 ± 2	375 ± 15	255 ± 15
NiTi-10TiC (S2)	59 ± 2	400 ± 15	270 ± 15
NiTi-20TiC (S1)	74 ± 2	non determinate	

Table 4.1 Measured moduli and stresses at which the transformation starts and ends for NiTi-0TiC, NiTi-10TiC and NiTi-20TiC

	For c_{11}=137 GPa, c_{12}=101 GPa, c_{44}=35 GPa [53]			For c_{11}=162 GPa, c_{12}=129 GPa, c_{44}=35 GPa [63]		
Averaging method	**Young's Modulus (GPa)**	**Shear Modulus (GPa)**	**Poisson's ratio**	**Young's Modulus (GPa)**	**Shear Modulus (GPa)**	**Poisson's ratio**
1	74.4	26.8	0.39	72.9	25.8	0.41
2	75.4	27.2	0.39	74.3	26.3	0.41
3	78.1	28.2	0.39	77.4	27.5	0.41
4	70.9	25.4	0.40	68.6	24.2	0.42
5	74.5	26.8	0.39	73.0	25.8	0.41

Table 4.2 Polycrystalline elastic constants from single crystal data for austenite from various averaging methods i.e. 1. Hashin-Shtrikman lower bound 2. Hashin-Shtrikman upper bound [64], 3. Reuss [66], 4. Voigt [65] and 5. Hill [67].

	Extensometer measurement	Theoretical prediction	Method of prediction
NiTi-0TiC	50 ± 2	74.4-75.4 74.5	Hashin-Shtrikman [64] Hill average [67]
NiTi-10TiC	58 ± 2	87.3	Eshelby [68]
NiTi-20TiC	74 ± 2	102.1	Eshelby [68]

Table 4.3 Elastic moduli (GPa) of NiTi-0TiC, NiTi-10TiC and NiTi-20TiC as determined by extensometry and as predicted; discrepancies suggest non-elastic contributions to the extensometer moduli.

4.8 Figures

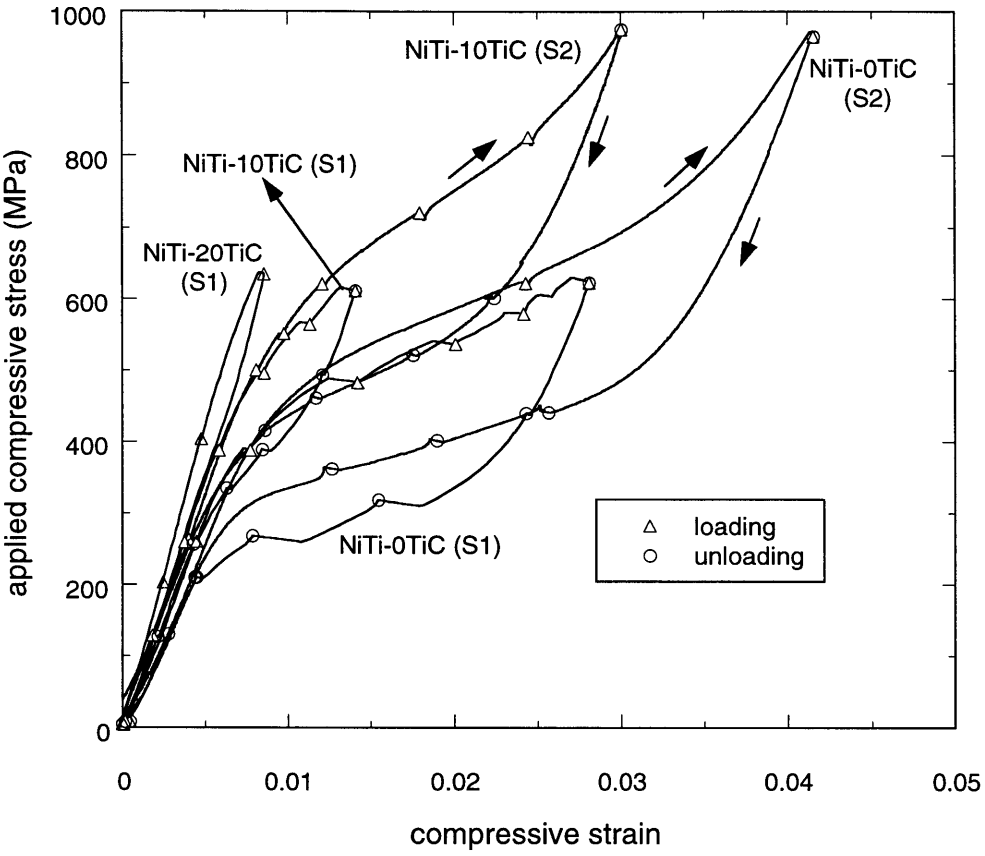

Fig. 4.1 Curves of applied compressive stress vs. compressive strain measured by extensometry for NiTi-0TiC, NiTi-10TiC and NiTi-20TiC. The symbols indicate the stress levels at which neutron diffraction spectra were obtained.

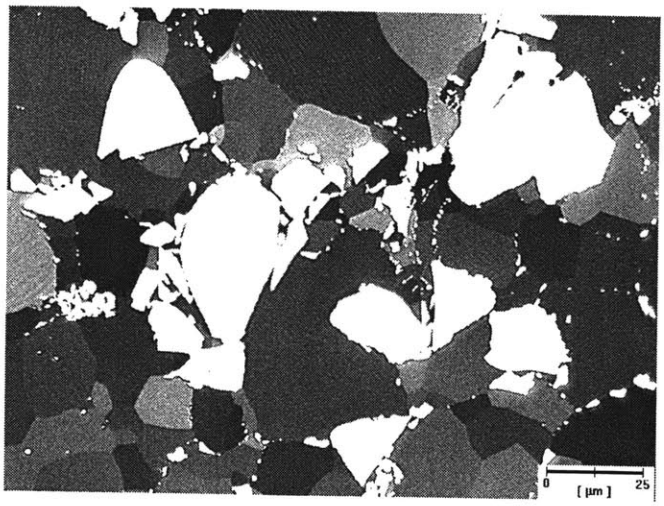

Fig. 4.2 Polarized light micrograph of NiTi-10TiC showing non-reacted interfaces between TiC (in white) and the matrix.

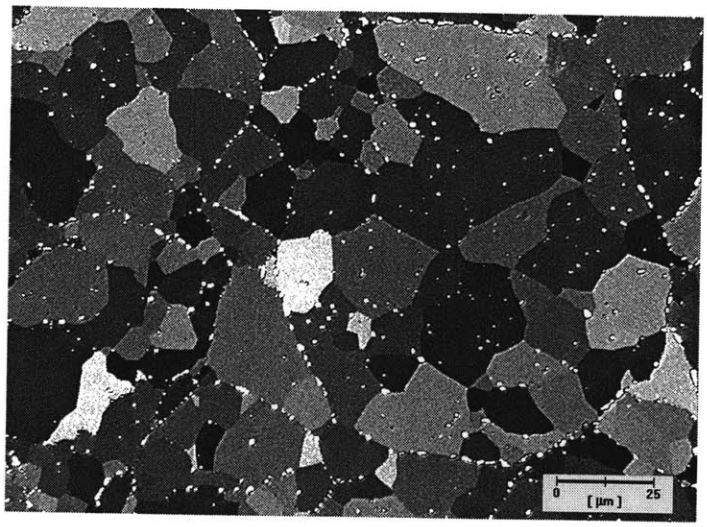

Fig. 4.3 Polarized light micrograph showing oxide precipitates. The outline seen here could be a martensitic NiTi particle prior to HIP.

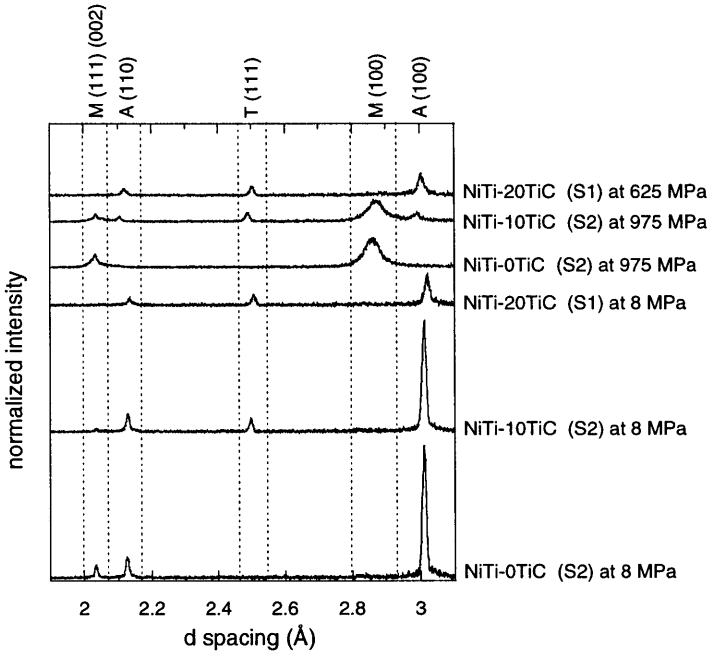

Fig. 4.4 Section of normalized neutron diffraction spectra (scattering vector parallel to loading direction) from NiTi-0TiC, NiTi-10TiC and NiTi-20TiC under stress and at 8 MPa with austenite (A), martensite (M) and TiC (T) peaks identified. A nominal stress of 8 MPa was used as the "no load" condition to hold the specimen horizontally in the rig. Diffraction from steel in the extensometer knife edges contaminates the M(111) reflection especially for NiTi-0TiC (S2) at 8 MPa. This was determined to have no effect on the refinement.

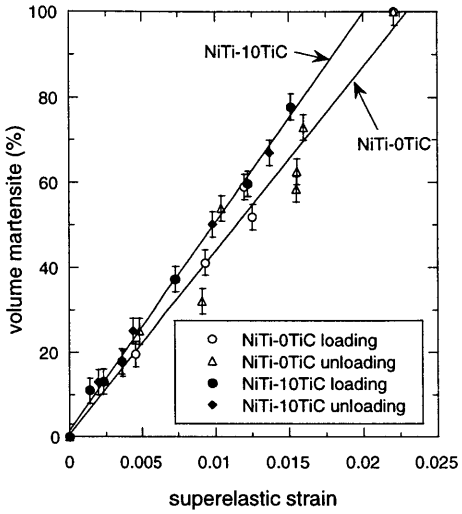

Fig. 4.5 Volume (%) of martensite obtained from Rietveld refinements as a function of the superelastic strain in four samples of NiTi-0TiC and NiTi-10TiC.

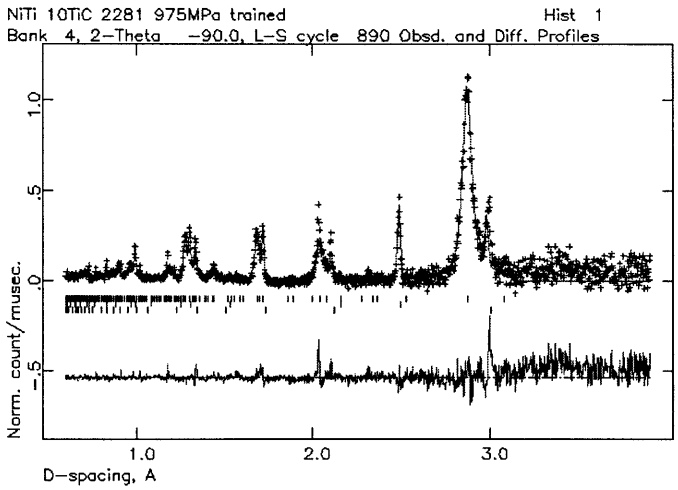

Fig. 4.6 A typical GSAS Rietveld refinement output (shown here for NiTi-10TiC (S2) at 975 MPa) for diffracting lattice planes perpendicular to the load. The crosses are the measured spectra; the line through them is the Rietveld least squares fit. The tick marks indicate reflections from the martensite, austenite and TiC phases. The difference curve between refinement and measurement is also shown.

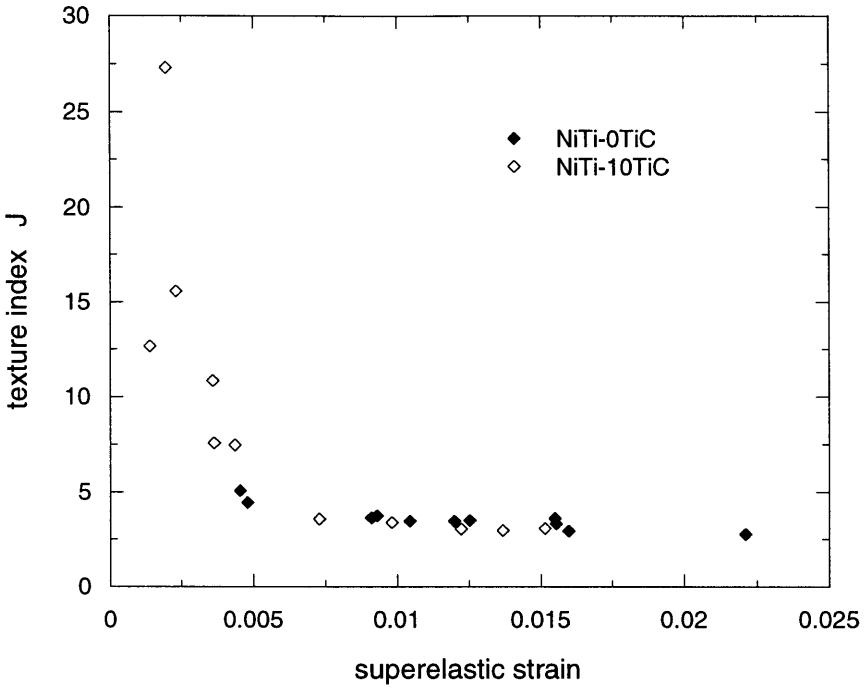

Fig. 4.7 Texture index J for NiTi-0TiC (S1), NiTi-0TiC (S2), NiTi-10TiC (S1), NiTi-10TiC (S2), for martensite as a function of the superelastic strain.

(a)

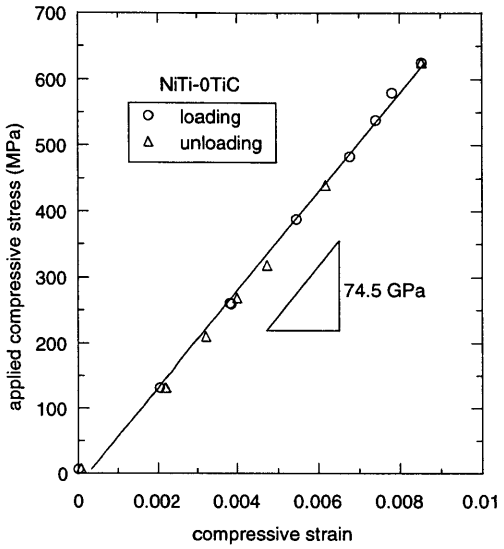

(b)

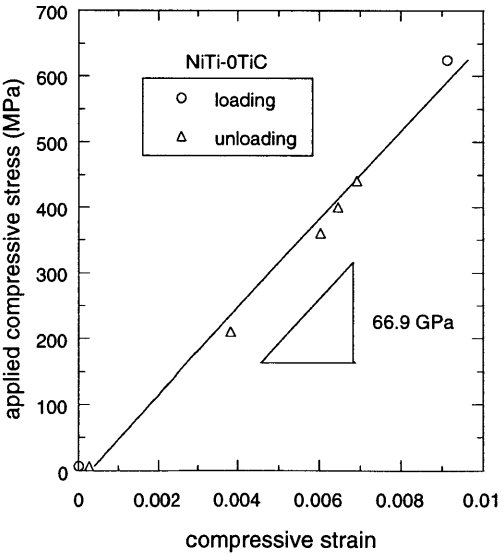

Fig. 4.8 The strain obtained from Rietveld analysis (Eq. 4.1) in the austenite phase in (a) NiTi-0TiC (S1) and (b) NiTi-0TiC (S2) during loading and unloading.

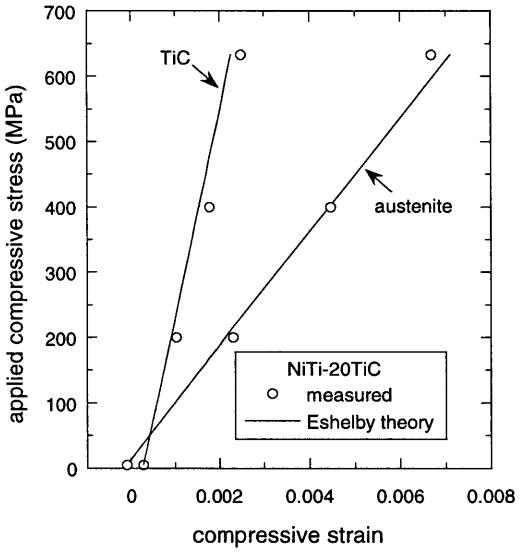

Fig. 4.9 The strains obtained from the Rietveld analysis (Eq. 4.1) in the austenite and TiC phases in NiTi-20TiC (S1). Discrete phase strains predicted by Eshelby's elastic theory are also shown.

(a)

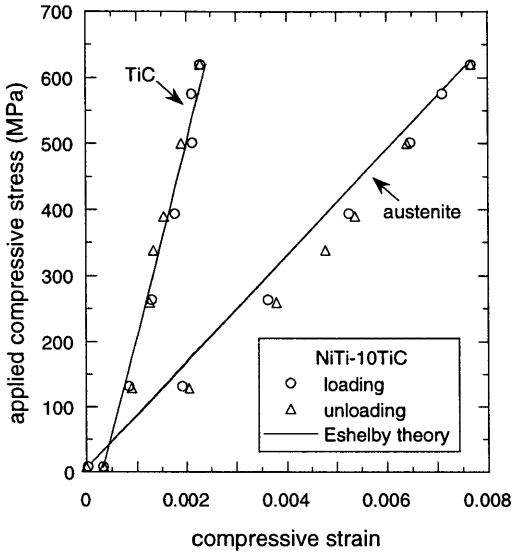

(b)

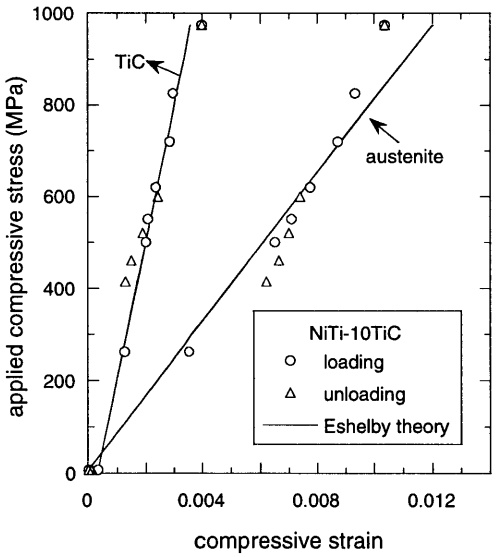

Fig. 4.10 The strains obtained from Rietveld analysis (Eq. 4.1) in the austenite and TiC phases in (a) NiTi-10TiC (S1) and (b) NiTi-10TiC (S2) during loading and unloading Discrete phase strains predicted by Eshelby's elastic theory are also shown.

(a)

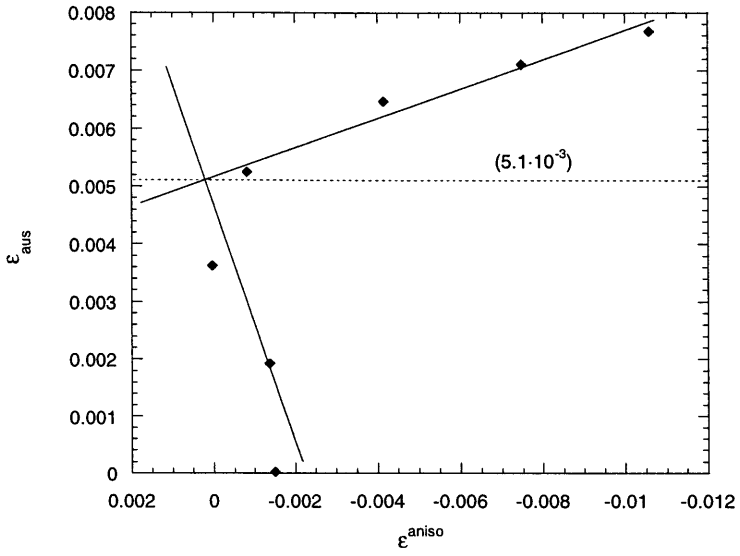

(b)

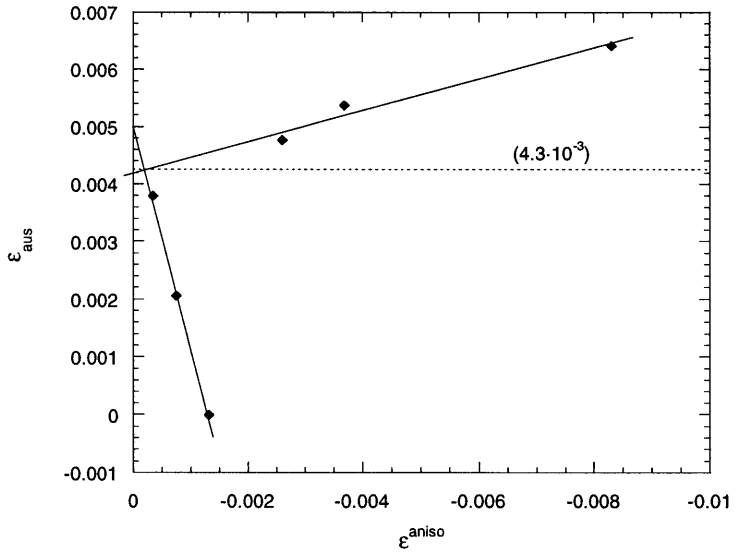

Fig. 4.11 The isotropic strain in austenite (ε_{aus} in Eq. 4.1) plotted against its anisotropic component (ε^{aniso} in Eq. 4.2) during loading in (a) and unloading in (b) in NiTi-10TiC (S1).

(a)

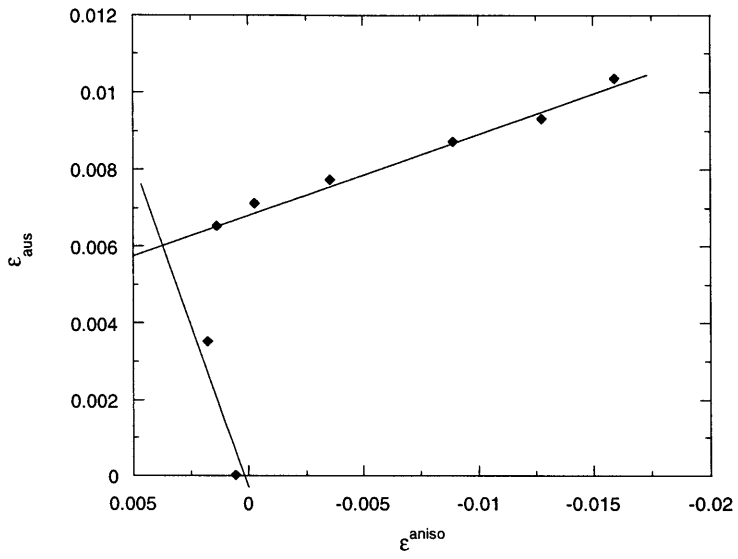

(b)

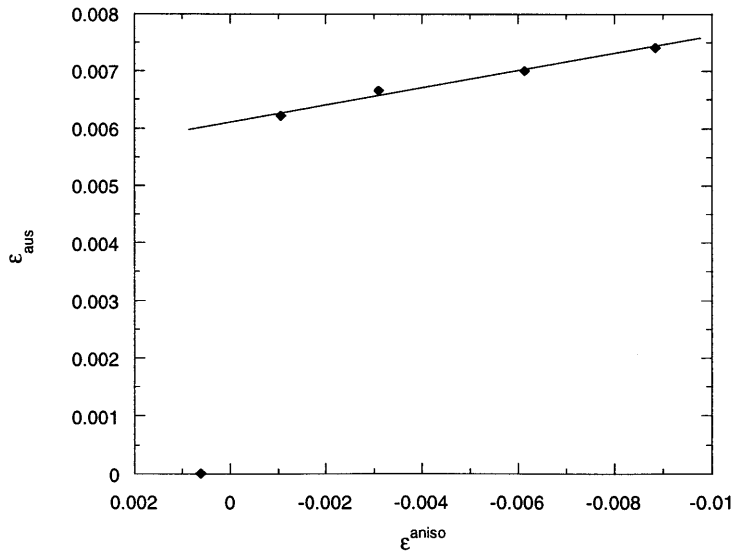

Fig. 4.12 The isotropic strain in austenite (ε_{aus} in Eq. 4.1) plotted against its anisotropic component (ε^{aniso} in Eq. 4.2) during loading in (a) and unloading in (b) in NiTi-10TiC (S2).

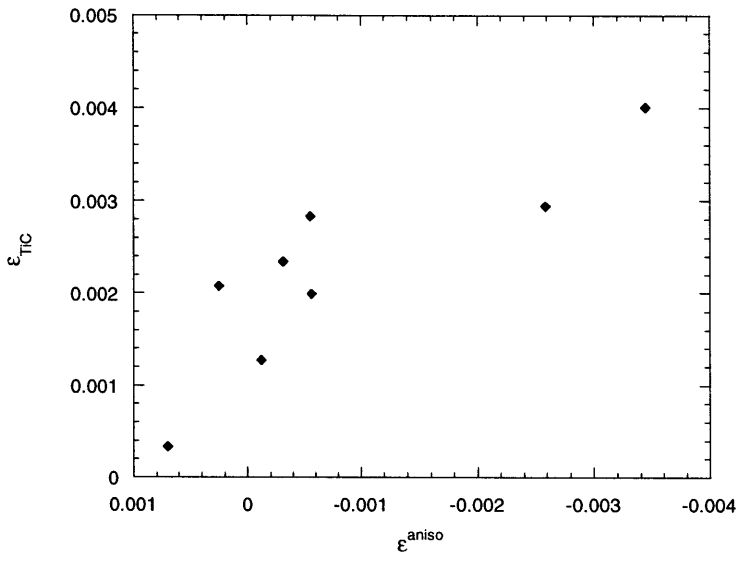

Fig. 4.13 The isotropic strain in TiC (ε_{TiC} in Eq. 4.1) plotted against its anisotropic component (ε^{aniso} in Eq. 4.2) during loading in NiTi-10TiC (S2)

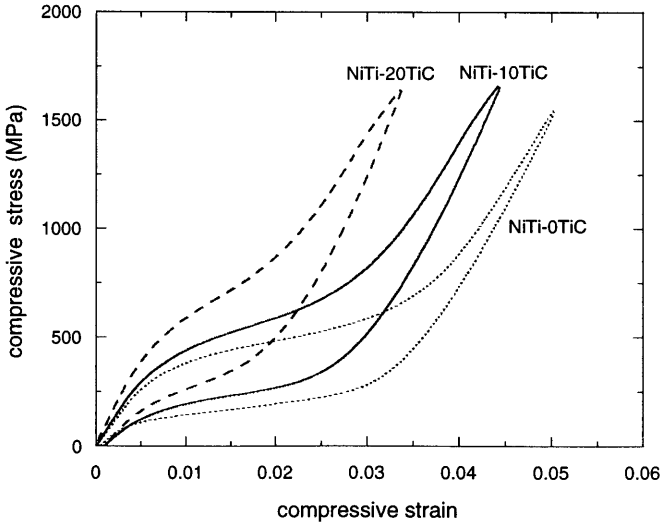

Fig. 4.14 Stress-strain response of NiTi-0TiC, NiTi-10TiC and NiTi-20TiC tested to higher compressive stresses to investigate whether the martensite formed further twins to yield larger strains. Note that the plastic strain from the previous cycle is subtracted out.

4.9 Appendix A

Mathcad 7.0 document for averaging schemes to obtain polycrystalline elastic constants from single crystal data

$c_{11} := 137$ $c_{12} := 101$ $c_{44} := 35$ Components of the stiffness tensor in GPa from Brill et al

$K := \frac{1}{3}(c_{11} + 2c_{12})$ $K = 113$ Bulk modulus K in GPa

$G_1 := \frac{1}{2}(c_{11} - c_{12})$ $G_1 = 18$

$G_2 := c_{44}$ $G_2 = 35$ Shear moduli in GPa

$\beta_1 := \frac{-3\cdot(K + 2G_1)}{5G_1\cdot(3K + 4G_1)}$ $\beta_2 := \frac{-3\cdot(K + 2G_2)}{5G_2\cdot(3K + 4G_2)}$ parameter definition

H subscript denotes lower bound of Hashin-Shtrikman
S subscript denotes upper bound of Hashin-Shtrikman
V subscript denotes Voigt average
R subscript denotes Reuss average
RV subscript denotes mean of Reuss and Voigt (Hill average)
all E and G are in GPa

$G_H := G_1 + 3\left(\frac{5}{G_2 - G_1} - 4\beta_1\right)^{-1}$ $G_S := G_2 + 2\left(\frac{5}{G_1 - G_2} - 6\beta_2\right)^{-1}$

$G_R := \frac{5G_1\cdot G_2}{2G_2 + 3G_1}$ $G_V := \frac{1}{5}(2\cdot G_1 + 3\cdot G_2)$ $G_{RV} := \frac{1}{2}(G_R + G_V)$

$\nu_H := \frac{1}{2}\left(1 - \frac{3\cdot G_H}{3\cdot K + G_H}\right)$ $\nu_S := \frac{1}{2}\left(1 - \frac{3\cdot G_S}{3\cdot K + G_S}\right)$ $\nu_{RV} := \frac{1}{2}\left(1 - \frac{3\cdot G_{RV}}{3\cdot K + G_{RV}}\right)$

$\nu_R := \frac{1}{2}\left(1 - \frac{3\cdot G_R}{3\cdot K + G_R}\right)$ $\nu_V := \frac{1}{2}\left(1 - \frac{3\cdot G_V}{3\cdot K + G_V}\right)$

$E_H := \left(\frac{1}{3G_H} + \frac{1}{9K}\right)^{-1}$ $E_S := \left(\frac{1}{3G_S} + \frac{1}{9K}\right)^{-1}$ $E_{RV} := \left(\frac{1}{3G_{RV}} + \frac{1}{9K}\right)^{-1}$

$$E_R := \left(\frac{1}{3\,G_R} + \frac{1}{9\,K}\right)^{-1} \qquad E_V := \left(\frac{1}{3\,G_V} + \frac{1}{9\,K}\right)^{-1}$$

$G_H = 26.76$	$E_H = 74.407$	$\nu_H = 0.39$
$G_S = 27.151$	$E_S = 75.414$	$\nu_S = 0.389$
$G_V = 28.2$	$E_V = 78.103$	$\nu_V = 0.385$
$G_R = 25.403$	$E_R = 70.897$	$\nu_R = 0.395$
$G_{RV} = 26.802$	$E_{RV} = 74.514$	$\nu_{RV} = 0.39$

Using values from Mercier et al (c_{11}= 162.44 GPa, c_{12}=129.24 GPa and c_{44}=34.77 GPa) gives,

$G_H = 25.771$	$E_H = 72.852$	$\nu_H = 0.413$
$G_S = 26.298$	$E_S = 74.255$	$\nu_S = 0.412$
$G_V = 27.494$	$E_V = 77.424$	$\nu_V = 0.408$
$G_R = 24.165$	$E_R = 68.559$	$\nu_R = 0.419$
$G_{RV} = 25.83$	$E_{RV} = 73.008$	$\nu_{RV} = 0.413$

4.10 Appendix B

Mathcad 7.0 document estimating composite stiffness using Eshelby theory

$E_M := 74.514$

$\nu_M := 0.39$

$G_M := 26.8$

properties of austenite as determined from various bounds (E_m and G_m are in GPa)

$F := 0.2$ Volume fraction of inclusions

$$C_I := \begin{bmatrix} 515 & 106 & 106 & 0 & 0 & 0 \\ 106 & 515 & 106 & 0 & 0 & 0 \\ 106 & 106 & 515 & 0 & 0 & 0 \\ 0 & 0 & 0 & 179 & 0 & 0 \\ 0 & 0 & 0 & 0 & 179 & 0 \\ 0 & 0 & 0 & 0 & 0 & 179 \end{bmatrix}$$

Stiffness tensor for inclusion (GPa)

$$S_{11} := \frac{1}{E_M} \qquad S_{12} := \frac{-\nu_M}{E_M} \qquad S_{44} := 2\left(S_{11} - S_{12}\right)$$

$$C_{11} := \frac{S_{11} + S_{12}}{\left(S_{11} - S_{12}\right)\left(S_{11} + 2S_{12}\right)} \qquad C_{44} := \frac{1}{S_{44}}$$

$$C_{12} := \frac{-S_{12}}{\left(S_{11} - S_{12}\right)\cdot\left(S_{11} + 2S_{12}\right)}$$

$C_{11} = 148.638$

$C_{12} = 95.031$

$C_{44} = 26.804$

Eshelby S tensor for spherical inclusions

$$S := \begin{bmatrix} \frac{7-5\nu_M}{15(1-\nu_M)} & \frac{-1+5\nu_M}{15(1-\nu_M)} & \frac{-1+5\nu_M}{15(1-\nu_M)} & 0 & 0 & 0 \\ \frac{-1+5\nu_M}{15(1-\nu_M)} & \frac{7-5\nu_M}{15(1-\nu_M)} & \frac{-1+5\nu_M}{15(1-\nu_M)} & 0 & 0 & 0 \\ \frac{-1+5\nu_M}{15(1-\nu_M)} & \frac{-1+5\nu_M}{15(1-\nu_M)} & \frac{7-5\nu_M}{15(1-\nu_M)} & 0 & 0 & 0 \\ 0 & 0 & 0 & \frac{8-10\nu_M}{15(1-\nu_M)} & 0 & 0 \\ 0 & 0 & 0 & 0 & \frac{8-10\nu_M}{15(1-\nu_M)} & 0 \\ 0 & 0 & 0 & 0 & 0 & \frac{8-10\nu_M}{15(1-\nu_M)} \end{bmatrix}$$

$$C_M := \begin{bmatrix} C_{11} & C_{12} & C_{12} & 0 & 0 & 0 \\ C_{12} & C_{11} & C_{12} & 0 & 0 & 0 \\ C_{12} & C_{12} & C_{11} & 0 & 0 & 0 \\ 0 & 0 & 0 & C_{44} & 0 & 0 \\ 0 & 0 & 0 & 0 & C_{44} & 0 \\ 0 & 0 & 0 & 0 & 0 & C_{44} \end{bmatrix}$$

Stiffness tensor for matrix
(elements in GPa)

$$I := \begin{bmatrix} 1 & 0 & 0 & 0 & 0 & 0 \\ 0 & 1 & 0 & 0 & 0 & 0 \\ 0 & 0 & 1 & 0 & 0 & 0 \\ 0 & 0 & 0 & 1 & 0 & 0 \\ 0 & 0 & 0 & 0 & 1 & 0 \\ 0 & 0 & 0 & 0 & 0 & 1 \end{bmatrix}$$

$$C_C := \left[C_M^{-1} - F \cdot \left[\left(C_I - C_M \right) \cdot (S - F \cdot (S - I)) + C_M \right]^{-1} \cdot \left(C_I - C_M \right) C_M^{-1} \right]^{-1}$$

$$C_C = \begin{bmatrix} 177.93 & 103.272 & 103.272 & 0 & 0 & 0 \\ 103.272 & 177.93 & 103.272 & 0 & 0 & 0 \\ 103.272 & 103.272 & 177.93 & 0 & 0 & 0 \\ 0 & 0 & 0 & 36.831 & 0 & 0 \\ 0 & 0 & 0 & 0 & 36.831 & 0 \\ 0 & 0 & 0 & 0 & 0 & 36.831 \end{bmatrix}$$

$$C_{11} := C_{C_{0,0}}$$

$$C_{12} := C_{C_{1,0}}$$

$$C_{44} := C_{C_{4,4}}$$

$$S_{11} := \frac{C_{11} + C_{12}}{\left(C_{11} - C_{12} \right) \left(C_{11} + 2\, C_{12} \right)} \qquad S_{44} := \frac{1}{C_{44}}$$

$$S_{12} := \frac{-C_{12}}{\left(C_{11} - C_{12} \right) \cdot \left(C_{11} + 2\, C_{12} \right)} \qquad E := \frac{1}{S_{11}}$$

$$\nu := -E \cdot S_{12} \qquad G := \frac{E}{2\,(1 + \nu)}$$

$$S_{11} = 9.797 \cdot 10^{-3} \qquad S_{12} = -3.598 \cdot 10^{-3} \qquad S_{44} = 0.027$$

$$E = 102.076 \qquad \nu = 0.367 \qquad G = 37.329$$

for F=0.1,

$$\nu := -E \cdot S_{12} \qquad G := \frac{E}{2(1+\nu)}$$

$S_{11} = 0.011$ $S_{12} = -4.343 \cdot 10^{-3}$ $S_{44} = 0.032$

$E = 87.263$ $\nu = 0.379$ $G = 31.641$

4.11 Appendix C

Mathcad 7.0 document to determine thermal mismatch stresses between matrix and reinforcement

$E_m := 74.514$

$\nu_m := 0.39$

$G_m := 26.8$

properties of austenite as determined from various bounds (E_m and G_m are in GPa)

$\alpha_m := 11 \cdot 10^{-6}$ average coefficient of thermal expansion for matrix in K^{-1}

$f := 0.1$ volume fraction of inclusions

$\alpha_i := 7.3 \cdot 10^{-6}$ average coefficient of thermal expansion for inclusion in K^{-1}

$T_f := 756$ lowest temperature at which mismatch is zero in °C

$T_r := 25$ room temperature °C

$$C_i := \begin{bmatrix} 515 & 106 & 106 & 0 & 0 & 0 \\ 106 & 515 & 106 & 0 & 0 & 0 \\ 106 & 106 & 515 & 0 & 0 & 0 \\ 0 & 0 & 0 & 179 & 0 & 0 \\ 0 & 0 & 0 & 0 & 179 & 0 \\ 0 & 0 & 0 & 0 & 0 & 179 \end{bmatrix}$$

Stiffness tensor for inclusion (GPa)

$$s_{11} := \frac{1}{E_m} \qquad s_{12} := \frac{-\nu_m}{E_m} \qquad s_{44} := 2\left(s_{11} - s_{12}\right)$$

$$c_{11} := \frac{s_{11} + s_{12}}{\left(s_{11} - s_{12}\right)\left(s_{11} + 2 s_{12}\right)} \qquad c_{44} := \frac{1}{s_{44}}$$

$$c_{12} := \frac{-s_{12}}{\left(s_{11} - s_{12}\right) \cdot \left(s_{11} + 2 s_{12}\right)}$$

$c_{11} = 148.638$

$c_{12} = 95.031$

$c_{44} = 26.804$

Eshelby S tensor for spherical inclusions

$$S := \begin{bmatrix} \frac{7-5\nu_m}{15(1-\nu_m)} & \frac{-1+5\nu_m}{15(1-\nu_m)} & \frac{-1+5\nu_m}{15(1-\nu_m)} & 0 & 0 & 0 \\ \frac{-1+5\nu_m}{15(1-\nu_m)} & \frac{7-5\nu_m}{15(1-\nu_m)} & \frac{-1+5\nu_m}{15(1-\nu_m)} & 0 & 0 & 0 \\ \frac{-1+5\nu_m}{15(1-\nu_m)} & \frac{-1+5\nu_m}{15(1-\nu_m)} & \frac{7-5\nu_m}{15(1-\nu_m)} & 0 & 0 & 0 \\ 0 & 0 & 0 & \frac{8-10\nu_m}{15(1-\nu_m)} & 0 & 0 \\ 0 & 0 & 0 & 0 & \frac{8-10\nu_m}{15(1-\nu_m)} & 0 \\ 0 & 0 & 0 & 0 & 0 & \frac{8-10\nu_m}{15(1-\nu_m)} \end{bmatrix}$$

$$C_m := \begin{bmatrix} c_{11} & c_{12} & c_{12} & 0 & 0 & 0 \\ c_{12} & c_{11} & c_{12} & 0 & 0 & 0 \\ c_{12} & c_{12} & c_{11} & 0 & 0 & 0 \\ 0 & 0 & 0 & c_{44} & 0 & 0 \\ 0 & 0 & 0 & 0 & c_{44} & 0 \\ 0 & 0 & 0 & 0 & 0 & c_{44} \end{bmatrix}$$

Stiffness tensor for matrix

$$I := \begin{bmatrix} 1 & 0 & 0 & 0 & 0 & 0 \\ 0 & 1 & 0 & 0 & 0 & 0 \\ 0 & 0 & 1 & 0 & 0 & 0 \\ 0 & 0 & 0 & 1 & 0 & 0 \\ 0 & 0 & 0 & 0 & 1 & 0 \\ 0 & 0 & 0 & 0 & 0 & 1 \end{bmatrix}$$

$$\varepsilon_{tm} := \left(\alpha_m - \alpha_i\right)\left(T_f - T_r\right) \cdot \begin{bmatrix} 1 \\ 1 \\ 1 \\ 0 \\ 0 \\ 0 \end{bmatrix}$$ thermal mismatch strain

$$\varepsilon_t := \left[-\left[\left(C_m - C_i\right) \cdot (S - f \cdot (S - I)) - C_m\right]\right]^{-1} \cdot C_i \cdot \varepsilon_{tm} \cdot 10^9$$ equivalent transformation strair

$$\sigma_m := -f \cdot C_m \cdot (S - I)\, \varepsilon_t$$

$$\frac{\sigma_m}{10^6} = \begin{bmatrix} 49.096 \\ 49.096 \\ 49.096 \\ 0 \\ 0 \\ 0 \end{bmatrix}$$ matrix mean internal stress in MPa

for 0.2,

$$\frac{\sigma_m}{10^6} = \begin{bmatrix} 49.096 \\ 49.096 \\ 49.096 \\ 0 \\ 0 \\ 0 \end{bmatrix}$$ matrix mean internal stress in MPa

4.12 Appendix D

Mathcad 7.0 document to determine strains in the matrix and reinforcement from Eshelby theory for an externally applied stress

$E_M := 74.514$

$\nu_M := 0.39$

$G_M := 26.8$

properties of austenite as determined from various bounds (E_m and G_m are in GPa)

$\alpha_M := 11 \cdot 10^{-6}$ average coefficient of thermal expansion for matrix in K^{-1}

$F := 0.1$ volume fraction of inclusions

$\alpha_I := 7.3 \cdot 10^{-6}$ average coefficient of thermal expansion for inclusion in K^{-1}

$T_F := 756$ lowest temperature at which mismatch is zero in °C

$T_R := 25$ room temperature °C

$$C_I := \begin{bmatrix} 515 & 106 & 106 & 0 & 0 & 0 \\ 106 & 515 & 106 & 0 & 0 & 0 \\ 106 & 106 & 515 & 0 & 0 & 0 \\ 0 & 0 & 0 & 179 & 0 & 0 \\ 0 & 0 & 0 & 0 & 179 & 0 \\ 0 & 0 & 0 & 0 & 0 & 179 \end{bmatrix} \cdot 10^9$$ Stiffness tensor for inclusion (Pa)

$$S_{11} := \frac{1}{E_M} \qquad S_{12} := \frac{-\nu_M}{E_M} \qquad S_{44} := 2\left(S_{11} - S_{12}\right)$$

$$C_{11} := \frac{S_{11} + S_{12}}{\left(S_{11} - S_{12}\right)\left(S_{11} + 2S_{12}\right)} \qquad C_{44} := \frac{1}{S_{44}}$$

$$C_{12} := \frac{-S_{12}}{\left(S_{11} - S_{12}\right) \cdot \left(S_{11} + 2S_{12}\right)}$$

$C_{11} = 148.638$

$C_{12} = 95.031$

$C_{44} = 26.804$

Eshelby S tensor for spherical inclusions

$$S := \begin{bmatrix} \frac{7-5\nu_M}{15(1-\nu_M)} & \frac{-1+5\nu_M}{15(1-\nu_M)} & \frac{-1+5\nu_M}{15(1-\nu_M)} & 0 & 0 & 0 \\ \frac{-1+5\nu_M}{15(1-\nu_M)} & \frac{7-5\nu_M}{15(1-\nu_M)} & \frac{-1+5\nu_M}{15(1-\nu_M)} & 0 & 0 & 0 \\ \frac{-1+5\nu_M}{15(1-\nu_M)} & \frac{-1+5\nu_M}{15(1-\nu_M)} & \frac{7-5\nu_M}{15(1-\nu_M)} & 0 & 0 & 0 \\ 0 & 0 & 0 & \frac{8-10\nu_M}{15(1-\nu_M)} & 0 & 0 \\ 0 & 0 & 0 & 0 & \frac{8-10\nu_M}{15(1-\nu_M)} & 0 \\ 0 & 0 & 0 & 0 & 0 & \frac{8-10\nu_M}{15(1-\nu_M)} \end{bmatrix}$$

$$C_M := \begin{bmatrix} C_{11} & C_{12} & C_{12} & 0 & 0 & 0 \\ C_{12} & C_{11} & C_{12} & 0 & 0 & 0 \\ C_{12} & C_{12} & C_{11} & 0 & 0 & 0 \\ 0 & 0 & 0 & C_{44} & 0 & 0 \\ 0 & 0 & 0 & 0 & C_{44} & 0 \\ 0 & 0 & 0 & 0 & 0 & C_{44} \end{bmatrix} \cdot 10^9$$

Stiffness tensor for matrix

$$I := \begin{bmatrix} 1 & 0 & 0 & 0 & 0 & 0 \\ 0 & 1 & 0 & 0 & 0 & 0 \\ 0 & 0 & 1 & 0 & 0 & 0 \\ 0 & 0 & 0 & 1 & 0 & 0 \\ 0 & 0 & 0 & 0 & 1 & 0 \\ 0 & 0 & 0 & 0 & 0 & 1 \end{bmatrix}$$

$$\varepsilon_{TM} := \left(\alpha_M - \alpha_I\right)\left(T_F - T_R\right) \cdot \begin{bmatrix} 1 \\ 1 \\ 1 \\ 0 \\ 0 \\ 0 \end{bmatrix}$$

thermal mismatch strain

$$\varepsilon_{TTM} := \left[-\left[\left(C_M - C_I\right)\cdot(S - F\cdot(S - I)) - C_M\right]\right]^{-1} \cdot C_I \cdot \varepsilon_{TM}$$

equivalent transformation strain from thermal mismatch

$$\sigma_A := \begin{bmatrix} (-415)\cdot 10^6 \\ 0 \\ 0 \\ 0 \\ 0 \\ 0 \end{bmatrix}$$

Applied external stress in Pa

$$\varepsilon_{TEM} := \left[-\left[\left(C_M - C_I\right)\cdot(S - F\cdot(S - I)) - C_M\right]^{-1}\right]\cdot\left[\left(C_M - C_I\right)\cdot C_M^{-1}\cdot\sigma_A\right]$$

equivalent transformation strain from elastic mistmatch

$\sigma_{MM} := -F \cdot C_M \cdot (S - I) \cdot \varepsilon_T$ $\sigma_{MI} := (1 - F) \cdot C_M \cdot (S - I) \cdot \varepsilon_T$

$\sigma_M := \sigma_A + \sigma_{MM}$

$\sigma_I := \sigma_A + \sigma_{MI}$

$\varepsilon_M := C_M^{-1} \cdot \sigma_M$

$\varepsilon_I := C_I^{-1} \cdot \sigma_I$

$$\sigma_A = \begin{bmatrix} -4.15 \cdot 10^8 \\ 0 \\ 0 \\ 0 \\ 0 \\ 0 \end{bmatrix}$$

$$\frac{\sigma_M}{10^6} = \begin{bmatrix} -364.743 \\ 15.241 \\ 15.241 \\ 0 \\ 0 \\ 0 \end{bmatrix}$$

average stress in matrix

$$\varepsilon_M = \begin{bmatrix} -5.055 \cdot 10^{-3} \\ 2.034 \cdot 10^{-3} \\ 2.034 \cdot 10^{-3} \\ 0 \\ 0 \\ 0 \end{bmatrix}$$

average strair in matrix

$$\frac{\sigma_I}{10^6} = \begin{bmatrix} -867.312 \\ -137.171 \\ -137.171 \\ 0 \\ 0 \\ 0 \end{bmatrix}$$

average stress in inclusion

$$\varepsilon_I = \begin{bmatrix} -1.714 \cdot 10^{-3} \\ 7.161 \cdot 10^{-5} \\ 7.161 \cdot 10^{-5} \\ 0 \\ 0 \\ 0 \end{bmatrix}$$

average strair in inclusion

Chapter 5

Crystallography of Stress-Induced Martensitic Transformations in NiTi and NiTi-TiC Composites

Evolution of texture distributions in austenite and martensite are examined as a function of stress and strain by Rietveld refinements. Using the lattice parameters determined in this work, transformation strains are calculated for each of the 12 lattice correspondence variants of martensite that can form from symmetry. The martensite that forms has the same orientation as martensite subjected to (11-1) Type 1 twinning. Owing to the unique lattice correspondence between austenite and martensite, the austenite develops texture as well. Due to reasons of strain compatibility, the martensite that exists at higher stress is less textured than martensite that exists at lower stresses and martensite that forms in the presence of TiC is less textured than martensite that forms without TiC. The linearity observed between volume fraction of martensite and the superelastic strain is explained by suggesting that the superelastic strain arises as a product of the volume fraction of martensite present and a summation (over all variants) of a product of the strain associated with the formation of a variant and a texture function that introduces the fraction of all variants that are of that orientation.

5.1 Theoretical background

As the parent austenite phase transforms to martensite, various orientations of martensite with crystallographically equivalent but different habit plane indices form. The habit plane is the plane that separates the parent phase from martensite and along which shear occurs during the transformation. The various orientations of martensite with these different habit plane indices are called habit plane variants. These habit plane variants can be further divided in to units that have a unique lattice correspondence with the parent phase. The lattice correspondence is a unique relationship between the initial (parent or austenite) and final (martensite) lattices. The equivalent lattice correspondences constitute the correspondence variants [9, 73].

Austenitic NiTi has a CsCl (B2) structure and martensitic NiTi has a (B19') monoclinic 2H structure. The lattice correspondence has been established to be of the type [76, 77]:

$$(001)_M \,//(011)_{B2}, [\bar{1}10]_M \,//[\bar{1}\bar{1}0]_{B2} \qquad \text{..... 5.1}$$

This relation can be fulfilled by a total of 12 crystallographically different correspondence variants. Each of these 12 crystallographically different correspondence variants yields two crystallographically equivalent habit plane variants making a total of 24 habit plane variants.

Table 5.1 shows the lattice correspondence between martensite variants and the parent austenitic phase [78]. Due to the choice of axes in the Rietveld refinement program GSAS, we take b to be the unique axis of the monoclinic cell, a convention followed by [78] and [31].

5.1.1 Computation of transformation strains

Given the unique correspondence in Table 5.1, strains associated with the transformation from the parent austenite phase to a given variant can be computed. Here the method suggested by [73] is followed for lattice parameters determined by Rietveld refinement from earlier chapters of this work. The transformation can be thought to occur by a pathway that includes

(i) rotation (R)

(ii) distortion (D)

(iii) shear (S)

with their respective tensorial representations in brackets. The rotation R aligns the principal axes of the martensite variant with the principal axis of the austenite parent phase according to relationships in Table 5.1. The distortion D equates the lengths of these axes while the shear S introduces the necessary displacement to form the monoclinic cell. The product DS is usually referred to as the deformation gradient tensor, G [79]. The components of the deformation gradient tensor can thus be easily determined from geometrical considerations. For the convention chosen above

$$G_{ij} = \begin{bmatrix} \frac{a}{d_{100,B2}} & 0 & \frac{-c\sin\theta}{2d_{110,B2}} \\ 0 & \frac{b}{2d_{110,B2}} & 0 \\ 0 & 0 & \frac{c\cos\theta}{2d_{110,B2}} \end{bmatrix} \quad \text{..... 5.2}$$

where a, b and c are lattice parameters of the monoclinic martensite (θ being the deviation from 90° of the unique axis) and $d_{100,B2}$ and $d_{110,B2}$ are the lattice spacing in the <100> and <110> directions in the parent austenite phase. A normalized R is calculated for each correspondence variant such that

$$R\cdot\begin{bmatrix}1\\0\\0\end{bmatrix}\cdot\sqrt{d_{11}^2+d_{12}^2+d_{13}^2}=\begin{bmatrix}d_{11}\\d_{12}\\d_{13}\end{bmatrix}$$
$$R\cdot\begin{bmatrix}0\\1\\0\end{bmatrix}\cdot\sqrt{d_{21}^2+d_{22}^2+d_{23}^2}=\begin{bmatrix}d_{21}\\d_{22}\\d_{23}\end{bmatrix} \quad \text{..... 5.3}$$
$$R\cdot\begin{bmatrix}0\\0\\1\end{bmatrix}\cdot\sqrt{d_{31}^2+d_{32}^2+d_{33}^2}=\begin{bmatrix}d_{31}\\d_{32}\\d_{33}\end{bmatrix}$$

where the lattice correspondence is given by

$$\begin{aligned}&[d_{11}d_{12}d_{13}]_{B2}\,//\,[100]_M\\&[d_{21}d_{22}d_{23}]_{B2}\,//\,[010]_M\\&[d_{31}d_{32}d_{33}]_{B2}\,//\,[001]_M\end{aligned} \quad \text{..... 5.4}$$

The transformation strain along <hkl> (parent basis) for a variant with rotation R is hence given by

$$\varepsilon_{hkl}^{var}=\frac{\left|R\cdot G\cdot R^{-1}\cdot v\right|}{|v|}-1 \quad \text{..... 5.5}$$

where $v=\begin{bmatrix}h\\k\\l\end{bmatrix}$.

5.1.2 Twinning in martensite

Of relevance to the following discussion is a consideration of deformation in stress-induced martensite after it forms from austenite. Two types of twinning have been reported for martensitic NiTi: Type I twinning, with a mirror reflection about the twinning plane K_1 = (11-1) and Type II twinning with twinning plane K_1 = (0.7205 1 -1), leading to a rotation by 180° around the shear direction η = [0-11] [76, 77, 80, 81].

Previous work [31] has investigated martensitic NiTi subjected to twinning under compressive loads by neutron diffraction. Here, diffraction intensity results showed that twinning occurred by variant reorientation by (11-1) Type I twinning. Variants with (100) planes

perpendicular to the loading axis were favored and this was justified by computing the average shape strains.

5.2 Experimental observations

5.2.1 Transformation strains from measured lattice parameters

Using the Rietveld refinement procedure as outlined in the previous chapters, the diffraction spectra for martensite give the best fit with the $P112_1/m$ structure, confirming the generally admitted structure [82, 83]. The lattice parameters for martensite are obtained from a spectrum at the lowest possible stress during loading at which a refinement converged. This corresponded to NiTi-0TiC (S1) at 490 MPa (the same sample designations used in Chapter 4 are used here). The values obtained are: a = 2.884 ± 0.001 Å, b = 4.178 ± 0.002 Å, c = 4.592 ± 0.002 Å and $\gamma = 94.75° \pm 0.04°$. For austenite, the no load lattice parameter was determined to be 3.0093 ± 0.0002 Å. Appendix A tabulates peak reflections corresponding to the $P112_1/m$ structure for martensite and the Pm3m structure for austenite. As shown for variant 6' in Appendix B, the transformation strains can be computed for the variants in Table 5.1 as outlined earlier. This is done for strains along <100>, <110> and <111> of the parent phase in Table 5.2.

5.2.2 Axial distribution plots

In Chapter 4, we used a texture index J (Eq. 4.4) to quantify the severity of the texture without looking in to details of the texture distribution. Here axial distribution plots are presented. These are identical to a slice of the pole figure because of cylindrical symmetry in the samples. The y-axis is a measure of the number of crystals that are oriented at an angle ϕ (x-axis) between the normal to the chosen plane and the loading axis, compared to a randomly oriented polycrystal.

Fig. 5.1 investigates the orientation of (100) planes in as-fabricated austenite (not trained) at the no load condition. No preferred orientation is seen in the austenite. Fig. 5.2 and Fig. 5.3 show the orientation of (100) and (111) planes for austenite and (100) and (0-11) planes for martensite, respectively, in NiTi-0TiC (S1) at 625 MPa.

To investigate texture evolution in the martensite with increasing stress, Fig. 5.4 shows the orientation of (100) planes in martensite in NiTi-0TiC (S2) at 625 MPa and 975 MPa.

Fig. 5.5 and Fig. 5.6 seeks to compare martensite that is formed in the presence of TiC particles and that which is formed in the monolithic material at the same level of superelastic strain. Two superelastic strain levels are considered i.e., 0.012 and 0.004. The corresponding samples and stress levels for a superelastic strain level of 0.012 are NiTi-0TiC (S1) at 540 MPa during loading and NiTi-10TiC (S2) at 816 MPa during loading. The corresponding samples and stress levels for a superelastic strain level of 0.004 are NiTi-0TiC (S1) at 480 MPa during loading and NiTi-10TiC (S2) at 466 MPa during unloading. As described in Chapter 3, the superelastic strain, unlike stress, is a fundamental global quantity characterizing the phase strains, phase fractions and texture evolution in the transformation independently. Hence data of the same superelastic strain from different samples can be directly compared. The orientation of (100) planes are plotted in these figures.

The following discussion revisits some experimental observations made in earlier chapters which will be discussed in light of the texture evolution and transformation shape strains in §5.3.

5.2.3 Macroscopic response of NiTi-0TiC and NiTi-10TiC

When samples of NiTi-0TiC and NiTi-10TiC were further stressed (Fig. 4.14), no additional twinning in the martensite was observed but rather the samples began to accumulate non-recoverable plastic strain attributed to dislocation plasticity in martensite. Thus, it can be concluded that neither additional stress-induced martensite formation nor martensite twinning occurred.

5.2.4 Magnitude of recoverable strain in NiTi-0TiC and NiTi-10TiC

As mentioned in Chapter 2, the total recoverable strain in NiTi-0TiC in tension has been reported to be up to 8%. In Chapter 4, we reported lower recoverable strains of about 4.2% in NiTi-10TiC when it was subjected to compression loading. The magnitude of recoverable strain in NiTi-10TiC was less than that in NiTi-0TiC. At a stress of 975 MPa, 4.2% strain (elastic and superelastic) was recoverable in NiTi-0TiC, while 3.0% strain was recoverable in NiTi-10TiC (Fig. 4.1). Both NiTi-0TiC and NiTi-10TiC were loaded until slip occurred to confirm this observation as discussed in detail in Chapter 4.

5.2.5 Relationship between volume fraction of martensite and superelastic strain

A linear relationship was observed in Fig. 4.5 between the volume fraction of martensite formed and the superelastic strain for both NiTi-0TiC and NiTi-10TiC. The total superelastic strain corresponding to 100% transformation to martensite is less in NiTi-10TiC (2.0%) than in NiTi-0TiC (2.3%). This means that the same volume of martensite in the presence of TiC has less transformation shape strains associated with it than martensite formed without TiC particles.

5.3 Discussion in the context of texture evolution

Table 5.2 shows a non-unique relationship between variant type and transformation strain. In addition, since negative numbers denote compressive strains and positive numbers denote tensile strain, a clear asymmetry is seen in tension vs. compression behavior, especially with regard to the number of possible variants. This may explain why only 4.2% strain is recoverable in NiTi in compression compared to up to 8% in tension. A similar theory is proposed by [84] who use different lattice parameters to determine transformation strains and a different choice of coordinate axes.

Since the samples were fabricated using Hot Isostatic Pressing (HIP), no significant texture is expected in the starting material. This explains the observation in Fig. 5.1. This is consistent with a value of near unity obtained for the texture index J from Rietveld refinements in earlier chapters. Fig. 5.3 shows a highly textured martensite with its (100) planes aligned perpendicular to the loading axis and its (0-11) planes aligned parallel to the loading axis. This configuration was observed previously by [31] for the case of martensitic NiTi subjected to compression loading. The configuration was justified by examining strains associated with variant combinations corresponding to (11-1) Type 1 twinning. This corresponded to variant conversions to 1, 1', 2 and 2'. Thus stress-induced martensite when formed under compression forms with a structure similar to a (11-1) Type 1 twinned structure. In both cases on additional loading, slip occurs and no further twinning is possible to generate strain.

Given the unique lattice correspondence in Table 5.1, the austenite can be expected to develop texture as well. For variant 1 formation, the martensite (100) plane forms from the austenite (100) plane. This explains the observation in Fig. 5.2a where austenite (100) planes perpendicular and parallel to the loading axis disappear. This variant conversion also implies austenite (111) planes align perpendicular to the loading axis as seen in Fig. 5.2b.

Previously, by reporting the texture index (Fig. 4.7), it was observed that martensite existing at higher stresses was less textured than martensite existing at lower stresses. This is again seen for the orientation of (100) planes in martensite in Fig. 5.4. Initially, favorable (with respect to stress) orientations of austenite transform to martensite. However, the martensite that forms later needs to be compatible with the existing martensite and the austenite. This constraint results in not-so favorable orientations of martensite forming and hence an overall reduction in texture is observed. However, the martensite that is formed still generates the same amount of strain since the relationship between superelastic strain and the volume fraction martensite is linear (Fig. 4.5). This is understandable since more than one orientation of martensite can give the same strain, as seen in the transformation shape strains reported in Table 5.2. Thus given this non-unique correspondence between transformation strain and variant orientation, the linearity may be justified.

In the light of the above behavior, the following description of the recoverable superelastic strain is proposed. The superelastic strain along <hkl>, ε^*_{hkl}, can be thought to arise due to the volume fraction of martensite present (V_m), the strain associated with the formation of a variant i, ε^i_{hkl} (Eq. 5.5), and a texture function, F_i, that introduces the fraction of all variants that are of type i where the summation is over all 12 correspondence variants in Table 5.1:

$$\varepsilon^*_{hkl} = 2V_m \sum_i F_i \varepsilon^i_{hkl} \qquad \text{..... 5.6}$$

The factor of 2 is introduced since there are 24 habit plane variants. Thus even though the texture evolves as seen in Fig. 4.7 and Fig. 5.4, the total superelastic strain (per unit volume of martensite) which depends on the texture and the strain in particular variants is the same, i.e, $\sum_i F_i \varepsilon^i_{hkl}$ in Eq. 5.6 is constant.

Comparing the texture of martensite formed in the presence of TiC and absence of TiC particles at the same superelastic strain level, Fig. 5.5 and Fig. 5.6 suggests that martensite with TiC is less textured. This is understandable given that there are more constraints when TiC is present. This is analogous to the situation of martensite forming at lower strains being more textured than the martensite that is formed at higher stresses. However, the extension from texture to recoverable strain is not straight forward because of the non-uniqueness of variant orientation and transformed strain.

5.4 Conclusions

The texture evolution is quantified from Rietveld refinements and texture arguments are used to explain observations in the preceding chapters. The findings are summarized below:

(1) The martensite that forms has a texture that is consistent with martensite subjected to (11-1) Type 1 twinning. (100) planes line up perpendicular to the loading axis and (0-11) planes are parallel to the loading axis. Hence on further loading after complete transformation, there are no strains associated with twinning but rather slip due to dislocation plasticity.

(2) Owing to the unique correspondence between austenite and martensite phases, the austenite which is initially texture free develops texture as well.

(3) For reasons of strain compatibility, the martensite that exists at higher stresses is less textured that the martensite that exists at lower stresses. Similarly, the martensite that forms in the presence of TiC is less textured than martensite in the monolithic material.

(4) The non-unique correspondence between variants and the transformed strain can justify a linear relationship between the volume of martensite formed and the superelastic strain.

(5) The superelastic strain can be thought to arise as a product of the volume fraction of martensite present and a summation (over all variants) of a product of the strain associated with the formation of a variant and a texture function that introduces the fraction of all variants that display this orientation. Thus the extension from texture to recoverable strain is not straight forward.

(6) Phenomenologically, the transformation strains associated with martensite forming in the presence of TiC are less than those forming without TiC. This could occur because of the need to satisfy strain compatibility between TiC and the transformed martensite.

5.5 Tables

Variant	$[100]_M$	$[010]_M$	$[001]_M$
1	$[100]_{B2}$	$[011]_{B2}$	$[0\text{-}11]_{B2}$
1'	$[\text{-}100]_{B2}$	$[0\text{-}1\text{-}1]_{B2}$	$[0\text{-}11]_{B2}$
2	$[100]_{B2}$	$[0\text{-}11]_{B2}$	$[0\text{-}1\text{-}1]_{B2}$
2'	$[\text{-}100]_{B2}$	$[01\text{-}1]_{B2}$	$[0\text{-}1\text{-}1]_{B2}$
3	$[010]_{B2}$	$[\text{-}101]_{B2}$	$[101]_{B2}$
3'	$[0\text{-}10]_{B2}$	$[10\text{-}1]_{B2}$	$[101]_{B2}$
4	$[010]_{B2}$	$[101]_{B2}$	$[10\text{-}1]_{B2}$
4'	$[0\text{-}10]_{B2}$	$[\text{-}10\text{-}1]_{B2}$	$[10\text{-}1]_{B2}$
5	$[001]_{B2}$	$[1\text{-}10]_{B2}$	$[110]_{B2}$
5'	$[00\text{-}1]_{B2}$	$[\text{-}110]_{B2}$	$[110]_{B2}$
6	$[001]_{B2}$	$[110]_{B2}$	$[\text{-}110]_{B2}$
6'	$[00\text{-}1]_{B2}$	$[\text{-}1\text{-}10]_{B2}$	$[\text{-}110]_{B2}$

Table 5.1 Lattice correspondence between martensite variants (indexed M) and B2 parent austenite phase (indexed B2) [78].

Variant	$<100>_{B2}$	$<010>_{B2}$	$<001>_{B2}$
1	-4.2	2.7	-2.5
1'	-4.2	-3.4	-2.5
2	-4.2	2.7	8.1
2'	-4.2	-3.4	0.3
3	3.4	-3.4	0.3
3'	-3.4	2.7	8.1
4	3.4	-3.4	-2.5
4'	3.4	2.7	-2.5
5	3.4	8.3	0.3
5'	3.4	8.3	8.1
6	3.4	-1.7	-2.5
6'	3.4	-1.7	-2.5

Table 5.2 Stress-induced transformation strains (%), along $<100>_{B2}$, $<110>_{B2}$ and $<111>_{B2}$ calculated from Appendix B.

5.6 Figures

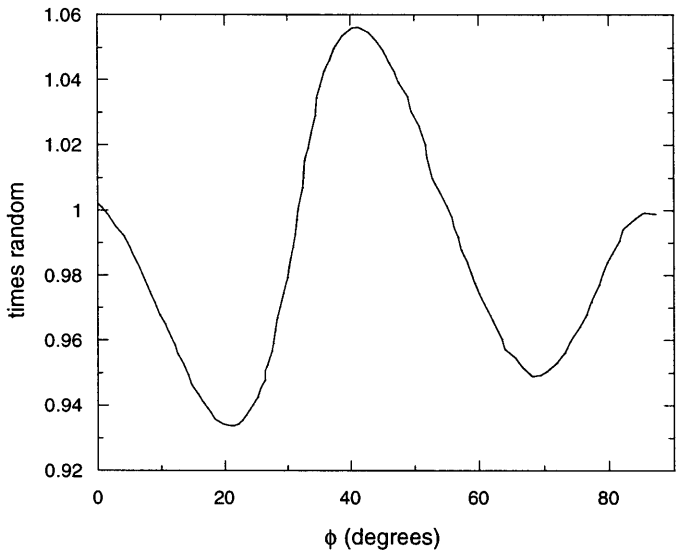

Fig. 5.1 (100) axial distribution plot for austenite in a as-fabricated NiTi-0TiC sample (no training) at 8 MPa.

(a)

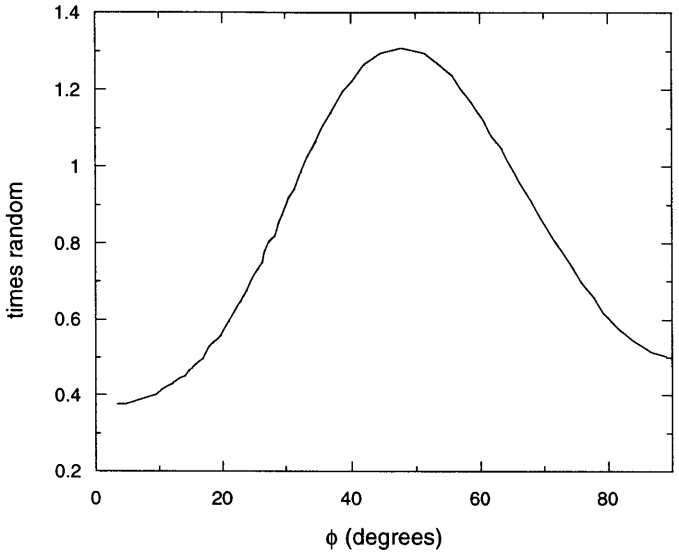

(b)

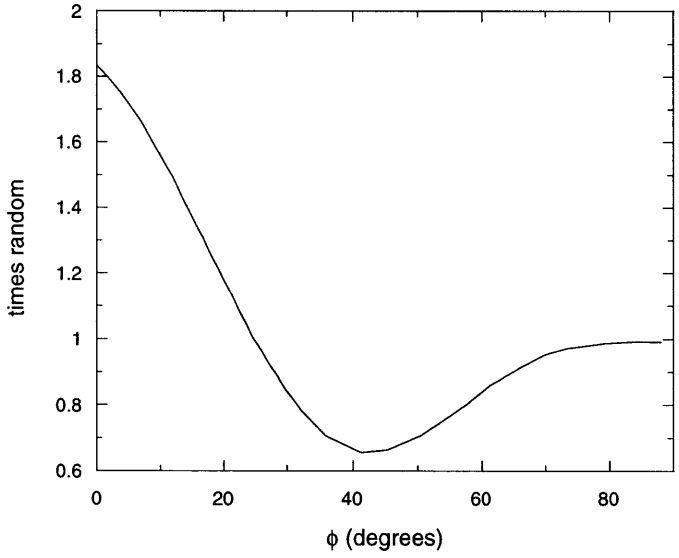

Fig. 5.2 (a) (100) and (b) (111) axial distribution plot for austenite in NiTi-0TiC (S1) at 625 MPa.

(a)

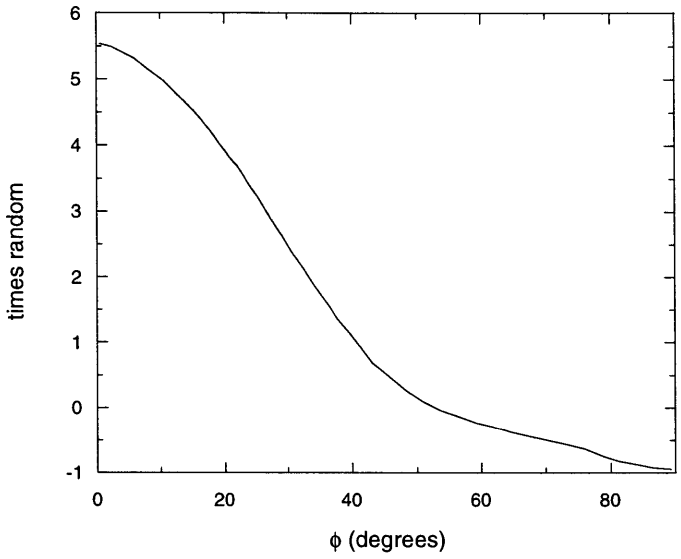

(b)

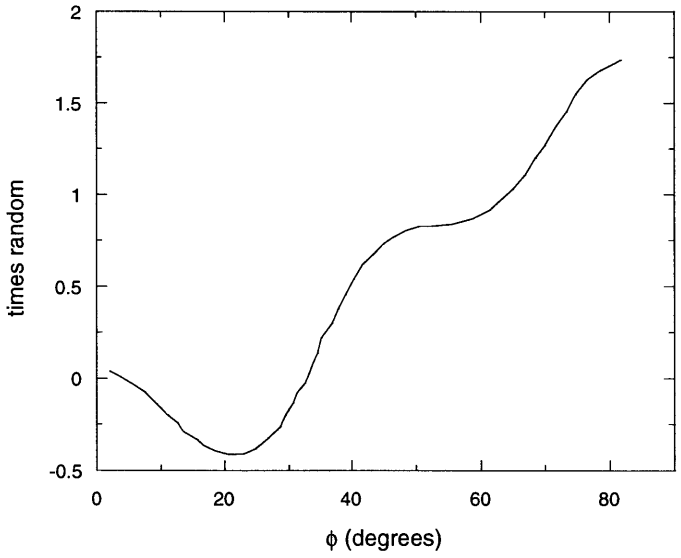

Fig. 5.3 (a) (100) and (b) (0-11)axial distribution plot for martensite in NiTi-0TiC (S1) at 625 MPa.

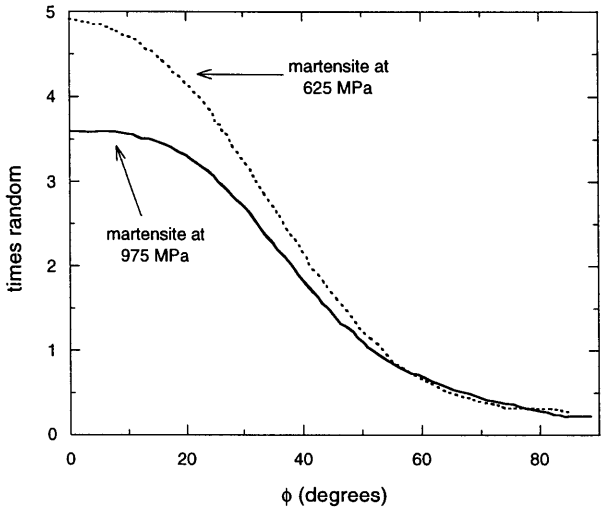

Fig. 5.4 (100) axial distribution plot for martensite in NiTi-0TiC at 625 MPa and 975 MPa.

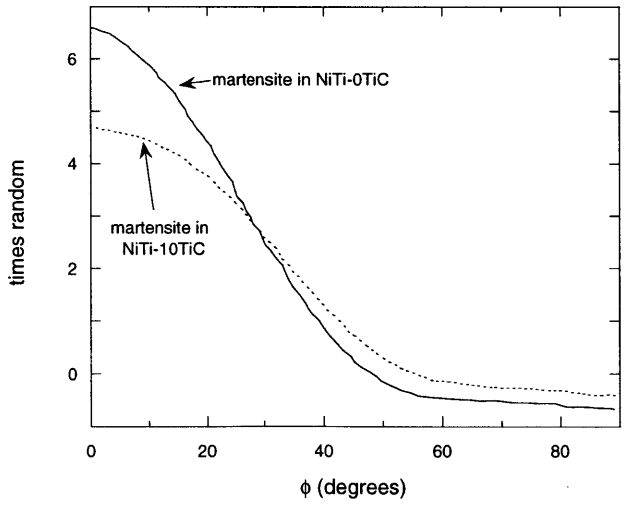

Fig. 5.5 (100) axial distribution plot for martensite in NiTi-0TiC and NiTi-10TiC at a superelastic strain of 0.012 (NiTi-10TiC (S2) is at 816 MPa during loading and NiTi-0TiC (S1) is at 540 MPa during loading).

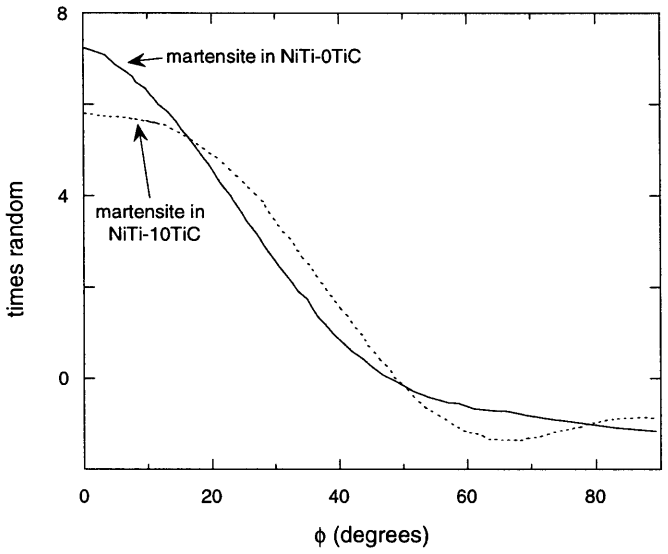

Fig. 5.6 (100) axial distribution plot for martensite in NiTi-0TiC and NiTi-10TiC at a superelastic strain of 0.004 (NiTi-10TiC (S2) is at 466 MPa during unloading and NiTi-0TiC (S1) is at 482 MPa during loading).

5.7 Appendix A

The d spacing of various hkl reflections for austenite in NiTi-0TiC at no load (as-fabricated sample without training). The scattering vector is parallel to the loading direction. F^2 is the sum of the squares of the cosine and sine parts of the structure factor (see page 115 [39]).

h	k	l	Multip -licity	d spacing (Å)	F^2
1	0	0	6	3.00926	13.3
1	1	0	12	2.12787	4.025
1	1	1	8	1.7374	15.01
2	0	0	6	1.50463	3.131
2	1	0	24	1.34578	12.85
2	1	1	24	1.22853	2.371
2	2	0	12	1.06394	2.183
3	0	0	6	1.00309	8.911
2	2	1	24	1.00309	9.241
3	1	0	24	0.95161	1.382
3	1	1	24	0.90733	6.578
2	2	2	8	0.8687	1.103
3	2	0	24	0.83462	6.129
3	2	1	48	0.80426	0.8164
4	0	0	6	0.75232	0.601
4	1	0	24	0.72985	3.539
3	2	2	24	0.72985	3.673
3	3	0	12	0.70929	0.4991
4	1	1	24	0.70929	0.4052
3	3	1	24	0.69037	3.19
4	2	0	24	0.67289	0.3154
4	2	1	48	0.65668	2.251
3	3	2	24	0.64158	0.2357
4	2	2	24	0.61426	0.1586
5	0	0	6	0.60185	1.501
4	3	0	24	0.60185	1.637
5	1	0	24	0.59017	0.115
4	3	1	48	0.59017	0.1254

The d spacing of various hkl reflections for martensite in NiTi-0TiC (S2) at a maximum of load 975 MPa The scattering vector is parallel to the loading direction. F^2 is the sum of the squares of the cosine and sine parts of the structure factor (see page 115 [39]).

h	k	l	Multip -licity	d spacing (Å)	F^2
0	1	1	4	3.07927	-0.6
1	0	0	2	2.86543	839.2
-1	1	0	2	2.52841	10.9
1	0	1	4	2.35966	1.7
1	1	0	2	2.34098	1.5
0	2	0	2	2.29035	5.4
-1	1	1	4	2.16053	-9.7
0	0	2	2	2.07962	7.5
1	1	1	4	2.04004	294.8
0	2	1	4	2.00628	1.4
0	1	2	4	1.89361	-7.6
-1	2	0	2	1.86867	-5.7
1	0	2	4	1.68307	527.8
1	2	0	2	1.71884	78.3
-1	2	1	4	1.70454	-12.2
-1	1	2	4	1.60613	19.7
1	2	1	4	1.58854	-11.5
1	1	2	4	1.55474	0.7
0	2	2	4	1.53964	-0.1
0	3	0	2	1.5269	87.3
2	0	0	2	1.43272	311.9
0	3	1	4	1.43336	2.9
-1	2	2	4	1.38997	-22.0
-2	1	0	2	1.40196	84.8
-1	3	0	2	1.39804	41.5
2	0	1	4	1.3546	155.0
0	1	3	4	1.32697	-27.5
1	2	2	4	1.32488	134.0
2	1	0	2	1.33526	116.0
-2	1	1	4	1.32852	69.1
-1	3	1	4	1.32518	2.8
1	3	0	2	1.30212	-42.4
2	1	1	4	1.27135	1171.0
1	0	3	4	1.24801	1.3
-2	2	0	2	1.2642	0.1
1	3	1	4	1.24265	-7.7
-1	1	3	4	1.21565	27.7
0	3	2	4	1.23078	6.5

h	k	l	Mult-iplicity	d spacing (Å)	F^2
1	1	3	4	1.19291	80.4
0	2	3	4	1.18604	-10.4
-2	2	1	4	1.20957	0.5
2	0	2	4	1.17983	135.3
-2	1	2	4	1.16248	10.8
2	2	0	2	1.17049	832.8
-1	3	2	4	1.16023	-20.9
2	2	1	4	1.12672	21.8
2	1	2	4	1.12359	43.8
0	4	0	2	1.14517	14.7
-1	2	3	4	1.11343	31.4
1	3	2	4	1.10363	-15.6
1	2	3	4	1.07913	66.1
0	4	1	4	1.10409	14.5
-2	2	2	4	1.08026	-0.2
-1	4	0	2	1.09618	1.1
-2	3	0	2	1.09243	-35.9
0	0	4	2	1.03981	7.2
-1	4	1	4	1.05998	15.0
-2	3	1	4	1.05659	0.0
0	1	4	4	1.01401	-1.7
0	3	3	4	1.02642	-0.1
2	2	2	4	1.02002	336.7
1	4	0	2	1.03339	-0.1

5.8 Appendix B

Mathcad 7.0 document to calculate transformation strains for a typical variant (6' in this case).

$$\begin{bmatrix} d_{11} & d_{12} & d_{13} \\ d_{21} & d_{22} & d_{23} \\ d_{31} & d_{32} & d_{33} \end{bmatrix} := \begin{bmatrix} 0 & 0 & -1 \\ -1 & -1 & 0 \\ -1 & 1 & 0 \end{bmatrix}$$

Insert parent phase correspondence here;
$[d_{11}\ d_{12}\ d_{13}]_{B2}$ $[100]_m$
$[d_{21}\ d_{22}\ d_{23}]_{B2}$ $[010]_m$
$[d_{31}\ d_{32}\ d_{33}]_{B2}$ $[001]_m$

$$\alpha := \sqrt{d_{11}^2 + d_{12}^2 + d_{13}^2} \qquad \beta := \sqrt{d_{21}^2 + d_{22}^2 + d_{23}^2} \qquad \gamma := \sqrt{d_{31}^2 + d_{32}^2 + d_{33}^2}$$ normalization

$$a := \frac{d_{11}}{\alpha} \qquad b := \frac{d_{21}}{\beta} \qquad c := \frac{d_{31}}{\gamma}$$

$$d := \frac{d_{12}}{\alpha} \qquad e := \frac{d_{22}}{\beta} \qquad f := \frac{d_{32}}{\gamma}$$

$$g := \frac{d_{13}}{\alpha} \qquad h := \frac{d_{23}}{\beta} \qquad i := \frac{d_{33}}{\gamma}$$

Given

$x \cdot 1 + y \cdot 0 + z \cdot 0 = a$

$x \cdot 0 + y \cdot 1 + z \cdot 0 = b$

$x \cdot 0 + y \cdot 0 + z \cdot 1 = c$

$p \cdot 1 + q \cdot 0 + r \cdot 0 = d$

$p \cdot 0 + q \cdot 1 + r \cdot 0 = e$

$p \cdot 0 + q \cdot 0 + r \cdot 1 = f$

$l \cdot 1 + n \cdot 0 + o \cdot 0 = g$

$l \cdot 0 + n \cdot 1 + o \cdot 0 = h$

$l \cdot 0 + n \cdot 0 + o \cdot 1 = i$

$$\begin{bmatrix} aa \\ bb \\ cc \\ dd \\ ee \\ ff \\ gg \\ hh \\ ii \end{bmatrix} := \text{Find}(x, y, z, p, q, r, l, n, o) \rightarrow \begin{bmatrix} \frac{d_{11}}{\sqrt{d_{11}^2 + d_{12}^2 + d_{13}^2}} \\ \frac{d_{21}}{\sqrt{d_{21}^2 + d_{22}^2 + d_{23}^2}} \\ \frac{d_{31}}{\sqrt{d_{31}^2 + d_{32}^2 + d_{33}^2}} \\ \frac{d_{12}}{\sqrt{d_{11}^2 + d_{12}^2 + d_{13}^2}} \\ \frac{d_{22}}{\sqrt{d_{21}^2 + d_{22}^2 + d_{23}^2}} \\ \frac{d_{32}}{\sqrt{d_{31}^2 + d_{32}^2 + d_{33}^2}} \\ \frac{d_{13}}{\sqrt{d_{11}^2 + d_{12}^2 + d_{13}^2}} \\ \frac{d_{23}}{\sqrt{d_{21}^2 + d_{22}^2 + d_{23}^2}} \\ \frac{d_{33}}{\sqrt{d_{31}^2 + d_{32}^2 + d_{33}^2}} \end{bmatrix}$$

$$\begin{bmatrix} aa & bb & cc \\ dd & ee & ff \\ gg & hh & ii \end{bmatrix} = \begin{bmatrix} 0 & -0.707 & -0.707 \\ 0 & -0.707 & 0.707 \\ -1 & 0 & 0 \end{bmatrix}$$

R matrix for variant

$$\left[\left[\begin{bmatrix} aa & bb & cc \\ dd & ee & ff \\ gg & hh & ii \end{bmatrix} \cdot \begin{bmatrix} 1 \\ 0 \\ 0 \end{bmatrix} \cdot \alpha\right] - \begin{bmatrix} d_{11} \\ d_{12} \\ d_{13} \end{bmatrix}\right] = \begin{bmatrix} 0 \\ 0 \\ 0 \end{bmatrix} \qquad \left[\left[\begin{bmatrix} aa & bb & cc \\ dd & ee & ff \\ gg & hh & ii \end{bmatrix} \cdot \begin{bmatrix} 0 \\ 1 \\ 0 \end{bmatrix} \cdot \beta\right] - \begin{bmatrix} d_{21} \\ d_{22} \\ d_{23} \end{bmatrix}\right] = \begin{bmatrix} 0 \\ 0 \\ 0 \end{bmatrix}$$

$$\left[\left[\begin{bmatrix} aa & bb & cc \\ dd & ee & ff \\ gg & hh & ii \end{bmatrix} \cdot \begin{bmatrix} 0 \\ 0 \\ 1 \end{bmatrix} \cdot \gamma\right] - \begin{bmatrix} d_{31} \\ d_{32} \\ d_{33} \end{bmatrix}\right] = \begin{bmatrix} 0 \\ 0 \\ 0 \end{bmatrix}$$

Check!

$$R := \begin{bmatrix} aa & bb & cc \\ dd & ee & ff \\ gg & hh & ii \end{bmatrix}$$

$$G := \begin{bmatrix} 0.958 & 0 & -0.090 \\ 0 & 0.983 & 0 \\ 0 & 0 & 1.079 \end{bmatrix}$$

$$R \cdot G \cdot \left(R^{-1}\right) = \begin{bmatrix} 1.031 & -0.048 & 0 \\ -0.048 & 1.031 & 0 \\ -0.064 & 0.064 & 0.958 \end{bmatrix}$$

$$v := \begin{bmatrix} 1 \\ 0 \\ 0 \end{bmatrix} \qquad \left(\frac{\left| R \cdot G \cdot R^{-1} \cdot v \right|}{|v|} - 1 \right) \cdot 100 = 3.408 \qquad \text{(strain in percent)}$$

$$v := \begin{bmatrix} 1 \\ 1 \\ 0 \end{bmatrix} \qquad \left(\frac{\left| R \cdot G \cdot R^{-1} \cdot v \right|}{|v|} - 1 \right) \cdot 100 = -1.7$$

$$v := \begin{bmatrix} 1 \\ 1 \\ 1 \end{bmatrix} \qquad \left(\frac{\left| R \cdot G \cdot R^{-1} \cdot v \right|}{|v|} - 1 \right) \cdot 100 = -2.526$$

Chapter 6

Phenomenological Changes Due to Stress-Cycling in Superelastic NiTi Studied by Neutron Diffraction

The following phenomenological changes are noted from in situ neutron diffraction measurements on NiTi subjected to stress-cycling : (i) The volume fraction of martensite formed remains almost unchanged. (ii) The average phase strain in austenite remains mostly unchanged at intermediate loads but changes for unloaded austenite. (iii) The texture in martensite and austenite under load changes significantly resulting in changes in macroscopic stress-strain behavior. (iv) The isotropic and anisotropic components of the strain in austenite redistribute themselves. The reason for these changes remain unclear and a theory suggesting changes in the internal stress field to minimize mismatch is proposed. While the mechanical characteristics of stress-cycling have been previously studied, the relevance of this chapter stems from the fact that such fundamentally significant phenomenological changes are reported for the first time.

6.1 Introduction

In various applications, superelastic alloys are subjected to repetitive loading and unloading accompanied with forward and reverse martensitic transformations of the parent phase. Previous work has investigated the effects of cyclic stresses on the stress-strain curve of superelastic NiTi alloys [85-89]. The findings are summarized below for cycling at constant temperature:

(1) the residual plastic strain at zero applied stress increases with cycling;

(2) the stresses at which the martensitic transformation initiates and finishes decreases with increased cycling ;

(3) the strain or stress hysteresis becomes smaller with increased cycling;

(4) the irrecoverable strain increases with increased cycling;

(5) the transformation strain range decreases with an increase in the number of cycles;

(6) the phenomena described above becomes insensitive to cycling with increasing number of cycles, i.e., a steady state is reached where the transformation is stabilized.

While extensive knowledge exists on the engineering aspect of this stabilization, almost no work has been carried out to understand the scientific aspects of this stabilization. [89] attribute the residual strain to the occurrence of slip in the preceding deformation. The internal stresses formed by slip may assist the formation of stress-induced martensite, thereby reducing

the critical stresses needed for the transformation. The internal stress field after cyclic deformation may also be responsible for changes in the strain gradient. The final stabilization has been attributed to work hardening due to dislocations during cycling [85].

Here an attempt is made to characterize changes in superelastic NiTi subjected to stress-cycling with neutron diffraction measurements. By carrying out simultaneous neutron diffraction and stress-cycling, i.e., neutron spectra acquisition as load is applied to the sample, the stress-induced transformation can be monitored for changes with stress-cycling.

6.2 Experimental

The Sample NiTi-0TiC (S2) which was fabricated and heat treated as described in Chapter 3 was used as the starting sample. The sample was tested in the same configuration as described in the preceding chapters. A total of 101 load-unload compressive cycles were completed at room temperature, each up to 988 MPa, with diffraction data obtained at various fixed stress levels during cycles 1, 2, 3, 101 and 102. For intermediate cycles where no neutron data was collected, the ramp rate was 3 mm/min, while for neutron diffraction cycles the ramp rate was 0.1 mm/min. Average temperature changes due to transformation enthalpy dissipation of about 10-14 °C were recorded during the fast cycles. For the slower cycles during neutron data acquisition, no measurable changes in temperature were noted. Neutron data were obtained at

(1) the no load condition (in practice 8 MPa to hold the sample horizontally),

(2) 715 MPa during the loading part of the cycle,

(3) a maximum stress of 988 MPa,

(4) 545 MPa during unloading and

(5) again at the unloaded condition for each cycle. For convenience, the various stress-levels and cycle designations are tabulated in Table 6.1. An extensometer was attached to the sample to obtain macroscopic stress-strain data during cycling.

6.3 Neutron diffraction data analysis

Austenite phase strains, texture and phase volume fraction information are obtained by carrying out Rietveld refinements as explained in the preceding chapters. For texture, both the texture index (Eq. 4.4) and axial distribution plots are used from a spherical harmonics formulation in the Rietveld refinement. An average strain (Eq. 4.1) is determined for austenite as well as isotropic and anisotropic components (Eq. 4.2).

6.4 Results

Due to vibrations in the hydraulic equipment and consequent slipping of the extensometer knife edges, no satisfactory stress-strain data was obtained during many of the cycles. Data that represents the trends discussed in §6.1 can be seen on examining the 3rd and 90th cycles (Fig. 6.1). For the tested sample, the residual strain seemed to rapidly drop off. As mentioned in Chapter 2, a non-recoverable compressive plastic strain of 0.1% was recorded after the first training cycle but none was noted during the second or during the third diffraction cycle. More work to characterize the stress-strain response from mechanical tests will be carried out in [7]. However, this data has already been published (see §6.1) and is not critical to the present analysis of neutron diffraction spectra from stress-cycled NiTi.

6.4.1 Volume fraction evolution

From the bar graph in Fig. 6.2 no significant changes in volume fraction (within error) are observed with stress-cycling. Thus given the general trend that the superelastic strain is greater with stress-cycling (Fig. 6.1 and §6.1), the same volume of martensite generates a larger recoverable strain.

6.4.2 Changes in texture

Fig. 6.3 and Fig. 6.4 show the texture index J (Eq. 4.4) for martensite and austenite. The following observations are made:

(1) The texture in martensite increases on cycling at intermediate loads during loading and unloading as seen from the texture index. While the changes in texture index are not significant between Cycles C1 and C2, they are significant between Cycles C2 and C101. The axial distribution plots for (100) martensite in Fig. 6.5 and Fig. 6.6 also show a slight increase in texture at intermediate loads during loading and unloading, respectively, on stress-cycling.

(2) However, there is a significant decrease in martensite texture at maximum stress (988 MPa) on stress-cycling. This is also seen in the axial distribution plots for (100) martensite at 988 MPa from Cycles C1, C2 and C101 in Fig. 6.7. Again, while these changes are not significant between Cycles C1 and C2, they are significant between Cycles 101 and C2.

(3) There is no texture developed in the austenite at the no load condition after stress-cycling. Fig. 6.8 is the axial distribution plot for (100) austenite that confirms this observation (within error) at the no load portions of the various cycles.

(4) The texture in the austenite increases significantly after cycling. This is also seen in the axial distribution plots for austenite at 715 MPa during loading for Cycles C1, C2 and C101 (Fig. 6.9) and at 544 MPa during unloading for Cycles C1, C2 and C101 (Fig. 6.10). The changes are significant between Cycles 101 and C2.

6.4.3 Strain evolution with stress-cycling

No significant changes are observed in the average strain in austenite measured from Eq. 4.1 as seen in Fig. 6.11. However, there is a change in the residual strain (phase strain at no external load) on cycling. From Fig. 6.12, it can be seen that anisotropic and isotropic components of the strain change and redistribute themselves on cycling. Throughout this work compressive strains are reported only in magnitude as positive strains. Here owing to the sign reversal the sign and magnitude are shown in Fig. 6.11 and Fig. 6.12.

6.5 Discussion

The volume fraction of martensite formed does not significantly change with cycling but the superelastic strain at constant stress increases. Thus from Eq. 5.6, this necessarily implies that a change in texture is required so as to obtain larger strains. The fact that the volume fraction of martensite does not change in spite of other changes observed in Fig. 6.1 and §6.1 suggests that external stress is more important in deciding the transforming volumes on cycling. Due to the self-accommodating nature of the transformation, the strain generated varies due to possible changes in texture.

The driving force for changes in texture so that martensitic variants form generating larger strains is not clear. One possible reason could be due to strain redistribution occurring during repeated reversible transformations between austenite to martensite so as to minimize the mismatch between the transformed martensite and the transforming austenite. Consequently, the local internal stress field associated with grain-boundaries and interfaces is altered so as to minimize the hysteresis and associated interface friction. This alteration may result in martensite initially forming at lower stresses or more favorable orientations of martensite forming at lower stresses. However, since the final recoverable strain is the same, the texture of martensite when it exists as larger volume fractions has to be lower as is seen in Fig. 6.7. The source of changes in the internal stress field could be dislocations that are associated with slip and non-recoverable

strains (e.g., the 0.1% non-recoverable plastic strain observed between the first and second cycles in Chapter 2) as proposed by [89].

Owing to the unique lattice correspondence the austenite develops texture as well. This effect has been described in detail in Chapter 3. It is interesting to note that the austenite in the no load state is still random after cycling. Thus there is no biasing field in the no load condition to texture the austenite from the reverse transformation.

The self-accommodating nature of the transformation is again evident in the austenitic strains in Fig. 6.11. No significant changes in the austenite strains are observed expect that the residual strain after cycling is different. This could be due to the accumulated plastic strain (associated with dislocations and slip). The redistribution of the anisotropic and isotropic components of the austenite strains on stress-cycling in Fig. 6.12 could be because of

(a) changes in texture of the austenite

(b) the strain redistribution alluded to previously and which may or may not be due to slip

(c) slip associated with dislocations that is responsible for the macroscopic non-recoverable plastic strain. However since the austenite in the no load condition in Cycles 101 and Cycle 102 shows no texture (Fig. 6.8) it is unlikely that (a) dominates because changes in isotropic and anisotropic components of the strain in austenite are also observed at these no load conditions. The changes in the isotropic and anisotropic components of strain on plastic deformation have been reported for steel, substantiating (c) [47].

6.6 Conclusion

Phenomenological changes on subjecting NiTi to stress cycling are noted. Neither the volume fraction of martensite nor the average phase strains in the austenite under load changes significantly with stress-cycling. However, significant differences in texture (in the loaded specimen) are noted along with isotropic/anisotropic components of the strain in the austenite. The evolving texture is responsible for the significant changes in the macroscopic stress-strain response of NiTi with stress-cycling. The driving forces for these texture changes are not clear. A hypothesis put forward is that these changes may be due to strain redistribution, which may be a consequence of the self-accommodating nature of the transformation.

The observations reported here are fundamentally significant to understanding stress-cycling in superelastic NiTi. Here, the choice of cycles to examine these effects constitutes the

training regime where initial stabilization has been reached. The evolving texture suggests that different starting textures could drastically change the fatigue (with respect to stress-cycling) response of superelastic alloys. This could be adapted in engineering applications of superelastic materials reducing the number of training cycles needed or increasing the total fatigue life of such materials.

6.7 Tables

Cycle number	Cycle designation	Stress (MPa)
1	C1	8
1	C1	715
1	C1	988
1	C1	544
2	C2	8
2	C2	715
2	C2	988
2	C2	543
3	C3	8
101	C101	8
101	C101	715
101	C101	988
101	C101	544
102	C102	8

Table 6.1 Stress levels and cycle designations at which neutron spectra were obtained.

6.8 Figures

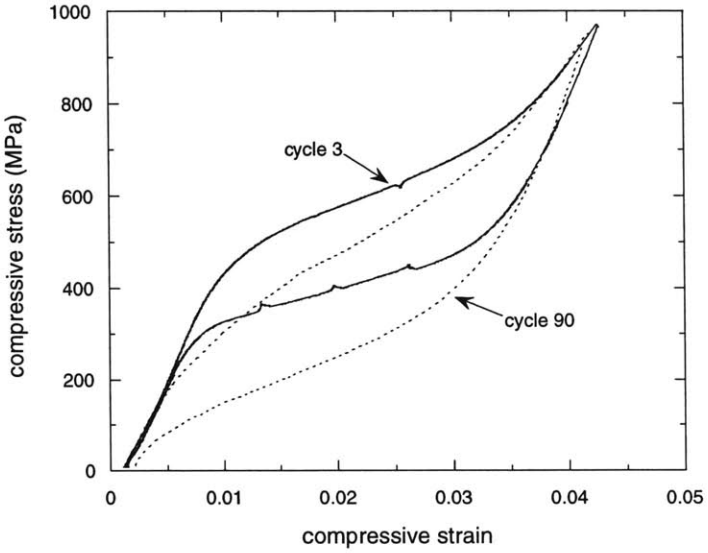

Fig. 6.1 Stress-strain response of NiTi when subjected to stress-cycling; the 3rd and 90th cycles are shown here.

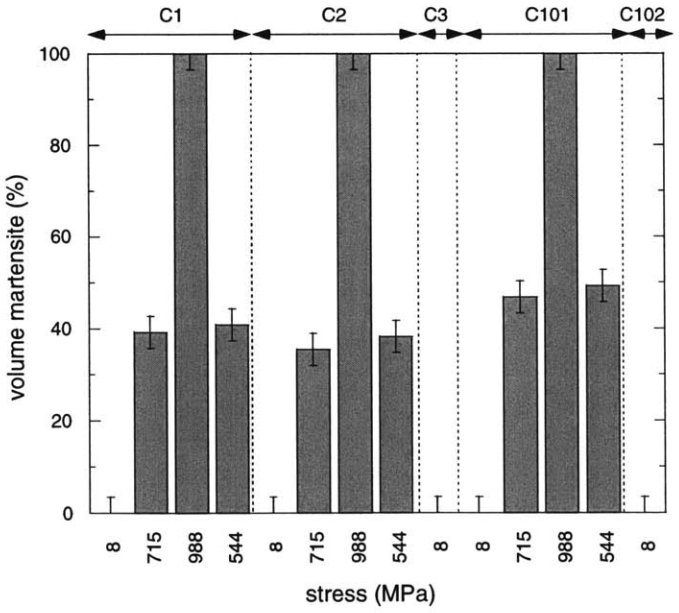

Fig. 6.2 Bar graph showing volume fraction of martensite at various stress levels for the different cycles (C).

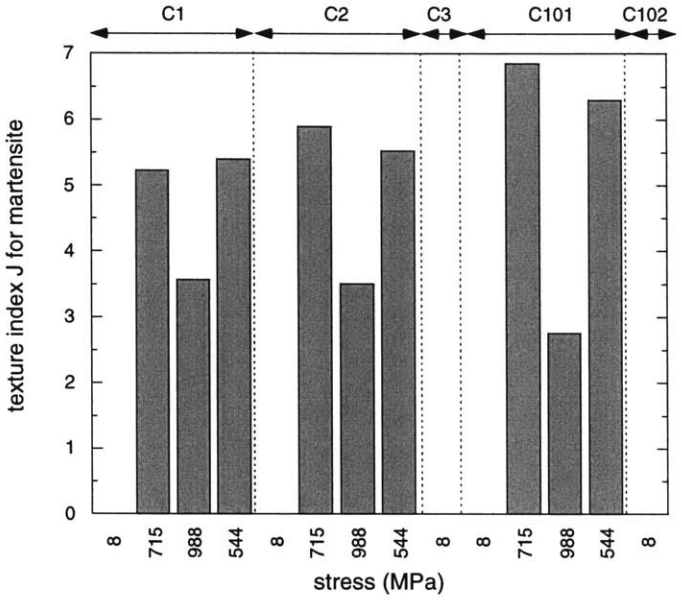

Fig. 6.3 Bar graph showing texture index J (Eq. 4.4) for martensite at various stress levels for the different cycles (C).

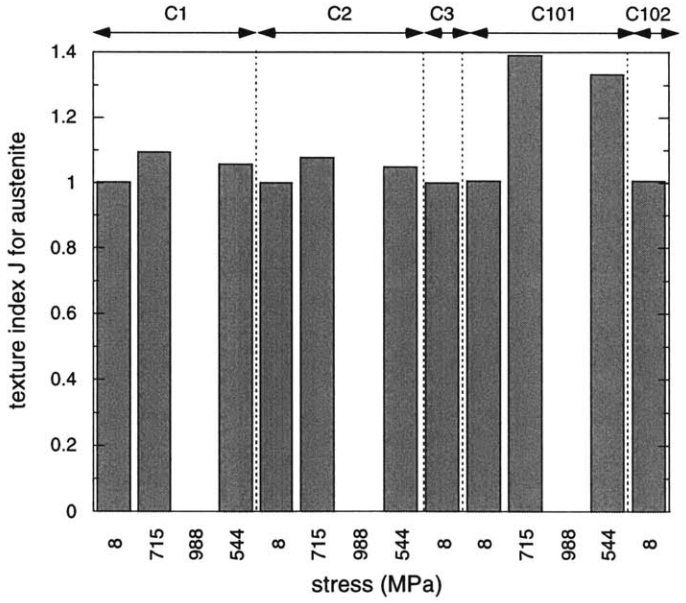

Fig. 6.4 Bar graph showing texture index J (Eq. 4.4) for austenite at various stress levels for the different cycles (C).

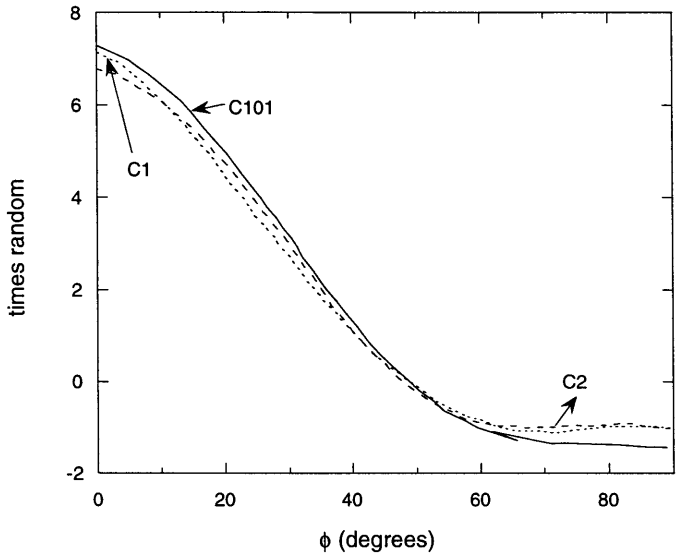

Fig. 6.5 (100) axial distribution plot for martensite at 715 MPa during loading in Cycles C1, C2, and C101.

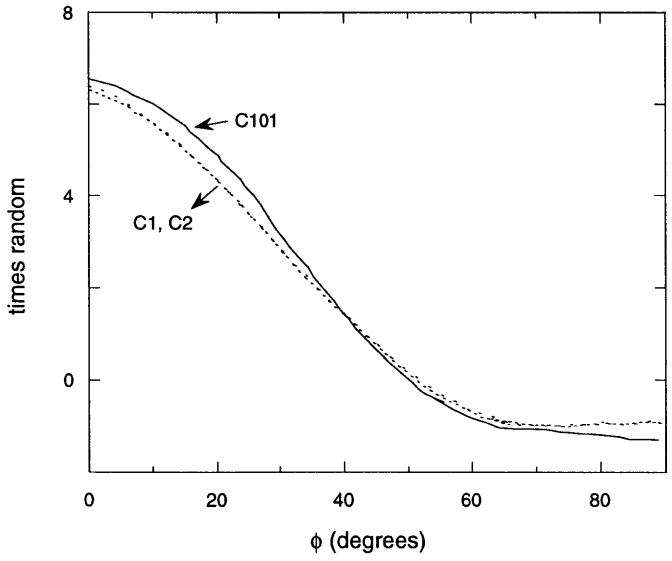

Fig. 6.6 (100) axial distribution plot for martensite at 544 MPa during unloading in Cycles C1, C2, and C101.

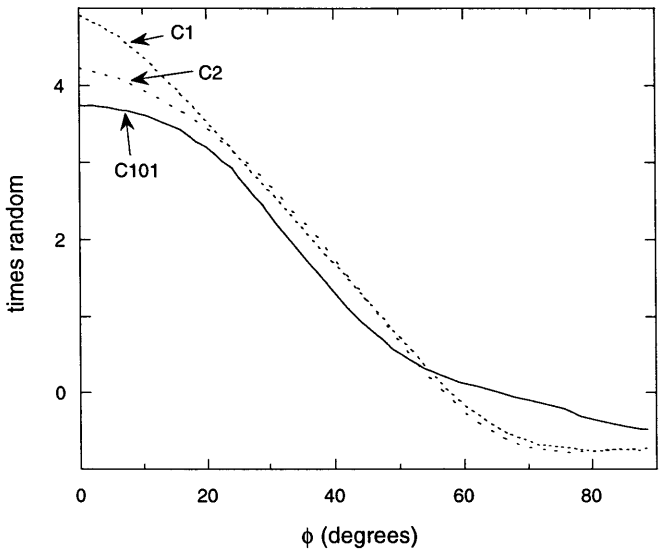

Fig. 6.7 (100) axial distribution plot for martensite at maximum load (988 MPa) during cycles C1, C2 and C101.

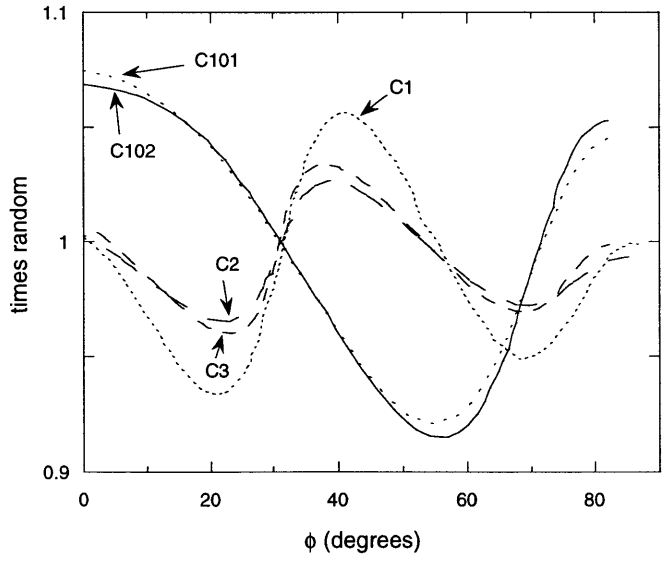

Fig. 6.8 (100) axial distribution plot for austenite in the no load condition at the start of Cycles C1, C2, C3 and C101 and C102.

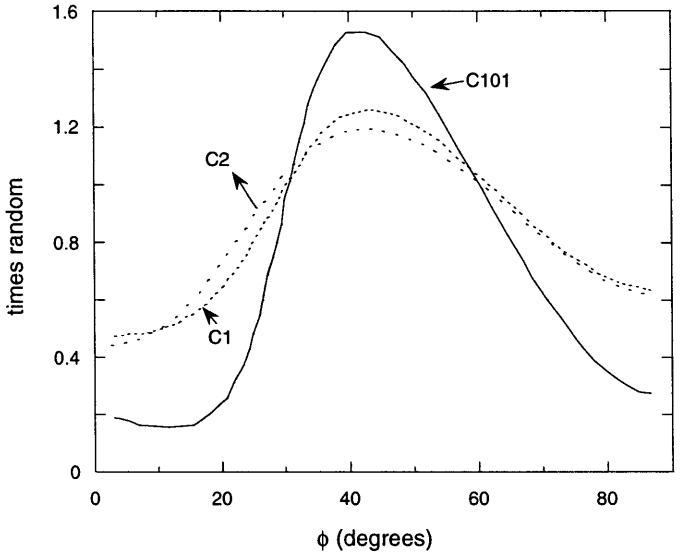

Fig. 6.9 (100) axial distribution plot for austenite at 715 MPa during loading in Cycles C1, C2, and C101.

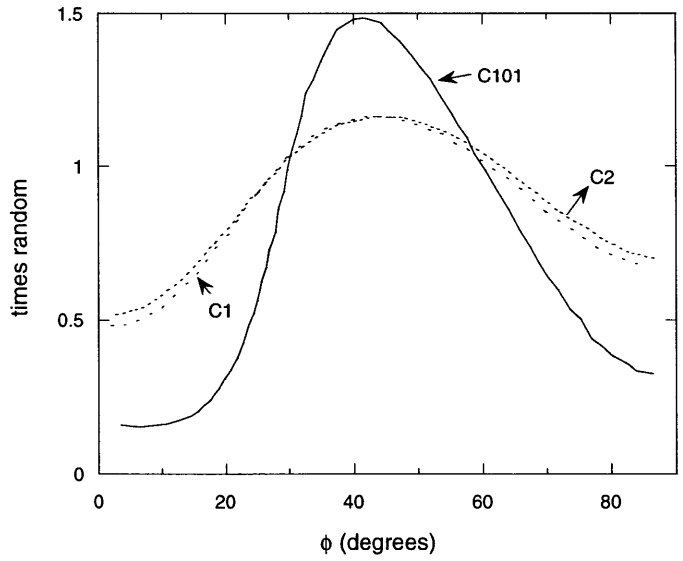

Fig. 6.10 (100) axial distribution plot for austenite at 544 MPa during unloading in Cycles C1, C2, and C101.

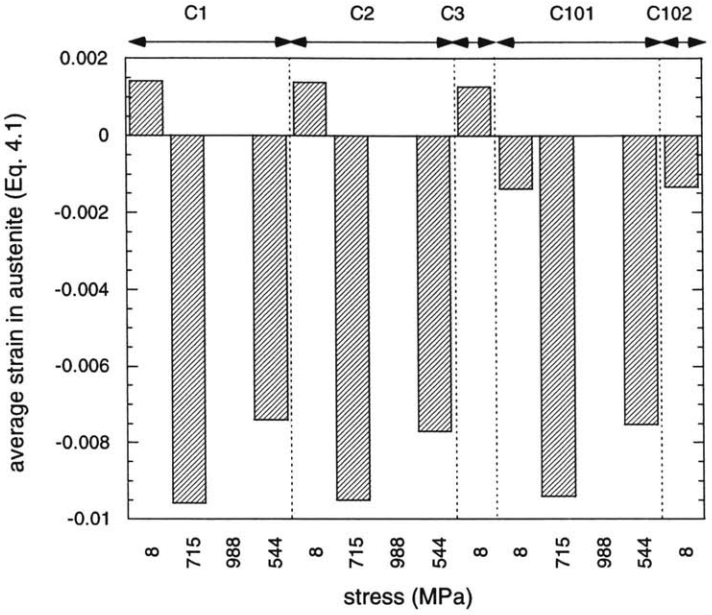

Fig. 6.11 Bar graph showing average strains in austenite (Eq. 4.1) at various stress levels for the different cycles (C). The strains are referenced to a lattice parameter of 3.0093 ± 0.0002 Å.

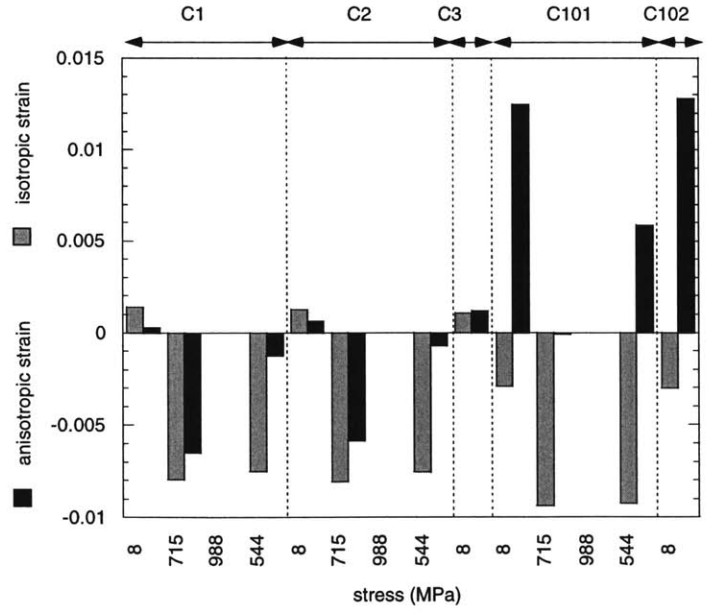

Fig. 6.12 Bar graph showing the anisotropic and isotropic components of the average strains in austenite (Eq. 4.2) at various stress levels for the different cycles (C).

Chapter 7

Preliminary Studies on the Fatigue Behavior of Shape-Memory NiTi and NiTi-TiC Composites

The work initiated to study the fatigue behavior of shape-memory NiTi and NiTi-TiC composites is described. The materials were fabricated using Hot Isostatic Pressing (HIP) and subsequently characterized. Fatigue crack growth experiments were carried out at room temperature and the results reported. A pre-cracked, compact test, shape-memory NiTi specimen was subjected to neutron diffraction measurements under various loaded and unloaded conditions. The results are presented and discussed.

7.1 Introduction

As outlined in Chapter 1, the primary focus of this work has been to study "non-slip" deformation mechanisms in materials e.g., twinning and stress-induced transformations. Until now the emphasis has been on studying stress-induced transformations since previous work (see §4.1) has investigated the behavior of shape-memory composites in uniaxial compression where the matrix deforms by twinning. Here the crack-growth behavior of such composites are presented. In addition, neutron diffraction measurements on a compact-test shape-memory specimen are performed with the aim of observing twinning due to a multi-axial state of stress ahead of a crack-tip.

In martensitic NiTi alloys, deformation can take place by twinning of martensite and strain can be recovered by a thermally induced transformation to the parent phase. This gives rise to the shape-memory effect and is illustrated schematically in Fig. 7.1. The martensitic phase consists of equal fractions of 24 variants with varying crystallographic orientations. Martensite deforms predominantly by twinning till strains of up to 8%, resulting in strong texture, as the optimally oriented variants grow at the expense of the less-favorably oriented ones. Heating results in an allotropic transformation to the parent austenitic phase and the strain accumulated by twinning of the martensite is recovered (see Fig. 7.2). If, upon subsequent cooling, the original martensite with equal volume fractions of the 24 possible variants is formed, the recovered strain is retained. However, if, upon cooling, martensite with oriented variants is formed so as to relax internal elastic stresses, the transformation is biased, some of the strain recovered upon heating is

lost, and the sample adopts a shape intermediate between those of the deformed and undeformed states. This is the two-way shape-memory effect.

Fatigue crack growth rates were measured in NiTi and found to be lower than predicted from a phenomenological law relating growth rates to the elastic modulus. No influence of M_s, the temperature of the start of the martensitic transformation, on crack growth was found. Low cycle fatigue measurements showed that the Coffin-Manson law is obeyed [89]. NiTi fracture toughness data from sharp notch tensile and Charpy tests are reported in [90] . [91] investigated the fatigue life of NiTi alloys as a function of stress and strain control, test temperature and heat-treatment. Fatigue cracks were seen to nucleate at TiC inclusions in specimens which were made by high frequency induction melting, while they nucleated along grain boundaries in specimens which were made by electron beam melting. [92] applied a strain-based lifetime rule, similar to the Manson-Coffin relation for low cycle fatigue. [93] [51] measured the fatigue crack propagation rates in NiTi at various temperatures ranging from 253K to 423K. In addition, the effect of heat-treatment and Ni-concentration was also investigated. The crack propagation rate increases with increasing Ni concentration (because of change in the transformation temperatures) and heat-treatment affects the crack propagation by changing the critical stress for slip. The temperature dependence manifests itself in the relaxation mechanism ahead of the crack tip i.e. stress-induced transformation, twin boundary movement, variant coalescence or slip.

The most comprehensive work to date on the effect of *in situ* phase transformation on fatigue-crack propagation in NiTi alloys is [94]. Studies were performed at room temperature in both non-transforming microstructures (stable austenite and stable martensite) and transforming austenitic microstructures (both reversible and non-reversible transformations to martensite). Fatigue-crack growth rates were found to be much slower in the non-transforming microstructures. The transforming microstructure had larger growth rates and a 50 to 70% decrease in the threshold stress intensity factor range. The crack-growth behavior was determined to depend on the intrinsic properties of the parent and product phase, the energy expended by the transformation and the effect of the phase change in suppressing strain localization and inducing crack-tip shielding. However, no conclusive mechanism was proposed and verified. More recently work by [95] investigated the fatigue crack growth behavior of NiTi with a martensitic transformation temperature of 80°C. Fatigue crack growth rate measurements were performed at a frequency of 10 Hz for stress ratios from 0.1 to 0.9, in both vacuum and air

at room temperature. The thresholds and near-threshold crack growth behaviors were interpreted in the context of a two-threshold model.

In summary, there is limited work underlining the fatigue and fracture mechanisms in NiTi alloys. Previous work on fatigue and fracture properties of composites does not involve mechanisms like stress-induced transformation, twin boundary movement and variant coalescence which is operative in NiTi-TiC composites. The objective of this investigation is to attempt to address some of these issues.

7.2 Experimental procedures

7.2.1 Sample fabrication

Cylindrical billets (approx. 9.1 cm by 16.5 cm) of the following shape-memory titanium-rich compositions were fabricated using Hot Isostatic Pressing (HIP):

(a) unreinforced NiTi (49.4 at.% Ni)

(b) 10 vol. % TiC in a NiTi (49.4 at.% Ni) matrix

(c) 20 vol. % TiC in a NiTi (49.4 at.% Ni) matrix

These materials (designated NiTi-0TiC, NiTi-10TiC and NiTi-20TiC) were fabricated from prealloyed NiTi powders (99.9% pure, 49.4 at.% Ni, size between 44μm and 177μm, from Specialty Metals Corp., NY) and equiaxed TiC powders (99.9% pure, 44μm average size, from Atlantic Equipment Engineers, NJ). The powder, packed in a low carbon steel container (0.318 cm thick and lined with nickel foil coated with boron nitride to prevent carbon contamination) was subjected to HIP at 1065°C and 1000 atm for three hours. Samples as described in the following sections were electrode-discharge-machined and a solutionizing treatment was used wherein the samples were held at 930°C for one hour under titanium gettered flowing argon and furnace cooled to room temperature.

7.2.2 Characterization

Electron microprobe (using a JEOL superprobe 733 calibrated with pure Ni and Ti) , wet chemical and combustion analysis (with infrared detection) were used to characterize the composition of the fabricated materials shown in Table 7.1 . Fig. 7.3 shows that the composition remains constant with distance from a TiC particle. The TiC particles were almost perfectly

stoichiometric with a composition of 49.8 ± 0.1 at.% C (as determined by combustion analysis with infrared detection).

Differential Scanning Calorimtery (see Chapter 4) and resistance measurements [96] were used to obtain the transformation temperatures associated with the start and finish of the forward and reverse transformation [10]. The results are shown in Table 7.2.

Density measurements by water-displacement show that NiTi-0TiC, NiTi-10TiC and NiTi-20TiC are 99.8%, 99.7% and 99.4%, respectively, of their theoretical density as reported in [57].

The samples were polished to 1200 grade SiC paper and 6 μm diamond paste. The etchant used was a mixture of 120 ml H_20, 15 ml HCl, 15 g Na_2SO_3 and 2g NH_4HF_2. The average grain size was 11 μm for NiTi-0TiC and 13 μm for NiTi-10TiC and NiTi-20TiC [96].

7.3 Mechanical testing

7.3.1 Tensile testing

NiTi-0TiC, NiTi-10TiC and NiTi-20TiC were tested in a controlled temperature environment at a ramp speed of 2 mm/min at 15 °C below the M_f temperatures (see Table 7.2). Details of the test setup are presented in [96] and the results are presented in Fig. 7.4.

7.3.2 Fatigue and fracture testing

Three compact test specimens (50 mm by 48 mm and 10 mm thick and sized according to ASTM 399) were tested. An INSTRON 1331 servo-hydraulic machine was used for crack growth testing. Tests were conducted at room temperature at a load ratio R (defined as the ratio of minimum load to maximum load) of 0.1 with a sinusoidal frequency of 15 Hz. Crack extension was monitored using a long-range Questar telescope system. The specimens were pre-cracked with an applied threshold stress intensity factor range ΔK of about 10 MPa$\sqrt{m}$ (with a crack approximately 0.15 cm long) and the load shed to obtain a threshold stress intensity factor range. The load was then systematically increased to obtain a failure value. Curves of crack growth rate vs. the stress intensity factor range for shape-memory NiTi-0TiC, NiTi-10TiC and NiTi-20TiC are shown in Fig. 7.5.

7.3.3 Neutron diffraction measurements

An ASTM 299 sized NiTi-0TiC compact specimen (50 mm by 48 mm and 4 mm thick) was pre-cracked with an applied stress intensity factor range, ΔK, of about 10 MPa$\sqrt{m}$. The load axis and detector orientation is the same as that described previously (Chapter 2) . The neutron beam was focused so that a spot size of 3 mm by 3 mm was obtained. This is shown schematically in Fig. 7.6. Five measurements (designated R1-R5) were obtained:

(1) a no load measurement far from the crack-tip at Spot 1 to represent the undeformed sample (R1)

(2) an ahead-of-crack tip measurement with no external load at Spot 2 (R2)

(3) an ahead-of-crack tip measurement with an applied stress intensity factor, K, of 25 MPa$\sqrt{m}$ at Spot 2 (R3)

(3) an ahead-of-crack tip measurement with an applied K of 32 MPa$\sqrt{m}$ at Spot 2 (R4)

(4) an off-axis-crack tip measurement with an applied K of 32 MPa$\sqrt{m}$ at Spot 3 (R5)

The neutron data obtained was analyzed by Rietveld refinement using a spherical harmonic texture formulation (Chapter 3).

7.4 Results and Discussions

The results of the room temperature fatigue crack growth experiments are summarized in Table 7.3, along with a Paris law exponent [97]. Here no attempt is made to compare their behaviors due to the fact that the matrix state may not be identical given the transformation temperatures in Table 7.2 and that the tests were carried out at room temperature. The idea is merely to report measured values for shape-memory composites.

The results of the neutron diffraction measurements from Rietveld refinements are presented in Table 7.4. No significant differences in lattice parameter or texture are observed. Axial distribution plots for (100) martensite are shown in Fig. 7.7. An increase in texture may be argued for R4 (see Table 7.4). The lack of any changes in texture are surprising since twin zone sizes of 4.25 mm for K = 25 MPa$\sqrt{m}$ and 7 mm for K = 32 MPa$\sqrt{m}$ are expected. These values are estimated from yield stress values for twinning (see Fig. 7.4) and using a conservative plane strain radius estimation from [97]:

$$r_p = \frac{1}{3\pi}\left(\frac{K}{\sigma_y}\right)^2 \qquad \text{..... 7.1}$$

where K is the applied stress intensity factor and σ_{is} the stress at which martensite twins. As seen in Fig. 7.6, given the various size scales, the neutron measurements are expected to observe twinning around the crack-tip. The following hypotheses to explain the lack of twinning, if real, are proposed:

(1) Neutron diffraction measurements average a 3 mm by 3 mm by 4 mm (through thickness) volume. Due to the symmetric nature of the twinned structure, the measurements do not detect significant texture because of macro-averaging.

(2) Twinning is inhibited by the plasticity ahead of the crack tip.

(3) The multiaxial state of stress ahead of the crack tip is not conducive to twinning.

(4) The twin zone size is smaller than that calculated above.

However here we consider the possibility that rather than being a negative result this may be an inaccurate result. The neutron beam may have been focused at a spot different from that indicated in Fig. 7.6 since there was no way of knowing the exact point of incidence of the neutron beam. This argument is substantiated by the fact that run R1 has the same lattice parameters as the other runs. It is unlikely that the elastic strains (that should be reflected in the lattice parameters) can relax to those of unstressed values. The statistics on the refinement are good and this does not suggest a problem with the Rietveld refinements.

7.5 Conclusions and Future work

The work initiated and the approach taken to study fracture/fatigue behavior in shape-memory NiTi and NiTi-TiC composites are presented. The final objective is to make statements on the fatigue crack growth behavior in NiTi-0TiC, NiTi-10TiC and NiTi-20TiC by repeating measurements with additional heat treatments so that the monolithic and the matrix of the composite are directly comparable. Microscopy is being carried out to understand the fracture/fatigue mechanisms involved when twinning takes place. Other work in progress includes determining the effect of the load ratio on the threshold stress intensity factor range.

The crack-tip neutron diffraction experiments will be repeated at Argonne National Laboratory. A definitive statement on twinning ahead of a crack-tip will then be made.

7.6 Acknowledgement

While the samples were fabricated at MIT, some of the sample characterization work included in this chapter were performed at Daimler-Benz AG, Germany. The involvement of Dr. K. Johansen at Daimler-Benz is acknowledged. The additional supervision of Prof. S. Suresh and Dr. U. Ramamurty and use of facilities at the Laboratory for Experimental and Computational Micromechanics (LEXCOM) at MIT is also gratefully acknowledged.

7.7 Tables

Sample	Ni (at.%)	Ni (wt.%)	0 (wt.%)	C (wt%)
NiTi-0TiC	49.5 ± 0.2	54.6 ± 0.2	0.08 ± .01	0.097 ±0.01
NiTi-10TiC	49.7 ± 0.2	54.8 ± 0.2	0.11 ± 0.01	1.43 ± 0.01
NiTi-20TiC	49.7 ± 0.2	54.8 ± 0.2	0.14 ± 0.01	2.96 ±0.03

Table 7.1 Chemical composition of shape-memory NiTi-0TiC , NiTi-10TiC and NiTi-20TiC [96].

Sample	M_f (± 2°C)	M_s (± 2°C)	A_s (± 2°C)	A_f (± 2°C)
NiTi-0TiC	35	49	66	86
NiTi-10TiC	23	40	54	75
NiTi-20TiC	-4	18	25	46

Table 7.2 Transformation temperatures (°C) of shape-memory NiTi-0TiC, NiTi-10TiC and NiTi-20TiC [96].

Sample	Stress intensity factor range ΔK (MPa√m)		Paris exponent
	threshold	failure	
NiTi-0TiC	6	30	4.5
NiTi-10TiC	8	29	6.1
NiTi-20TiC	8	28	5.2

Table 7.3 Results of fatigue crack growth experiments at room temperature for shape-memory NiTi-0TiC, NiTi-10TiC and NiTi-20TiC.

Run	Summary of run	a (± 0.002 Å)	b (± 0.003 Å)	c (± 0.004 Å)	γ (± 0.04 °)	texture index J
R1	far from crack-tip	2.897	4.119	4.645	97.52	1.030
R2	crack-tip (no load)	2.898	4.120	4.648	97.55	1.023
R3	crack-tip (K = 25 MPa√m)	2.896	4.117	4.645	97.56	1.030
R4	crack-tip (K = 32 MPa√m)	2.894	4.115	4.647	97.66	1.051
R5	off crack-tip (K = 32 MPa√m)	2.896	4.117	4.644	97.55	1.023

Table 7.4 Results of Rietveld refinements on neutron data from NiTi-0TiC.

7.8 Figures

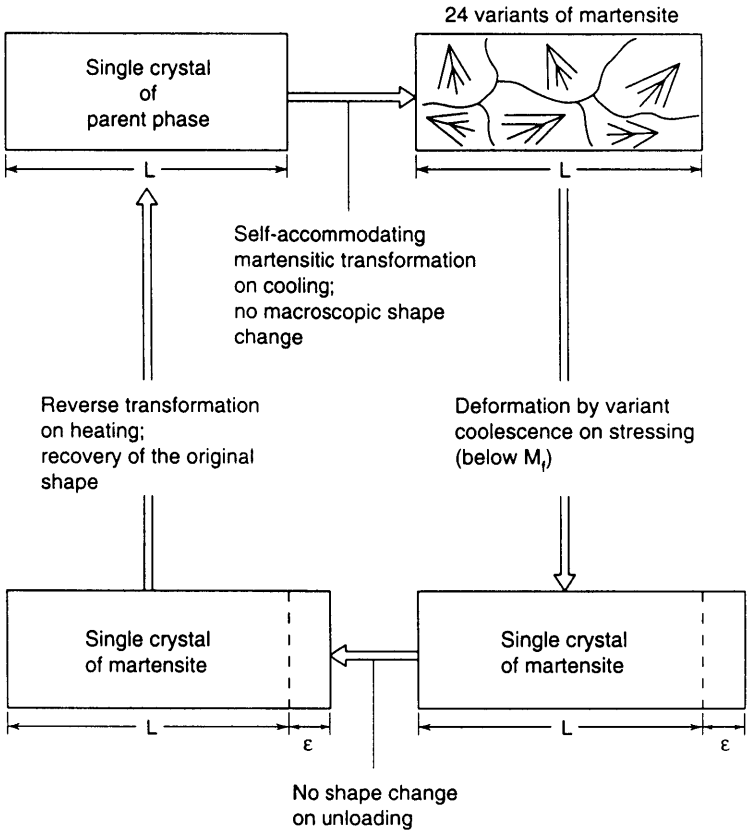

Fig. 7.1 A schematic of the shape-memory process from [98].

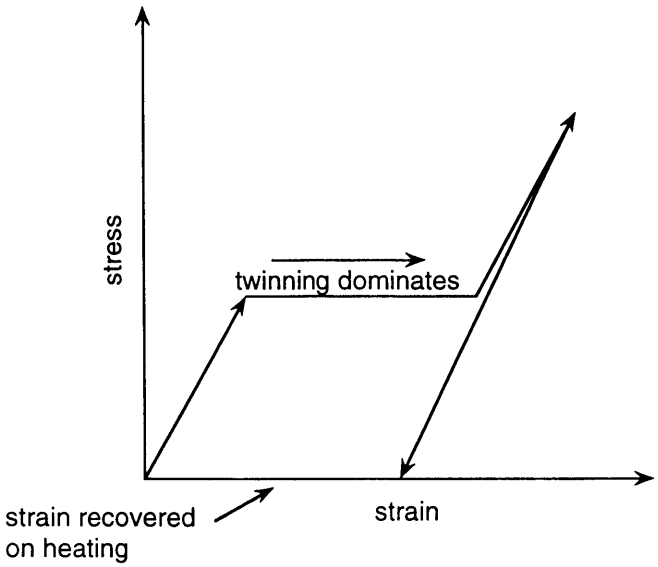

Fig. 7.2 Mechanical response of a typical shape-memory alloy.

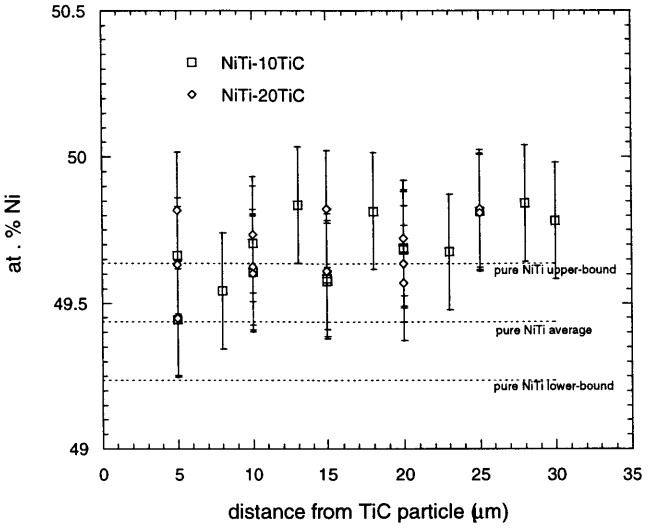

Fig. 7.3 Microprobe analysis of shape-memory NiTi-0TiC, NiTi-10TiC and NiTi-20TiC.

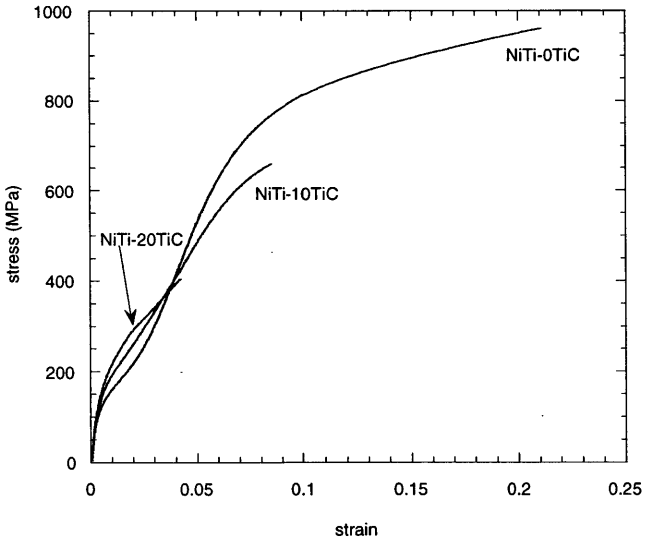

Fig. 7.4 Stress-strain response in tension of shape-memory NiTi-0TiC, NiTi-10TiC and NiTi-20TiC at 15 °C below the martensite finish temperature [96].

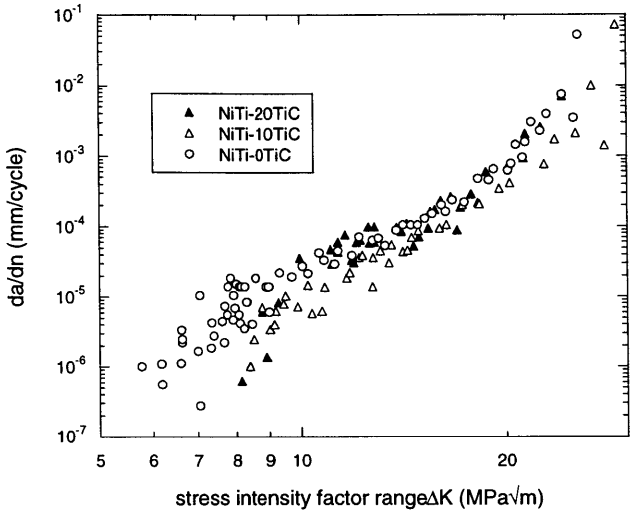

Fig. 7.5 da/dn vs. ΔK curves for shape-memory NiTi-0TiC, NiTi-10TiC and NiTi-20TiC tested at room temperature.

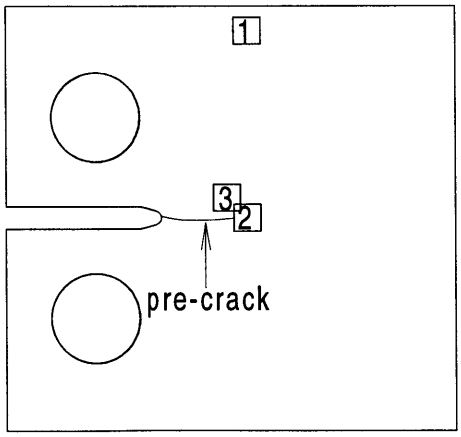

Fig. 7.6 Schematic of compact-test specimen showing the pre-crack and beam "spots" (squares) where neutron diffraction were acquired: Spot 1. No load Spot 2. Two measurements with a ΔK of 25 MPa√m and 32 MPa√m, respectively and Spot 3. An off-axis measurement at 32 MPa√m. The neutron beam spot size was 3 mm by 3 mm.

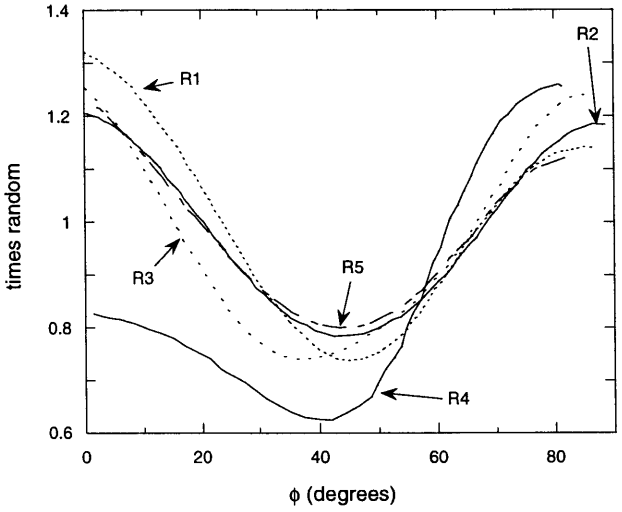

Fig. 7.7 (100) axial distribution plot for shape-memory NiTi-0TiC under various loads and from different locations. The designation are summarized in Table 7.4.

Chapter 8

Use of Shape-Memory and Superelastic Alloys

From August 1997 to February 1998 the author was a participant in the MIT-Germany program and worked in the area of shape-memory and superelastic alloys for Daimler-Benz AG, Germany. These alloys may have applications in their automotive (Mercedes-Benz) and aerospace (Airbus and Daimler-Benz Aerospace) divisions. The stay at Daimler-Benz also included extensive interaction with personnel from Ruhr Universität Bochum and Technische Universität München in Germany. For proprietary reasons no mention of actual applications or projects are made but the chapter is limited to describing some of the broader issues related to commercial applications of these alloys.

8.1 Commercial Alloys

The shape-memory effect was first found in a Au-Cd alloy and then in a In-Tl alloy. To date there have been numerous alloy systems that have been investigated for their shape-memory properties. Examples include systems based on Ag-Cd, Ni-Al, In-Tl, Ni-Ti, Cu-Zn, Cu-Al-Ni, Cu-Sn, Cu-Au-Zn, In-Cd, Mn-Cu and even more recently Fe based alloys. A large part of the research has focused on various elemental additions to the above systems. Of the many scientifically relevant shape-memory alloys, only Ni-Ti and Cu-based alloys have so far proven to be commercially viable in terms of cost, fabrication and engineering properties.

The two commercial Cu-based alloy systems are primarily Cu-Zn-Al and Cu-Al-Ni. These alloys tend to be more brittle than Ni-Ti alloys and their grain size has to be carefully controlled during fabrication. Cu-based alloys are also less corrosion resistant when compared to Ni-Ti based alloys. However, they are advantageous in that the transformation temperatures are higher than those of currently available Ni-Ti alloys. In addition, Cu-based alloys are also less expensive than Ni-Ti based alloys. Since the parent beta phase and the martensite phase is metastable in Cu-based shape memory alloys, the stability of their shape memory properties is influenced strongly by aging. This means that that transformation temperatures are affected by heat treatment and subsequently to thermal exposure during service.

8.2 Case study: Choice of alloy for use as an actuator

The broad requirements for a particular actuator application are summarized below:

(a) ability of the alloy to recover large strains under large stresses

b) small hysteresis effect

(c) moderate energy requirements for the phase transformation and consequently actuation

(d) fast response time on thermal cycling and consequently actuation

(e) stable behavior with respect to thermomechanical cycling

(f) stable behavior with respect to metallurgical aging phenomena

(g) corrosion resistance to humid environments

(h) commercial availability of the alloy in the form of wires to be easily incorporated into existing design

With the above the requirements in mind and given the limitations of Cu-based systems, Ni-Ti based alloy systems were the obvious choice. Up to 30% Cu can be added to the NiTi system while still retaining the high temperature austenitic phase. In contrast to other additions, substitution of even large concentrations of Cu does not affect the M_s temperature significantly. The presence of Cu also makes the M_s temperature less sensitive to variations in the Ni-Ti ratio. In the binary Ni-Ti alloy, M_s drops sharply as the Ni concentration increases from 50 to 51 at. %. This sensitivity is suppressed by the addition of Cu and hence allows for easier fabrication routes. The M_s temperature is also less sensitive to transformation cycling for the ternary Ni-Ti-Cu alloy than for the binary Ni-Ti alloy. In addition, Cu substantially narrows the hysteresis widths during thermal cycling. It has been observed that the hysteresis is reduced from 30° C for a binary NiTi alloy to less than 15° C for an alloy with 5% Cu. The narrower transformation hysteresis is also observed during the formation of stress induced martensite during mechanical cycling. This narrower hysteresis of Ni-Ti-Cu alloys has practical importance. Applications requiring a fast response time on thermal cycling are easier to realize with a narrow hysteresis alloy.

Another property influenced by copper additions to a binary Ni-Ti system is the lower yield strength of the martensite. This is the stress level at which the twins can re-orient. The larger strength differential between the austenite and the martensite phases results in more useful work that can be done by the shape-memory alloy during recovery.

Given the above properties of a ternary Ni-Ti-Cu alloy and the requirements, a Ni 45 at.% Ti 50 at.% Cu 5 at.% alloy was chosen.

8.3 Some existing challenges

(1) **Alloy development and modification to increase transformation temperatures**: There is still extensive work that needs to be done in modifying alloy compositions (with and without elemental additions), so as to favorably control transformation temperatures. For many applications, the temperature the alloys are exposed to during their desired operation is close to their transformation temperatures. In some cases thermal protection is possible, but in many others, due to design safety issues, the only solution is to increase the austenite start temperature. The new alloys so developed need to be completely characterized for their stress and temperature cycling fatigue properties.

(2) **Alloy composition control during manufacture**: A problem that has plagued the shape-memory and superelastic alloy manufacturing industry has been the need to control composition very accurately during manufacture. For example a 1 at. % change in the amount of nickel changes the transformation temperatures in NiTi by around 100°C [9]. This reproducibility issue is very important in critical applications.

(3) **Formability of the alloy in the desired shape**

(4) **Speed of transformation**: Ideally, martensite interface motion is limited by the speed of sound in the alloy. More practically, it is limited by the rate at which heat can be transferred to the alloy. Such issues are currently being addressed by heating shape-memory actuators intrinsically (i.e., using their own resistance or extrinsically by surrounding them with heating elements) in cases where the speed of transformation is critical.

(5) **Shape setting in linear superelastic materials**: Linear superelasticity is the phenomenon wherein NiTi alloys in the cold-worked state exhibit nearly hysteresis-free linear superelasticity, with elastically recoverable strains as high as 4%. The potential use in springs is of interest since the energy stored is almost four times that of steel. This effect is understood to arise from

twinned and untwinned highly-dislocated martensite. Thus using a hot forming process is not possible and work needs to be carried out to set these alloys in the desired shape and obtain high elastic strains [10].

(6) **Stability of the shape-memory and superelastic effect**: The stability of these effects with stress and temperature-cycling are very sensitive to composition and aging conditions. These issues are being addressed on a per-application basis and a complete body of work addressing this issue is still not available. Chapter 6 has shed light on the fundamental mechanisms that are associated with stress-cycling.

(7) **Behavior under different states of stress**: Experiments to evaluate the behavior of these alloys under different states of stress (ex. torsion, biaxial etc.) are only recently beginning to be systematically undertaken. As seen in Chapter 5, the directional dependence of the transformation strain suggests a dependence on the state of stress these materials are subjected to.

Chapter 9 Conclusions and Suggested Future Work

9.1 Conclusions

Due to the stand-alone nature of each chapter in this thesis, an appropriate conclusion is included at the end of each chapter. Here a table outlining the unique contributions of this work are presented.

Previously existing work	This work
In situ neutron diffraction measurements on materials subjected to elastic and plastic loading.	*In situ* neutron diffraction measurements during stress-induced reversible austenite to martensite phase transformations in NiTi subjected to loading. Associated modeling of neutron spectra to quantify strain, texture and volume fraction for austenite, martensite and TiC phases. (Chapter 2 and 3)
Anisotropic correction in Rietveld refinement of neutron spectra that reflects strain redistribution due to plastic deformation.	Anisotropic correction in Rietveld refinement of neutron spectra that reflects strain redistribution due to phase transformation. (Chapter 3)
Acoustic measurements of single crystal elastic constants of NiTi.	Excellent agreement between polycrystalline extensions of single crystal data (Hashin-Shtrikman and Hill averages) and neutron diffraction measurements. (Chapter 4)
No existing work on texture evolution in stress-induced martensite.	Texture evolution quantified from neutron diffraction spectra. (Chapter 5)
No reported fabrication of composites where the matrix deforms by stress-induced transformation.	Successful fabrication of such composites by HIP. (Chapter 4)
Neutron diffraction study of composites where the matrix deforms by slip or twinning.	Neutron diffraction study of composites where matrix deformation occurs due to stress-

	induced transformation. (Chapter 4)
Self-accommodation of martensite during twinning.	Self-accommodation of martensite during stress-induced transformation. Excellent agreement between Eshelby theory predictions and measurements suggesting that the transformation mismatch strain is accommodated. (Chapter 4)
Macroscopic observations during stress-cycling in superelastic NiTi.	Microscopic observations of phase texture, strain and volume fraction evolution during stress-cycling in superelastic NiTi. Significant changes in texture. (Chapter 6)
Experimental work on fracture-fatigue in shape-memory alloys.	Initiation of fracture-fatigue studies in shape-memory alloys and composites with emphasis on mechanisms. (Chapter 7)

9.2 Suggested future work

The following research projects are proposed:

(1) **Linear superelasticity in NiTi and NiTi-TiC composites**: The hysteresis in cold-worked NiTi is considerably reduced and the stress-strain behavior is almost linear up to 4%. TiC particles may be effective in modifying the moduli in these materials.

(2) **Indentation experiments**: Considerable time, cost and effort are used to prepare samples for mechanical testing to determine superelastic and shape-memory behavior. In addition, the maximum recoverable strain and maximum recovery stresses are difficult to obtain in a non-destructive manner. Indention experiments may be a fast and effective way to provide some or all of these results. The alloy can even be heated to undergo a transformation while indentation data is obtained. The samples may have to be prepared electrochemically so that the surface is not twinned or locally transformed.

(3) **Strain anisotropy in non-cubic systems**: The Rietveld formulation that was used here worked very well with cubic austenitic NiTi. The monoclinic martensite could not be treated in the same way since the volume fraction of martensite was too low for the refinements to converge in this work. Almost no work exists on using similar formulations on systems with other symmetries. Such measurement on martensite may provide valuable information on deformation twinning. As discussed in Chapter 3, the behavior of the lattice parameter of martensite is not examined. Fig. 9.1 shows the lattice parameters exhibiting no significant changes with stress. More work needs to be done to ascertain the strain in monoclinic structures such as martensite from lattice parameters or even evaluate limitations in the Rietveld procedure for low symmetry systems.

(4) **Total recoverable strain prediction**: A more rigorous model can be developed that takes into account the texture evolution and uses it along with extensometer data to decouple the elastic strains and non-elastic transformation or twinning strains. While Eq. 5.6 has been proposed, an FEM implementation using the information from axial distribution plots to predict total transformation strains in polycrystalline shape-memory and superelastic alloys may be worthy of investigation.

(5) **Fatigue/fracture investigation**: As described earlier in Chapter 7, the fatigue and fracture mechanisms have been little studied for composites in cases where the matrix undergoes deformation twinning or stress-induced transformation.

9.3 Figures

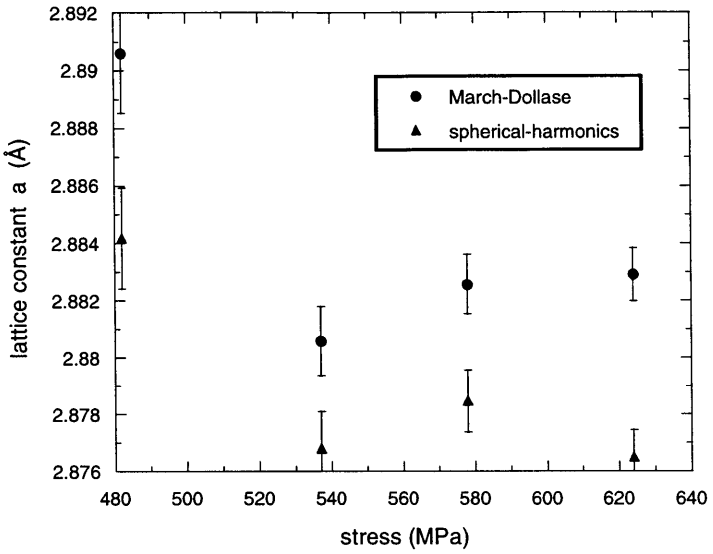

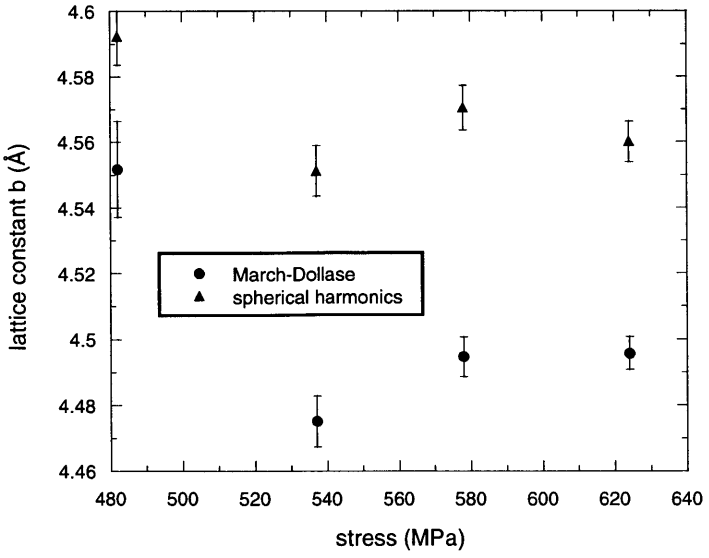

(see caption on next page)

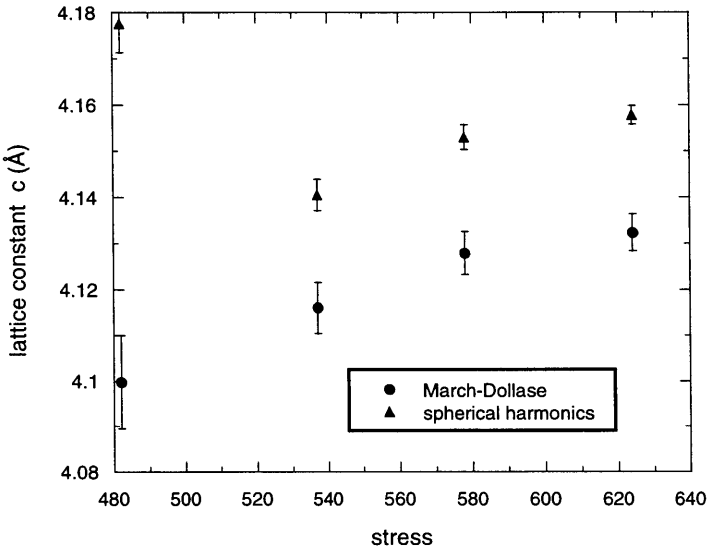

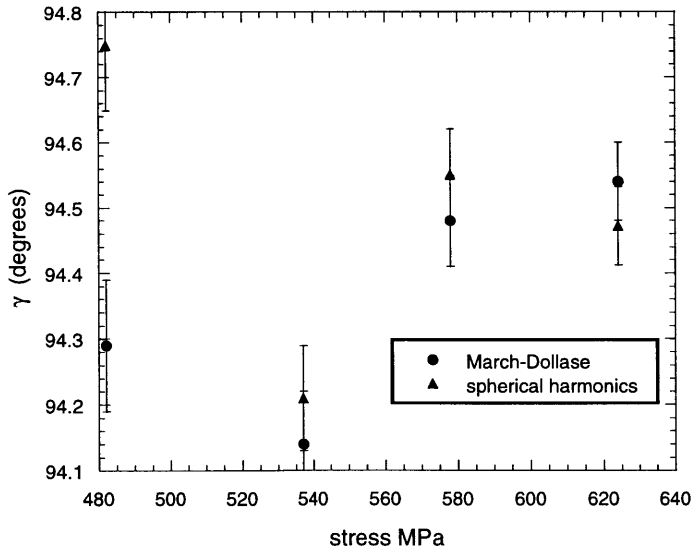

Fig. 9.1 Lattice parameters of martensite as a function of stress from Rietveld measurements using both March-Dollase and spherical harmonics texture formulations.

REFERENCES

[1] M. A. M. Bourke, R. Vaidyanathan, and D. C. Dunand, *Appl. Phys. Lett.*, vol. 69, pp. 2477, 1996.

[2] R. Vaidyanathan, M. A. M. Bourke, and D. C. Dunand, in *Los Alamos Neutron Science Center Activity Report*, Los Alamos National Laboratory, 1998 (in print).

[3] R. Vaidyanathan, M. A. M. Bourke, and D. C. Dunand, "Analysis of Neutron Diffraction Spectra Obtained During Stress-induced Transformations in Superelastic NiTi," *to be submitted to J. Appl. Phys.*, 1999.

[4] R. Vaidyanathan, M. A. M. Bourke, and D. C. Dunand, "Stress-Induced Martensitic Transformations in NiTi and NiTi-TiC Composites Investigated by Neutron Diffraction," *accepted for publication in Mat. Sci. and Engr. A (proc. ICOMAT 98)*, 1998.

[5] R. Vaidyanathan, M. A. M. Bourke, and D. C. Dunand, "Phase Fraction, Texture and Strain Evolution in Superelastic NiTi and NiTi-TiC Composites Investigated by Neutron Diffraction," *to be submitted to Acta Mater.*, 1999.

[6] R. Vaidyanathan, M. A. M. Bourke, and D. C. Dunand, "Neutron Diffraction Investigation of the Mechanical and Crystallographic Properties of Superelastic NiTi and NiTi-TiC Composites," *submitted for presentation at the 1999 TMS Annual Meeting, San Diego (proc. to be published)*, 1998.

[7] R. Vaidyanathan, M. A. M. Bourke, and D. C. Dunand, "Stress-cycling in Superelastic NiTi Studied with Neutron Diffraction," *to be submitted to Metall. Mater. Trans.*, 1999.

[8] R. Vaidyanathan, U. Ramamurty, D. C. Dunand, and S. Suresh, "Fatigue Behavior of Shape-Memory NiTi and NiTi-10TiC," *to be submitted to Scripta Mater.*, 1999.

[9] H. Funakubo, *Shape Memory Alloys*, New York: Gordon and Breach, 1987.

[10] T. W. Duerig, K. N. Melton, D. Stoeckel, and C. M. Wayman, *Engineering Aspects of Shape Memory Alloys*, London: Butterworth-Heinemann, 1990.

[11] C. M. Wayman, *MRS Bull.*, vol. 18, pp. 49, 1993.

[12] C. M. Jackson, H. J. Wagner, and R. J. Wasilewski, *NASA-SP 5110*, NASA, 1972.

[13] J. E. Hanlon, S. R. Butler, and R. J. Wasilewski, *Trans. Metall. Soc. AIME*, vol. 239, pp. 1323, 1967.

[14] R. J. Wasilewski, S. R. Butler, and J. E. Hanlon, *Metal Sci. J. 1*, pp. 104, 1967.

[15] F. E. Wang, B. F. DeSavage, W. J. Buehler, and W. R. Hosler, *J. Appl. Phys.*, vol. 39, pp. 2166, 1968.

[16] A. D. Johnson and P. I. Katz, *J. Appl. Phys.*, vol. 48, pp. 73, 1977.

[17] F. E. Wang and W. J. Buehler, *Appl. Phys. Lett.*, vol. 21, pp. 105, 1972.

[18] R. R. Hasiguti and K. Iwasaki, *J. Appl. Phys.*, vol. 39, pp. 2182, 1968.

[19] R. J. Wasilewski, *Trans. Metall. Soc. AIME*, vol. 233, pp. 1691, 1965.

[20] J. F. Goff, *J. Appl. Phys.*, vol. 397, pp. 2208, 1968.

[21] J. F. Goff, *J. Appl. Phys.*, vol. 35, pp. 2929, 1964.

[22] F. E. Wang, B. F. DeSavage, F. Bernard, W. J. Buehler, and W. R. Hosler, *J. Appl. Phys.*, vol. 39, pp. 2166, 1968.

[23] R. S. Allgaier, *J. Phys. Chem. Solids*, vol. 28, pp. 1293, 1967.

[24] K. Mukherjee, F. Milillo, and M. Chandrasekaran, *Mat. Sci. Engr.*, vol. 14, pp. 143, 1974.

[25] S. Miyazaki, S. Kimura, F. Takei, K. Otsuka, and Y. Suzuki, *Scripta Metall.*, vol. 17, pp. 1057, 1983.
[26] F. Takei, T. Miura, S. Miyazaki, S. Kimura, K. Otsuka, and Y. Suzuki, *Scripta Metall.*, vol. 17, pp. 987, 1983.
[27] T. Saburi, M. Yoshida, and S. Nenno, *Scripta Metall.*, vol. 18, pp. 363, 1984.
[28] H. Ling and R. Kaplow, *Metall. Trans. A*, vol. 12A, pp. 2101, 1981.
[29] G. E. Bacon, *Neutron Diffraction*, Oxford: Oxford University Press, 1962.
[30] D. C. Dunand, D. Mari, M. A. M. Bourke, and J. A. Goldstone, *J. Physique*, vol. IV, pp. 2820, 1996.
[31] D. C. Dunand, D. Mari, M. A. M. Bourke, and J. A. Roberts, *Metall. Mater. Trans.*, vol. 27A, pp. 2820, 1996.
[32] W. Buhrer, R. Gotthardt, and M. S. Wechsler, proc. International Conference on Martensitic Transformations ICOMAT-86, 1986.
[33] K. Otsuka, M. Tokonami, K. Shimizu, Y. Iwata, and I. Shibuya, *Acta Metall.*, vol. 27, pp. 965, 1979.
[34] M. A. M. Bourke, J. A. Goldstone, N. Shi, J. E. Allison, M. G. Stout, and A. C. Lawson, *Scripta Metall.*, vol. 29, pp. 771, 1993.
[35] M. A. M. Bourke, J. A. Goldstone, and T. M. Holden, in *Measurement of Residual and Applied Stress using Neutron Diffraction*, NATO ASI Series E No 216, M. T. Hutchings and A. D. Krawitz, Eds. Netherlands: Kluwer Academic, pp. 369, 1992.
[36] N. Shi, M. A. M. Bourke, J. A. Roberts, and J. E. Allison, *Metall. Mater. Trans.*, vol. 28A, pp. 2741, 1997.
[37] A. March, *Z. Kristallogr.*, vol. 81, pp. 285, 1932.
[38] W. A. Dollase, *J. Appl. Cryst.*, vol. 19, pp. 267, 1986.
[39] A. C. Larson and R. B. V. Dreele, *General Structure Analysis System (GSAS)*, Los Alamos National Laboratory Report LAUR 8-748, 1986.
[40] R. J. Wasilewski, *Scripta Metall.*, vol. 5, pp. 127, 1971.
[41] T. Saburi, T. Tatsumi, and S. Nenno, *J. Phys.*, vol. 43, pp. C4, 1982.
[42] S. Miyazaki and K. Otsuka, *Metall. Trans. A*, vol. 17, pp. 53, 1986.
[43] M. T. Hutchings and A. D. Krawitz, *Measurement of Residual and Applied Stress Using Neutron Diffraction*, NATO ASI Series E No 216, Netherlands: Kluwer Academic, 1992.
[44] H. M. Rietveld, *J. Appl. Crystallogr.*, vol. 2, pp. 65, 1969.
[45] H. J. Bunge, *Texture Analysis in Materials Science*, London: Butterworth, 1982.
[46] M. A. M. Bourke, private communication, 1996.
[47] M. R. Daymond, M. A. M. Bourke, and R. B. V. Dreele, *J. Appl. Phys.*, vol. 82, pp. 1554, 1997.
[48] J. F. Nye, *Physical Properties of Crystals*, Oxford: Oxford University Press, 1985.
[49] R. B. V. Dreele, *J. Appl. Cryst.*, vol. 30, pp. 517, 1997.
[50] P. H. Leo, T. W. Shield, and O. P. Bruno, *Acta Metall.*, vol. 41, pp. 2477, 1993.
[51] S. Miyazaki, K. Otsuka, and Y. Suzuki, *Scripta Metall.*, vol. 15, pp. 287, 1981.
[52] P. G. McCormick and Y. Liu, *Mat. Sci. Engr.*, vol. A167, pp. 51, 1993.
[53] T. M. Brill, S. Mittelbach, W. Assmus, M. Muellner, and B. Luethi, *J. Phys.: Condens. Matter*, vol. 3, pp. 9621, 1991.
[54] B. Clausen, T. Lorentzen, and T. Leffers, *Acta Mater.*, vol. 46 9, pp. 3087, 1998.
[55] D. Mari and D. C. Dunand, *Metall. Mater. Trans.*, vol. 26A, pp. 2833, 1995.

[56] D. Mari, L. Bataillard, D. C. Dunand, and R. Gotthardt, *J. Physique IV*, vol. 5, pp. C8-659, 1995.
[57] K. L. Fukami-Ushiro and D. C. Dunand, *Metall. Mater. Trans.*, vol. 27A, pp. 183, 1996.
[58] K. L. Fukami-Ushiro, D. Mari, and D. C. Dunand, *Metall. Mater. Trans.*, vol. 27A, pp. 193, 1996.
[59] D. C. Dunand, K. L. Fukami-Ushiro, D. Mari, J. A. Roberts, and M. A. M. Bourke, *Materials for Smart Systems II*, E. P. George, R. Gotthardt, K. Otsuka, S. Trolier-McKinstry, M. Wun-Fogle Eds., 1996.
[60] E. F. Sturcken and J. W. Croach, *Trans. Met. Soc. AIME*, vol. 227, pp. 934, 1963.
[61] T. M. Poletika, S. N. Kulkov, and V. E. Panin, *Poroshkova Metallurgiya*, vol. 7 (247), pp. 54, 1983.
[62] S. N. Kulkov, T. M. Poletika, A. Y. Chukhlomin, and V. E. Panin, *Poroshkovaya Metallurgiya*, vol. 8 (260), pp. 88, 1984.
[63] O. Mercier, K. N. Melton, G. Gremaud, and J. Haegi, *J. Appl. Phys.*, vol. 51 (3), pp. 1833, 1980.
[64] Z. Hashin and S. Shtrikman, *J. Mech. Phys. Solids*, vol. 10, pp. 335, 1962.
[65] W. Voigt, *Lehrbuch der Krystallphysik*, Berlin: Teubner, 1910.
[66] A. Reuss, *Z. angew. Math. Mech.*, vol. 9, pp. 49, 1929.
[67] R. Hill, *Proc. Phys. Soc. (London)*, vol. A65, pp. 349, 1952.
[68] T. W. Clyne and P. J. Withers, *An Introduction to Metal Matrix Composites*, Cambridge: Cambridge University Press, 1993.
[69] R. Chang and L. J. Graham, *J. Appl. Phys.*, vol. 37, pp. 3778, 1966.
[70] J. Shackelford and W. Alexander, *The CRC Materials Science and Engineering Book*, Boca Raton: CRC Press, 1992.
[71] D. C. Dunand and A. Mortensen, *Mater. Sci. Engr.*, vol. 135A, pp. 179, 1991.
[72] D. C. Dunand and A. Mortensen, *Acta. Metall.*, vol. 39, pp. 127, 1991.
[73] T. Saburi and S. Nenno, in *Solid-Solid Phase Transformations*, H. I. Aaronson, D. E. Loughin, R. F. Sekerka, and C. M. Wayman Eds., Warrendale: Met. Soc. AIME, 1981.
[74] G. B. Olson and M. Cohen, *Scripta Metall.*, vol. 9, pp. 1247, 1975.
[75] R. J. Salzbrenner and M. Cohen, *Acta Metall.*, vol. 27, pp. 739, 1979.
[76] K. Otsuka, T. Sawamura, and K. Shimizu, *Physica Status Solidi*, vol. 5, pp. 457, 1971.
[77] S. P. Gupta and A. A. Johnson, *Trans JIM*, vol. 14, pp. 292, 1973.
[78] K. Madangopal, J. Singh, and S. Banerjee, *Scripta Metall.*, vol. 25, pp. 2153, 1991.
[79] J. D. Vos, L. Delaey, E. Aernoudt, and P. V. Houtte, *Z. Metallkde*, vol. 69, pp. 511, 1978.
[80] T. Onda, Y. Bando, T. Ohba, and K. Otsuka, *Mater. Trans. JIM*, vol. 33, pp. 354, 1992.
[81] O. Matsumoto, S. Miyazaki, K. Otsuka, and H. Tamura, *Acta Metall.*, vol. 35, pp. 2137, 1987.
[82] Y. Kudoh, M. Tokohami, S. Miyazaki, and K. Otsuka, *Acta Metall.*, vol. 33, pp. 2049, 1985.
[83] W. Buhrer, R. Gotthardt, A. Kulik, and O. Mercier, *J. Phys.*, vol. 43, pp. 219, 1982.
[84] R. Plietsch and K. Ehrlich, *Acta Mater.*, vol. 45, pp. 2417, 1997.
[85] S. Miyazaki, "Thermal and Stress Cycling Effects and fatigue Properties of NiTi Alloys," in *Engineering Aspects of Shape Memory Alloys*, T. W. Duerig, K. N. Melton, D. Stoeckel, and C. M. Wayman Eds., pp. 394, 1990.
[86] H. Tobushi, H. Iwanaga, K. Tanaka, T. Hori, and T. Sawada, *JSME International Journal*, vol. I 35 3, pp. 271, 1992.

[87] N. Hagemeister, L. H. Yahia, C. Armand, and T. Lours, proc. First International Conference on Shape Memory and Superelastic Technologies, 1994.
[88] M. Kawaguchi, Y. Ohashi, and H. Tobushi, *JSME International Journal*, vol. 1 34 1, pp. 76, 1991.
[89] K. N. Melton and O. Mercier, *Acta Metall.*, vol. 27, pp. 137, 1979.
[90] K. N. Melton and O. Mercier, *Acta Metall.*, vol. 29, pp. 293, 1981.
[91] S. Miyazaki, Y. Sugaya, and K. Otsuka, proc. MRS Int'l Mtg. on Adv. Mats., vol. 9, pp. 251, 1989.
[92] Y. Furuya, H. Shimada, M. Matsumoto, and T. Honma, proc. MRS Int'l. Mtg. on Adv. Mats., vol. 9, pp. 269, 1989.
[93] S. Miyazaki, M. Suizu, K. Otsuka, and T. Takshima, proc. MRS Int'l Mtg. on Adv. Mats., vol. 9, pp. 263, 1989.
[94] R. H. Dauskardt, T. W. Duerig, and R. O. Ritchie, proc. MRS Int'l Mtg. on. Adv. Mats., vol. 9, pp. 243, 1989.
[95] R. L. Holtz, K. Sadananda, and M. A. Imam, proc. Johannes Weertman Symposium, TMS, 1996.
[96] K. Johansen, "TiC Verstärkung pulvermetallurgisch hergestellter NiTi-Formgedächtnislegierungen, PhD Thesis," Bochum: Ruhr-Universität, 1998.
[97] S. Suresh, *Fatigue of Materials*, Cambridge:Cambridge University Press, 1991.
[98] C. M. Wayman, in *Solid-Solid Transformations*, H. I. Aaronson, D. E. Loughin, R. F. Sekerka, and C. M. Wayman Eds., Warrendale: Met. Soc. AIME, 1981.